Effect of microstructure in electrospark deposition repaired conventional and additive manufactured Ni-superalloys

By

Pablo Daniel Enrique

A thesis

presented to the University of Waterloo

in fulfillment of the

thesis requirement for the degree of

Doctor of Philosophy

in

Mechanical and Mechatronics Engineering

Waterloo, Ontario, Canada, 2021

Examining Committee Membership

The following served on the Examining Committee for this thesis. The decision of the Examining Committee is by majority vote.

External Examiner	Professor Wei Zhang, Materials Science and Engineering, Ohio State University, United States
Supervisors	Professor Norman Y. Zhou, Mechanical & Mechatronics Engineering, University of Waterloo, Canada
	Professor Ehsan Toyserkani Mechanical & Mechatronics Engineering, University of Waterloo, Canada
Internal Members	Professor Mihaela Vlasea Mechanical & Mechatronics Engineering, University of Waterloo, Canada
	Professor Elliot Biro Mechanical & Mechatronics Engineering, University of Waterloo, Canada
Internal-external Member	Professor Michael Pope Chemical Engineering, University of Waterloo, Canada

Author's Declaration

This thesis consists of material all of which I authored or co-authored: see Statement of Contributions included in the thesis.

I understand that my thesis may be made electronically available to the public.

Statement of Contributions

This thesis is composed of a literature review in Chapter 2 and several studies in manuscript format (Chapter 3-6). The literature review is partially composed of an in-progress book chapter. Each of the studies in Chapters 3-6 are based on published papers. I am the primary author of all content included in this manuscript, and the contributions of the authors are listed below. Prof. Norman Zhou and Prof. Ehsan Toyserkani are the anchor authors, having provided resources and supervision for the research, as well as having edited and reviewed the respective papers on which they are listed.

Chapter 2

This chapter includes content from a book chapter currently in progress, authored by Ehsan Toyserkani, Ali Keshavarzkermani, Reza Esmaeilizadeh, and Pablo D. Enrique. I have included in this thesis portions of the book chapter which were written by me, but were edited by the other authors.

Chapter 3

P.D. Enrique, Z. Jiao, N.Y. Zhou, E. Toyserkani, Dendritic coarsening model for rapid solidification of Ni-superalloy via electrospark deposition, J. Mater. Process. Technol. 258 (2018) 138–143.

I was responsible for experiment design, sample preparation, sample characterization, analysis, and writing of the manuscript. Zhen Jiao edited the manuscript and contributed to the experiment design.

Chapter 4

P.D. Enrique, Z. Jiao, N.Y. Zhou, E. Toyserkani, Effect of microstructure on tensile properties of electrospark deposition repaired Ni-superalloy, Mater. Sci. Eng. A. 729 (2018) 268–275.

I was responsible for experiment design, sample preparation, sample characterization, analysis, and writing of the manuscript. Zhen Jiao edited the manuscript and assisted with interpretation of the results.

Chapter 5

P.D. Enrique, A. Keshavarzkermani, N.Y. Zhou, Effect of Micro-segregation on High Temperature Microstructure Evolution in Rapid Solidification Processed Nb-rich Ni-superalloys, Adv. Eng. Mater. (2021).

I was responsible for experiment design, sample preparation, sample characterization, analysis, and writing of the manuscript. Ali Keshavarzkermani edited the manuscript, assisted with interpretation of the results, and contributed to sample characterization.

Chapter 6

P.D. Enrique, A. Keshavarzkermani, R. Esmaeilizadeh, S. Peterkin, H. Jahed, E. Toyserkani, N.Y. Zhou, Enhancing fatigue life of additive manufactured parts with electrospark deposition post-processing, Addit. Manuf. 36 (2020) 101526.

I was responsible for experiment design, sample preparation, sample characterization, analysis, and writing of the manuscript. Ali Keshavarzkermani and Reza Esmaeilizadeh both edited the manuscript and assisted with sample characterization. Stephen Peterkin edited the manuscript and provided technical expertise on the electrospark deposition process. Prof. Hamid Jahed edited the manuscript, assisted with interpretation of the results, and provided resources for sample characterization.

Abstract

The ability to extend component lifespans and improve performance through repair and coating techniques is an important area of research with widespread industrial applications. Numerous industries, including aerospace, can benefit significantly from advancements in the repair and coating of high-performance, heat-sensitive parts; with engine temperatures steadily increasing and the shift towards reusable space exploration vehicles in cargo and crewed flights, the durability of key components is a concern. This is especially true with the increasing use of additive manufacturing, which can create parts with considerable geometrical freedom but suffer from high surface roughness and near-surface porosities.

Electrospark deposition (ESD) is a promising choice for the repair and coating of sensitive components due to its low heat input. When alloys are processed using ESD, a very fine subgrain microstructure forms with the potential for micro-segregation at subgrain boundaries. The aim of this research is to identify the influence of the subgrain microstructure and subgrain boundaries on the mechanical properties and phase transformations in Inconel 718, a commonly used Nb-rich Ni-superalloy. Inconel 718 is deposited on conventional Inconel 718 substrates in a series of studies that evaluate the ability to repair cavities and apply coatings. The included studies relate the thickness of solidified droplets (splats) to the size of the subgrain microstructure, microhardness, and yield strength of the material, while demonstrating that the subgrain and splat boundaries act as crack propagation pathways during tensile failure. Micro-segregation of Nb along the subgrain boundaries is also shown to increase the number of Nb-rich phases forming during high temperature heat treatments. These studies improve our understanding of the mechanical response of ESD-processed Nb-rich Ni-superalloys, and are used to tailor the application of ESD to improving the surface condition and fatigue life of a dissimilar additive manufactured Ni-superalloy. The findings show potential for the repair and surface enhancement of damaged or critical regions in heat-sensitive conventional and additive manufactured parts.

Acknowledgements

I am deeply grateful to those who supported me over the past four years and made my PhD journey enjoyable and memorable. I would like to thank my supervisors Prof. Norman Zhou and Prof. Ehsan Toyserkani for providing their guidance and mentorship. I appreciate the opportunities you provided to help me fulfill my broad research interests. I would like to thank my colleagues and friends at the Centre for Advanced Materials Joining (CAMJ) and the Multi-Scale Additive Manufacturing Lab (MSAM). I look back fondly at the friendships that were forged through shared struggles and shared celebrations. Thank you to Ali Keshavarzkermani, Chris DiGiovanni, Dr. Ehsan Marzbanrad, Nivas Ramachandiran, Reza Esmaeilizadeh, Dr. Robert Liang, Sagar Patel, Shehryar Khan, and Dr. Yahya Mahmoodkhani for all your help. I found every one of the technical and casual conversations we had to be insightful and enjoyable.

I would like to thank Nigel Scotchmer, Foss Jiao, and Stephen Peterkin from Huys Industries for supplying resources, providing feedback, and dedicating time towards the many projects we collaborated on. Your contributions towards my development as a researcher were invaluable.

Thank you to Huys Industries, the Natural Sciences and Engineering Research Council of Canada, and the Waterloo Institute for Nanotechnology for providing the financial support that made all of this possible.

I would also like to thank Dr. Yuquan Ding, Dr. Nina Heinig, and Dr. Lei Zhang for their assistance and training with various characterization techniques. My research benefited significantly from your expertise, and with your guidance my own abilities have significantly improved.

I would like to express gratitude towards my family, for encouraging curiosity and a strong work ethic at a young age, and without whom none of this would have been possible.

Finally, I would like to extend a heartfelt thank you to my better half, Amanda Forwell, for her unconditional love and support. The thought of spending time with you provided me with much needed motivation on days when nothing else went right.

Table of Contents

List of Figures

List of Tables

Chapter 1. Introduction

1.1 Problem statement

Metal deposition processes are frequently used in industry for the application of coatings and the repair of components. The benefits are numerous: high performance coatings can be used to extend product lifespans, the repair of defects formed during manufacturing reduce the need to scrap parts, and the repair or re-building of components damaged in service reduces end-of-life waste. Low heat input repair and coating techniques that can address heat-sensitive or high-performance components are especially useful. These allow for the coating and repairing of parts with thin geometries or parts used in extreme environments where performance can be negatively affected by high heat input.

Component repair or coating is often performed using traditional welding techniques such as gas tungsten arc welding (GTAW). A commonly cited issue with this technique is the large heat-affected zones that form due to high heat input, negatively affecting microstructure, microhardness, and residual stress fields that can accelerate fatigue failure [1,2]. In addition to these issues, repair processes can introduce defects that result in a smaller fatigue lifetime for the repaired component than the original component. Li et al. [3] found that cracks with a high aspect ratio introduced during the GTAW repair of a cast aluminum alloy were most responsible for an observed decrease in fatigue life, with spherical defects playing a smaller role. These issues have encouraged the development of other techniques more favourable to coating and repair applications.

A commonly used low heat input coating/repair technique is a directed energy deposition (DED) process which uses a laser or electron beam to melt and deposit a wire or powder feedstock material. Laser-based DED benefits from more flexible operation than electron beam DED – which requires the use of a vacuum – as well as lower heat input than GTAW. It also demonstrates good metallurgical bonding, unlike techniques such as cold spray or thermal spray which have very low heat input but are more susceptible to spalling failure [4]. Bennett et al. [5] evaluates the benefit of using DED repair for an automotive die compared to GTAW. The DED repaired die shows the same lifespan as that of the original die, whereas GTAW repaired dies last an average of 21% of the original lifespan. Significant environmental benefits are identified to the longer lifespan and

less frequent repair cycles, including the use of less feedstock material, lower ecotoxicity, lower exposure to carcinogenic material, and lower fossil fuel use (fewer repair cycles need fewer heat treatments). Therefore, there is a strong economic and sustainability argument for the use of cost-effective low heat input coating/repair techniques that can achieve high quality depositions with small heat-affected zones, low quantity of defects, and good metallurgical bonding.

The development of processes than can address the repair and coating of even more heat-sensitive parts is highly beneficial in many industries. Electrospark deposition (ESD) is a process in which a metal rod or wire feedstock is transferred using a short duration spark and rapidly solidified in a droplet-by-droplet fashion to obtain the desired deposition thickness. When compared to laser or electron beam DED processes, the small volume of material transferred with each spark in ESD allows for faster cooling rates and less heat buildup in the component being repaired or coated. An example thin wall component repair using ESD performed as part of this research is shown in Figure 1. This Rolls-Royce Tyne RTy.20 Mk 22 aircraft engine turbine blade, used in the Transall C-160 military transport aircraft first flown in 1963, continues to be used today. As equipment ages and replacement parts become less common, effective repair processes become more and more critical.

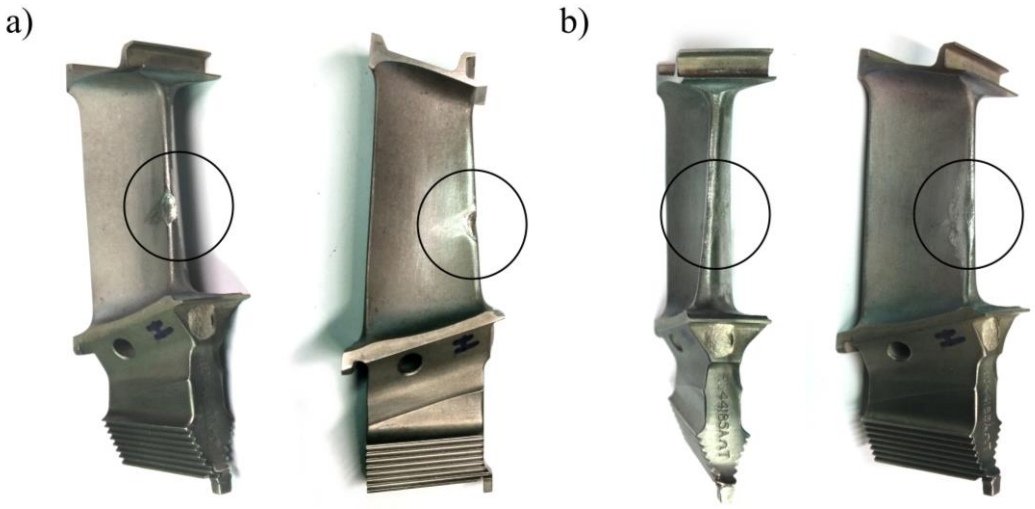

Figure 1. A Rolls-Royce Tyne RTy.20 Mk 22 aircraft engine turbine blade still in use today on the Transall C-160 military transport aircraft. As part of this research, the edge defect in (a) is repaired using an electrospark deposition process in (b).

In addition to addressing the coating and repair of high-value conventionally manufactured parts, low heat input metal deposition processes can also be used as a post-processing step to address

challenges with the adoption of fully additive manufactured parts. This is especially true for Ni-superalloy components, a class of high-value alloys that are fundamental to the aerospace, energy, and chemical industries. A number of early adopters in the aerospace industry have incorporated additive manufacturing of Ni-superalloys into their supply chain: SpaceX has implemented additive manufactured Inconel components in their SuperDraco engines [6], GE has successfully tested a commercial turboprop engine with more than a third of its components additively manufactured [7], and Patria has additively manufactured an Inconel 625 engine part for use by the Finnish air force in an F/A-18 Hornet fighter [8]. However, broad concerns regarding the reliability and long-term durability of these components remain. The servicing of these parts will necessitate the development of lower heat input repair processes to address thinner features that are more susceptible to heat buildup. Additionally, the higher surface roughness and higher frequency of near-surface porosities in additive manufactured parts are especially detrimental to part performance [9,10], which makes surface modification post-processing a necessity in high-performance parts.

Many surface modification techniques focus on reducing surface roughness and eliminating surface-related defects that influence the performance of parts, including the fatigue life and corrosion resistance. Although this is also true of parts made with other manufacturing processes, studies have shown that the as-built surface features in additive manufactured parts initiate cracking that can propagate due to cyclic thermal and mechanical stresses and lead to fatigue failure [11–13]. Removing these features using surface post-processing either shifts the crack initiation site to the less detrimental internal defects if they are present or, if sufficiently dense, achieves fatigue life results that compare to those of wrought parts [10,14]. Resistance to corrosion or oxidation is also influenced by the surface roughness, with the greater exposed surface area on as-built additive manufactured parts increasing their susceptibility to interfacial reactions [15]. However, applications that require cell adhesion or high-grip surfaces may benefit from an increased surface roughness. As a result, the post-processing procedure applied to additive manufactured parts must be chosen with the target application and required surface condition in mind. The use of a low heat input coating/repair technique to address surface roughness and surface defects in additive manufactured parts can also impart beneficial surface properties by depositing materials with high hardness, wear resistance, or corrosion resistance, obtaining higher part

performance and part lifespan if small heat-affected zones, low quantity of defects, and good metallurgical bonding are achieved.

1.2 Thesis objective

The use of electrospark deposition post-processing for coating and repair of high-performance parts requires further study of the process-related microstructure. This thesis has two objectives:

1. This thesis aims to understand the role of subgrain microstructure, boundaries, and micro-segregation on the mechanical properties and phase transformations in a common Nb-rich Ni-superalloy processed using ESD. This involves three studies on microstructure features formed due to very high cooling rates and the unique droplet-by-droplet mechanism with which ESD builds up material.
2. This thesis also aims to apply these findings to the repair of additive manufactured parts, with the goal of improving part performance beyond the original condition. The application is selected to benefit from properties identified in the ESD-processed Ni-superalloy.

The studies corresponding to each objective are presented in Figure 2, and discussed in greater detail in the following section.

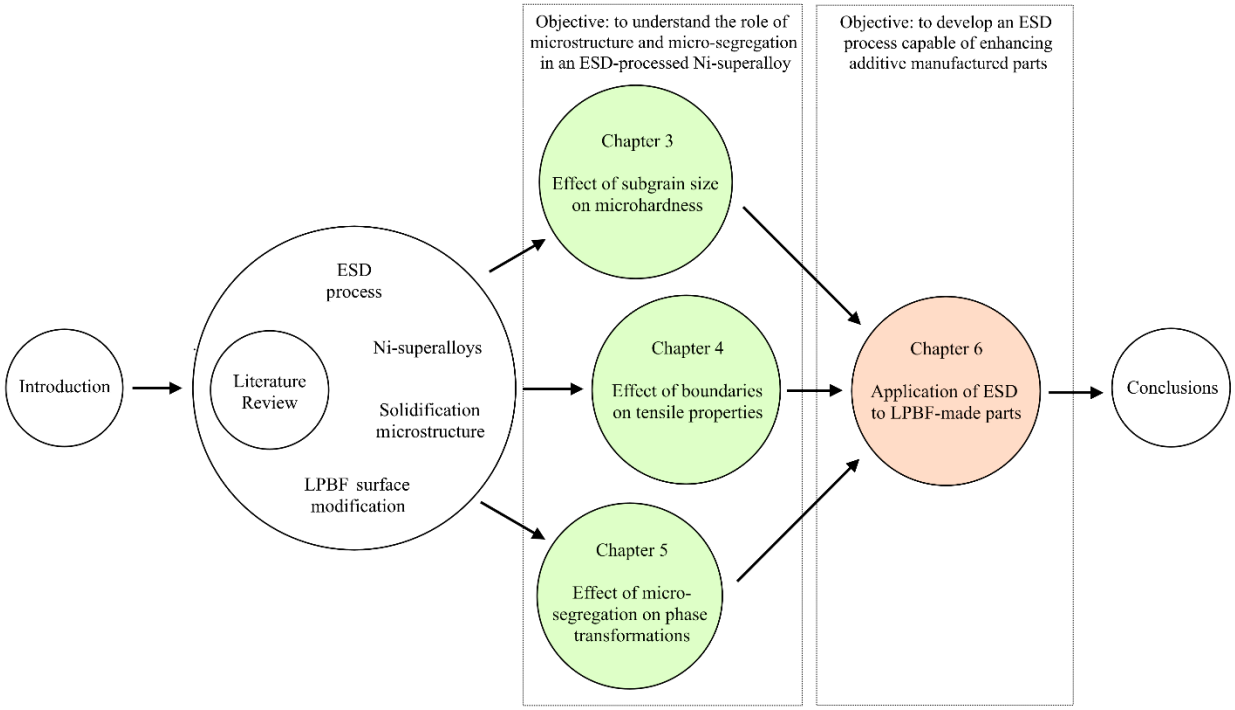

Figure 2. Graphical thesis abstract showing the connecting studies and their objectives

1.3 Thesis approach and overview

This thesis details work performed to develop a process for the electrospark deposition coating and repair of conventional and additive manufactured components. As part of developing the process, studies into the role of microstructure on mechanical properties and phase transformations in deposited material were performed.

Chapter two begins by providing a literature review of the ESD process parameters, to familiarize readers with the deposition technique. A review of Ni-superalloy chemistry, heat treatments, and properties are provided for the two Ni-superalloys used in this thesis: Inconel 718 and Hastelloy X. An introduction to solidification microstructure is given to familiarize the reader with concepts required for later chapters, as well as reviewing previous studies on the solidification microstructure of ESD-processed alloys. Lastly, a literature review of surface post-processing methods applied to laser powder bed fusion additive manufactured parts is provided, to place the proposed application of ESD post-processing in the broader context of surface treatments.

Fundamental studies on microstructure and its influence on properties are presented in chapters three, four, and five. Chapter three identifies a relationship between the thickness of deposited droplets (splats) and the size of the subgrain microstructure in an ESD-processed Ni-superalloy. This is extended to measurements of microhardness, which are found to follow a modified Hall-Petch relationship, relating splat thickness to the hardness of the material. Chapter four identifies the influence of subgrain and splat boundaries on the tensile properties and fracture pathway of repaired cavities. The unique morphology along the fracture surface of tensile tested samples is caused by crack deflection along the subgrain and splat boundaries. This is explained using stress intensity factors and a calculation of the relative critical energy release rate to determine the relative fracture toughness of the two boundaries. Chapter five further investigates the influence of the subgrain microstructure by determining the effect of micro-segregation at subgrain boundaries on phase transformations at elevated temperatures. A nucleation site model is used to compare the availability of nucleation sites in an ESD-processed Ni-superalloy and a homogenized Ni-superalloy, and is found to account for differences in the size of precipitates that form at subgrain/grain boundaries.

A study on the use of electrospark deposition to address the surface roughness of laser powder-bed fusion (LPBF) additive manufactured parts is included in chapter six. Alongside a significant reduction in surface roughness and significant increase in hardness, the fatigue life of Hastelloy X LPBF-made parts was significantly improved with the use of an ESD-processed Inconel 718 coating. Calculated stress intensities for crack propagation from experimentally measured surface features are used to calculate the expected difference in endurance limit stress between as-built and post-processed parts. Fatigue testing shows a significant improvement in post-processed parts for both low and high cycle fatigue conditions. A summary conclusion is presented in Chapter seven, relating to the objectives outlined previously.

Chapter 2. Literature Review

2.1 Electrospark Deposition (ESD) Process

Electrospark deposition (ESD) is a micro arc-welding process that operates by forming a spark between an electrode (anode) and substrate (cathode), which allows for material transfer from the electrode in the form of small droplets. The process is most commonly used for applying corrosion and wear resistant coatings [16–18] to conductive substrates, but has also been used to apply interlayers for the joining of dissimilar materials [19,20]. A diagram of the process is shown in Figure 3. Several parameters influence the ESD process, which are categorized in Table 1 as electrical, mechanical, environmental, and other.

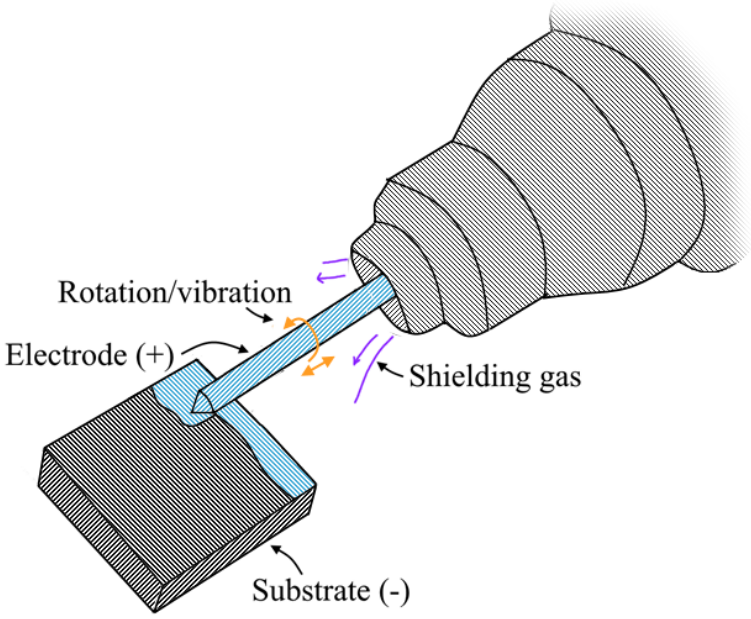

Figure 3. Diagram of ESD process

Table 1. ESD process parameters [21]

Category	**Process parameters**
Electrical	Voltage, capacitance, frequency, system efficiency, spark duration
Mechanical	Travel speed, contact force, contact angle, electrode vibration/rotation, number of passes, track overlap
Environmental	Gas composition, flow rate, temperature, cleanliness
Others	Electrode/substrate materials and geometry, surface finish

ESD functions by rapidly charging a capacitor of a chosen capacitance to a chosen voltage level. Contact between the electrode and substrate results in discharging of the capacitor and delivers a short-duration, high-current pulse [22]. From a physical standpoint, voltage has the effect of regulating the maximum arc gap between the electrode and substrate [23], while the capacitance regulates the duration of the arc. A frequency parameter – controlled by a logic driven thyristor circuit, is used to limit the number of discharge events. Of the many parameters that influence the ESD process, the electrical parameters are typically the most significant [24]. The energy output during ESD is governed by Equation (1), which has a square dependence on the capacitor charge voltage (V) and linear dependence on capacitance (C). The influence of an effective frequency (f) on the power output is seen in Equation (2).

$$E = \frac{1}{2} C \times V^2 \quad (1)$$

$$P = E \times f = \frac{1}{2} C \times V^2 \times f \quad (2)$$

The deposition rate has been shown in the literature to be functions of energy [23,25], with increased capacitance and/or voltage parameters resulting in higher temperatures and greater electrode melting. Frequency has a similar role, with more mass transfer events increasing both the temperature of the electrode and substrate [26], and the deposition rate [27].

In addition to the electrical parameters, the ESD process is also influenced by several mechanical parameters. Two of these include travel speed and electrode force. A decrease in material transfer occurs when travel speed is increased, since heat buildup decreases when discharge events are spaced further apart and the electrode is moved to a cooler region of the substrate [26]. The electrode force influences the average discharge gap, with lower forces resulting in a larger distance between the electrode and substrate. The discharge gap size has been reported to influence the amount of material transferred due to changes in the mass transfer mechanism [26,28]. In general, material transfer is shown to increase up to a certain gap size and decrease afterwards.

Although the aforementioned electrical and mechanical process parameters are the most commonly optimized parameters, ensuring good quality depositions requires the consideration of all parameters in Table 1 to varying degrees. This is more easily performed with automated ESD systems [29,30] than manual systems, since they can control parameters which are otherwise dependent on the skill of the operator, such as force, travel speed, track overlap, and contact angle.

2.2 Ni-superalloys

Ni-superalloys encompass a group of high-performance alloys used in a variety of extreme environments including structural and rotating airplane turbine engine parts [31,32] and critical sections of the space shuttle main engine [33]. As the name suggests, these alloys are primarily composed of a face-centered-cubic (fcc) Ni matrix, but also contain alloying elements that can be tuned to obtain the desired properties. Some elements such as chromium contribute to excellent corrosion and oxidation resistant properties, while other elements contribute to one of two primary mechanism that gives these alloys their high strength at elevated temperatures. Table 2 presents the composition of two Ni-superalloys used in this work: Inconel 718, a precipitation strengthened alloy also referred to as alloy 718, and Hastelloy X, a solid solution strengthened alloy.

Table 2. Composition (wt%) of two nickel superalloys [34,35]

Material	**Ni**	**Cr**	**Fe**	**Mo**	**Nb**	**Ti**	**Al**	**W**	**Co**
Inconel 718	50-55	17-21	Bal. (17)	2.8-3.3	4.75-5.5	0.65-1.15	0.2-0.8	-	< 1.0
Hastelloy X	Bal. (47)	22	18	9	< 0.5	< 0.15	< 0.5	0.6	1.5

The solid solution strengthening mechanism in these alloys occurs primarily due to the presence of large solute atoms (such as Mo, Cr, or W) at lattice sites typically occupied by Ni atoms. The stress field formed around a substitutional atom interacts with the stress fields around dislocations, impeding their motion. Precipitation strengthening instead works by the formation of small hard particles that impeded dislocation motion. In the case of coherent precipitates that align with the crystallographic structure of the matrix, dislocations are more likely to interact via a shearing mechanism, whereas dislocations are likely to interact with incoherent precipitates via an Orowan bowing mechanism [36]. In most Ni-superalloys, precipitation strengthening is attributed to the Nb, Ti, and Al alloying elements that form Ni_3Nb-γ" and $Ni_3(Al,Ti)$-γ' precipitates after heat treatment. With Inconel 718 having greater Nb and Ti+Al than Hastelloy X, the extent to which the precipitation of γ" and γ' affects the properties is greater. Due to the minimal quantities of Nb, Ti, and Al in Hastelloy X, it is not considered precipitation strengthenable. Instead, the mechanism by which Hastelloy X obtains its high strength is through solid solution strengthening and is unique in comparison to Inconel 718 in its addition of W. The large atomic size of W in comparison to Ni results in a significantly greater solid solution strengthening effect when W atoms are located at lattice sites.

A typical heat treatment process for Inconel 718 is shown in Table 3, which begins with a solution annealing step and is followed by a two-step aging treatment. The objective of solution annealing is to dissolve and evenly distribute alloying elements back into the Ni matrix, such that they evenly and fully form the γ" and γ' precipitates throughout the material during aging. At the conclusion of heat treatment, properly precipitated γ" and γ' phases are approximately 15-20 nm in size, with further exposure to temperatures above 650 °C (but below the solutionizing temperature) resulting in further growth [37]. Coarsening of these phases leads to a decline in strength and hardness, and exposure to some elevated temperatures can lead to phase transformations that also influence the properties of Inconel 718. Table 4 summarizes the composition and structure of phases in Inconel 718.

Table 3. Solution annealing and aging heat treatments for Inconel 718 [34]

Heat Treatment	**Time (h)**	**Temperature (°C)**
Solution annealing	1	925 - 1010
Precipitation	8	720
hardening (aging)*	10	620

* Two step process, furnace cooled between steps, air cooled after aging

Table 4. Composition of phases in Inconel 718 [38,39]

Phase	**Composition**
γ"	Ni_3Nb
γ'	$Ni_3(Al,Ti)$
Carbides	(Nb,Ti)C, (Ti,Nb)CN
δ	Ni_3Nb
Laves	$(Ni,Fe,Cr)_2(Nb,Mo,Ti)$

The formation of the δ phase occurs after exposure to temperatures between 700 °C and 1000 °C [40] and can be detrimental to the properties of the nickel superalloy [41]. Since it has the same composition as the γ" phase – but different crystal structure and morphology – it generally forms at the expense of the more favourable γ" phase, and can occur from the partial dissolution of γ" and subsequent transformation to δ [42]. Exposure to temperatures between 1005-1020 °C,

depending on Nb content in the material, is effective at achieving full dissolution of the δ phase [40]. However, some benefits can be expected, such as its ability to inhibit grain growth [40,41] and resist creep when forming along grain boundaries [38]. As such, the δ phase is typically unwanted but can be carefully controlled to improve certain properties.

The role of carbides – like the δ phase – displays positive and negative attributes, with some grain growth inhibition and some contribution to high temperature strength through grain boundary pinning countered by their ability to promote intergranular failure [39]. Formation can occur by two different mechanisms. The first occurs during solidification, where segregation of Nb and C into the liquid phase encourages formation of NbC in addition to the Laves phase [39]. Formation of NbC and Laves phase both occur at the expense of the γ" phase, although unlike the transition from γ" to δ, the NbC and Laves phases trap Nb and prevent later formation of the γ" during aging heat treatments. The second mechanism is by exposure to temperatures above 700 °C. The formation of carbides is found to be highly sensitive to the alloy composition, with changes in the quantity of nucleating particles (such as TiN), the quantity of carbon, and Nb homogenization greatly influencing the extent of carbide (and other phase) precipitation [43,44].

The Laves phase forms due to elemental segregation during solidification. Like the carbide and δ phases, the Laves phase has demonstrated both a positive and negative influence on the mechanical properties of Inconel 718. Laves phase particles can act as an impediment to crack propagation, or act as a crack initiation site, depending on the type and magnitude of applied loading [45]. At low stress amplitudes, the high-cycle fatigue life of Laves containing Alloy 718 is greater than that of material in the cast condition, although at high stress amplitudes the Laves phase is found to be detrimental [45]. The influence of the Laves phase is also reported to depend on morphology, with granular particles exhibiting better properties than a higher-aspect ratio Laves phase during tensile testing [46].

During solidification processes, the formation of a solidification microstructure with secondary phases and micro-segregation can influence the properties of these alloys in the as-deposited or heat-treated conditions, as well as during use. These have the potential to directly affect mechanical properties, as well as affecting the proper formation of γ" and γ' strengthening phases in precipitation hardenable alloys which depend on the availability of the alloying elements that form

those phases. The following section provides a review of solidification and the formation of a solidification microstructure.

2.3 Solidification Microstructure in ESD-processed Ni-superalloys

Solidification begins with nucleation of the solid phase from the liquid phase. This can occur homogeneously in the liquid, or heterogeneously at pre-existing surfaces. As a solid particle forms within a liquid (Figure 4), the favourable free energy change associated with the creation of a solid volume (ΔG_V) is opposed by the unfavourable free energy change associate with the creation of a solid/liquid interface (ΔG_S). Below the critical radius (r*), any solid embryos formed due to short range fluctuations in thermal energy will favour dissolution, while growth is favoured if the solid is greater than the critical radius. Due to this energy barrier, solidification via homogeneous nucleation often requires significant thermal undercooling below the freezing temperature. However, during welding and deposition processes, other surfaces are available for heterogeneous nucleation. In the presence of an already existing surface, the unfavourable change in interfacial energy is reduced and the critical free energy change (ΔG^*) is reduced as well. This makes it possible for nucleation to happen without thermal undercooling or with a significantly smaller thermal undercooling, since the smaller energy barrier for heterogeneous nucleation can be fully or mostly overcome by the naturally occurring thermal energy variations.

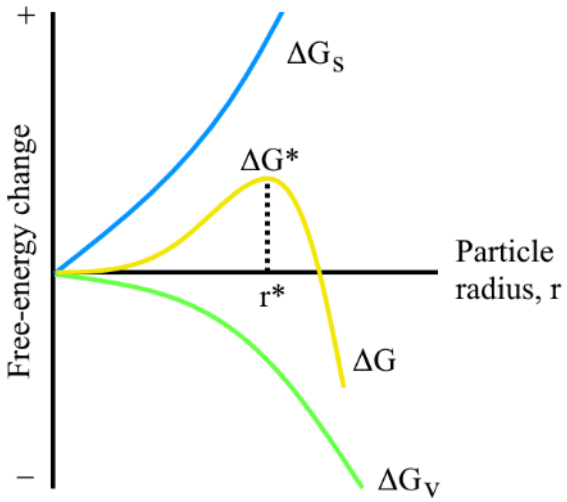

Figure 4. Free energy change during the formation of the solid phase in liquid

For the deposition of a metal alloy, the substrate frequently acts as the surface on which nucleation occurs. When the deposited material and substrate share a similar crystal structure and composition, the crystallographic orientation of the newly formed solid shares the orientation of the substrate [47]. The resulting solid forms epitaxially, growing perpendicular to the solid/liquid interface. As such, grains can extend across the substrate/deposition boundary and those oriented more favourably will outcompete and block neighbouring grains [48]. Anisimov et al. [49] identified most of the grains in an Inconel 718 ESD coating as having the <100> direction aligned with the build direction, even though the substrate was composed of misoriented grains. In face-centered-cubic (fcc) and body-centered-cubic (bcc) metals, how closely a grain's <100> crystallographic direction is aligned with the thermal gradient dictates how favourable the grain growth will be and how dominant that grain will become over its neighbours.

Solidification can be expected to result in one of four modes that describe the morphology of the solid/liquid interface. A planar morphology is more frequently observed in pure metals, and less frequently seen in alloys due to the potential for constitutional supercooling. This is the result of partitioning of alloying elements, which cause local variations in composition in front of the solid/liquid interface [48]. With changes in composition, the liquidus temperature is also affected. If the actual temperature ahead of the solid/liquid interface is below the new liquidus temperature, the solid/liquid interface becomes unstable and protrusions develop, as depicted in the cellular and columnar dendritic diagrams in Figure 5. Many studies identify an intermediate solidification microstructure, known as cellular dendritic, in which the growth of the secondary dendrite arms is stunted [47]. In situations with an even larger constitutional supercooling, an equiaxed dendritic solidification mode is possible, in which a solid crystal grows ahead of the solid/liquid interface.

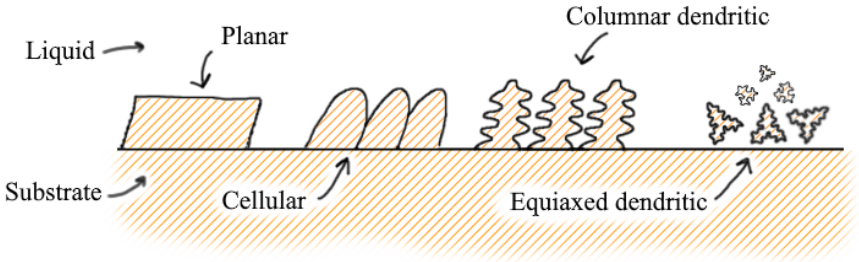

Figure 5. Depiction of planar, cellular, columnar dendritic, and equiaxed dendritic solidification microstructures

The type of solidification mode that occurs is determined by a combination of two parameters: the temperature gradient (G) and the growth rate (R). A very high temperature gradient or very low growth rate, which are features of solidification with no constitutional supercooling, can result in planar growth. On the other end, a very low temperature gradient or very high growth rate, both features of a large constitutional supercooling, can result in equiaxed dendritic growth. This is frequently depicted in plots of G vs. R as shown in Figure 6, where the slope G/R is indicative of the solidification microstructure that forms. The microstructure size is determined by the cooling rate, which is the product of the thermal gradient and the growth rate (G×R). Average cooling rates during ESD of up to 10^6 K/s have been frequently mentioned in literature, and measurements of the solidification microstructure size support these cooling rates. Xie and Wang [50] calculate an average cooling rate on the order of 10^5 K/s based on a primary cell spacing of 800 nm in a Ni-superalloy. Ebrahimnia et al. [51] use the solidification microstructure of an ESD-processed, laser-processed, and as-cast Ni-superalloy to compare the average cooling rates in each process. Their finding suggest that the cooling rates are on the order of 10^6 K/s, 10^3 K/s, and 10^0 K/s, respectively. However, maximum cooling rates in an ESD process can be significantly higher, up to 10^9 K/s, as calculated by Gould [20].

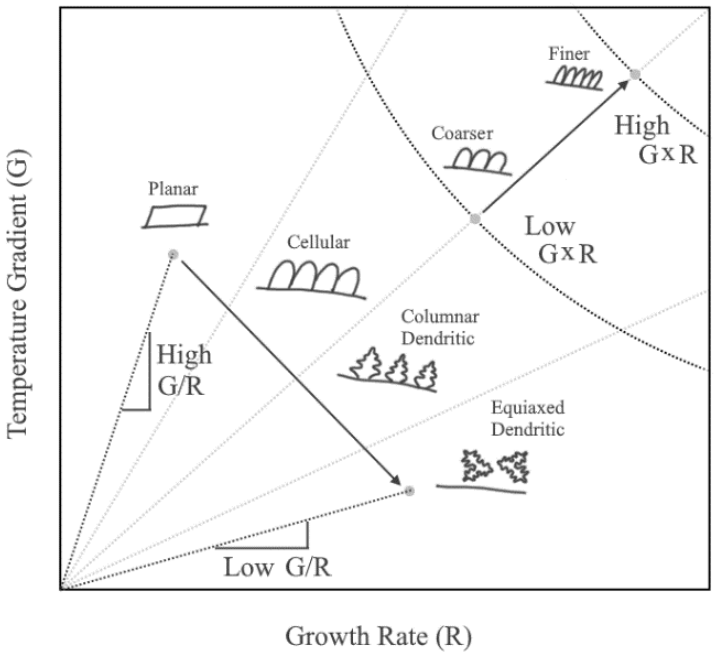

Figure 6. Solidification microstructure depending on temperature gradient and growth rate, adapted from [47,48]

The protruding features in the more frequently observed cellular and columnar dendritic microstructure form an epitaxial subgrain structure that remains after solidification is complete. Within a single grain, adjacent subgrains typically have only a slight misorientation and form low angle boundaries (misorientation angle typically <5° [47]). Additionally, with the partitioning of alloying elements and the formation of a segregated liquid at the terminus of solidification, subgrain boundaries can be enriched in certain alloying elements (Figure 7).

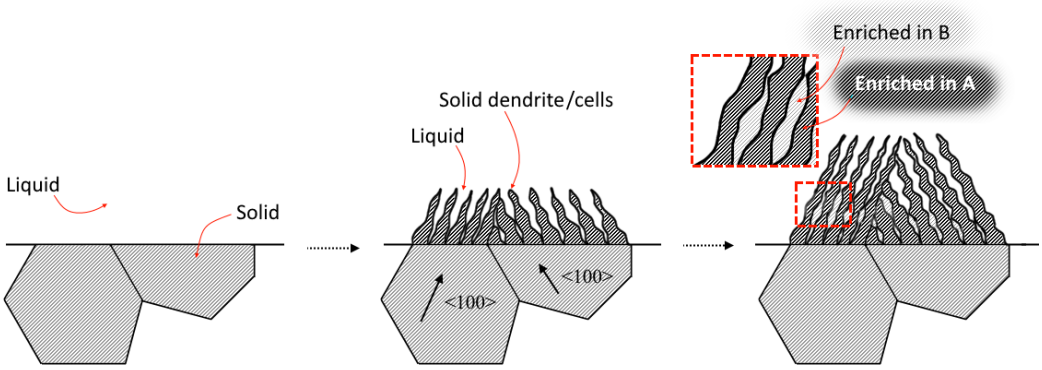

Figure 7. Schematic depiction of cellular dendritic growth from two substrate grains and micro-segregation at the cell boundaries

Micro-segregation at subgrain boundaries occurs due to differences in solubility of the elements within an alloy and a limited ability to redistribute segregated elements [47]. On the short timescale in which solidification during welding typically occurs, diffusion in the solid occurs too slowly to provide any notable redistribution of elements. When considering the liquid phase, both diffusion and convection are possible redistribution methods, and conditions can range from allowing long-range mass transport (diffusion and convection) to only allowing short-range mass transport (limited diffusion and no convection). Although the extent of segregation changes between these conditions, the result in all three cases is similar: for an element with an equilibrium partition coefficient k_e < 1, such as Nb in Inconel 718 [52], the first solid that forms is depleted of the element and the final solid that forms at the subgrain boundaries is enriched.

Micro-segregation in ESD-processed materials has been frequently discussed in the literature. The high cooling rates and rapid solidification that occurs during ESD has the potential to result in solute trapping. Under these solidification conditions, diffusion occurs too slowly even in the liquid phase to result in solute partitioning, such that a solid phase forms with more limited micro-segregation than would be expected from the equilibrium partition coefficient. Evidence of some

solute trapping was demonstrated by Heard et al. [53] for an ESD-processed Al-Li-Cu alloy (AA2199). Li, with a k_e of 0.55, was homogeneously distributed throughout the material at the conclusion of solidification while Cu, with a k_e of 0.15, segregated at the subgrain boundaries. Therefore, although solute trapping arises due to rapid solidification during ESD, micro-segregation is still expected to occur for some alloying elements. In Inconel 718, Nb has a similarly low k_e of 0.2 [52] as Cu in AA2199 and has similarly been reported to segregate at subgrain boundaries. Vishwakarma et al. [54] shows the segregation of Nb at the subgrain boundaries of ESD-processed Inconel 718 resulting in the formation of Nb-rich phases. However, an effective partition coefficient k of 0.5 was measured. This suggests that while some solute trapping may be occurring, it is not sufficient to result in a fully homogenous Inconel 718 deposit.

Without the use of a post-process heat treatment, several aspects of the solidification microstructure – including the subgrain structure and the micro-segregation at boundaries – remain in the deposited material. These features require further consideration, to determine how mechanical properties are affected and to identify suitable applications for ESD-processed Nb-rich Ni-superalloys.

2.4 Surface modification of LPBF-made parts

Poor surface quality in LPBF-made parts is attributed to partially fused powders, spatter, and the underlying melt tracks, and typically requires processing prior to use in high performance applications. The following sections discuss some of the more common surface post-processing techniques that have been applied to LPBF-made parts, spanning mechanical and thermal-based methods.

2.4.1 Mechanical techniques

Mechanical surface modification techniques encompass the more traditional machining, abrasive, and impact treatments frequently used in industry. Machining encompasses several subtractive processes performed by machine tools, some of which use rotating cutting tools to remove material from a fixed workpiece (milling in Figure 8a) or fixed cutting tools to remove material from rotating workpieces (lathe). LPBF parts subjected to this post-processing step are typically printed larger than the required dimension, with material removed until the required dimensions are

obtained. Although this produces material waste and is difficult to use on complicated geometries or work hardening materials, machining is commonly used due to its frequent application in traditional manufacturing and the ability to easily obtain a low final roughness regardless of the initial roughness. As shown by Rotella et al. [55] the result of machining on a CNC lathe is a surface roughness (Ra) of 1-2 µm, which is significantly lower than as-built LPBF parts (10-20 µm) but not as good as an equivalent wrought material processed with the same cutting speeds. This is attributed to the lower ductility of LPBF parts and suggests that a properly optimized machining process must not only consider the material's composition but also properties arising from its previous processing conditions. Lizzul et al. [56] demonstrated that the surface roughness achieved from milling is dependent on LPBF part orientation. Anisotropy in the grain structure – which arises from preferred grain growth in the build direction – affects the cutting tool wear rate and decreases tool life by up to 40% when machining surfaces. Generally, increasing cutting tool wear resulted in more material adhesion on the tool and more burr formation on the LPBF-made part, increasing the surface roughness.

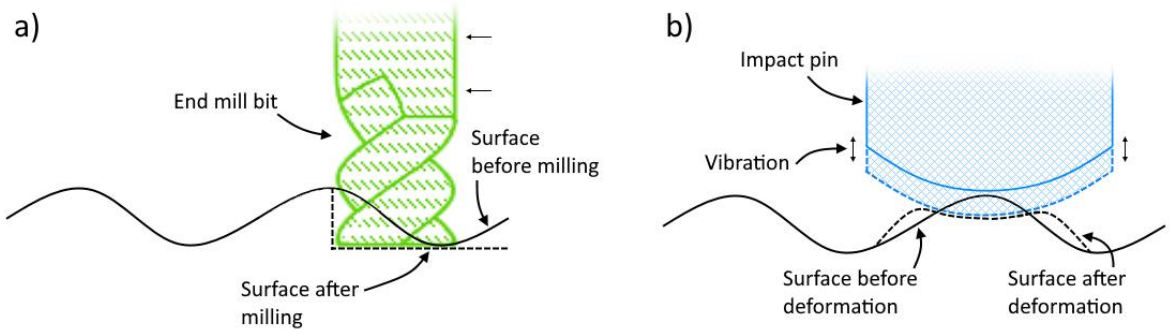

Figure 8. Mechanical surface modification process showing a) milling and b) impact treatment of a surface

Machining processes can either be performed out-of-envelope – in which the printing and machining are performed on separate machines – or with hybrid in-envelope systems that are capable of both functions. Out-of-envelope systems allow for intermediate post-processing steps such as heat treatments that relieve residual stresses caused by the LPBF process and increase ductility. Heigel et al. [57] demonstrated that when machining on an end mill is performed on as-built LPBF parts without heat treatment, a combination of LPBF-induced stresses and machining-induced stresses or phase changes can result in a distorted final part. Due to the spatial variations

in LPBF-induced residual stresses that range from tension to compression, and the other factors that arise during machining, accurately predicting the amount of distortion is difficult. Another challenge with machining is the reduction of surface roughness on internal channels or more complex lattice geometries. In these cases, other post-processing techniques are likely required.

Abrasive polishing spans a large range of post-processing techniques that use hard particles to remove surface asperities. A variety of bonded abrasive techniques such as sanding and grinding exist, although most are labour intensive and not realistically suitable for high production volumes, large parts, or internal channels. Alternatively, loose abrasive techniques can rely on fluid flow or simply the movement of a dry abrasive to provide the relative motion between hard particles and the part surface. Magnetic field-assisted polishing demonstrated by Yamaguchi et al. [58] on LPBF-made parts uses a mixture of abrasive slurry and magnetic particles in a magnetically driven device. The applied magnetic field causes the magnetic particles to press the abrasives into the part surface, while rotation of the magnet removes material by inducing relative motion between the abrasive particles and the part surface. Another loose abrasive post-processing technique is that of barrel finishing, demonstrated by Boschetto et al. [59] to polish external surfaces of specimens using an abrasive alumina, silica and silicon carbide mixture. This technique uses a rotating barrel to induce relative motion between the abrasive particles and the LPBF-made parts, with the rotational speed and build orientation influencing the time required to obtain a low surface roughness. Vibratory finishing is a similar technique that achieves its relative motion by vibrating a tub containing the parts to be polished and the abrasive particles. Although these techniques are limited to parts smaller than the size of the barrel or tub, require long processing times, and result in part dimension deviations that must be considered during the design stage, a significant reduction in surface roughness is possible.

Abrasive flow machining, also known as extrude honing, appears well suited to address difficult-to-reach internal channels, as shown by Duval-Chaneac et al. [60]. Increases in the abrasive concentration and fluid viscosity were both found to decrease the surface roughness, while compressive stresses on the part were affected by the relative contribution of ploughing versus cutting as the material removal mechanism. As shown by Han et al. [61] this post-processing technique can be applied to conformal cooling channels that would be impossible to post-processes with most other techniques. Velocity of the abrasive media was identified as a key factor in

determining surface roughness reduction; shorter channels resulted in higher flow velocity and a greater reduction in roughness, achieving a surface roughness comparable to conventionally molded cooling pipes. Nagalingam et al. [62] combines an abrasive flow machining technique with a hydrodynamic cavitation erosion mechanism for reducing surface roughness. With appropriate design of the fluid flow, bubbles form along the surface of internal channels, which collapse and create fast moving jets that erode material from the surface. However, if parts are not printed larger than their intended final dimensions, both the abrasive and machining techniques discussed so far are detrimental to assembly tolerances. Even with this in mind, controlling deformation in machined parts and achieving uniform wear rates in abrasively polished parts is challenging.

Unlike subtractive machining and abrasive post-processing options, impact techniques mainly rely on plastically deforming protruding features on a part surface to reduce the roughness. Processes such as ultrasonic impact treatment are typically performed by vibrating a hardened pin at frequencies from 15 and 55 kHz and making physical contact between the vibrating pin and the workpiece (Figure 8b). Zhang et al. [63] and Walker et al. [64] demonstrated improvements in the fatigue life of postprocessed LPBF-made samples, while Xing et al. [65] demonstrated an improvement in stress corrosion resistance. These property improvements are attributed to plastic deformation at the surface introducing compressive residual stresses alongside a reduction in surface roughness and an increase in near-surface hardness. During cyclic loading, the increased hardness and reduced surface roughness delayed crack initiation while the compressive stresses delayed crack propagation. In the case of stress corrosion cracking, the presence of a tensile stress due to temperature gradients during LPBF manufacturing makes them susceptible to this failure mechanism. Other impact treatments such as shot-peening, which uses loose metal, glass, or ceramic balls to strike a surface at high velocity, also show improvements in the fatigue performance of LPBF-made parts [66]. Depending on the material and parameters used, the process of impacting a surface can introduce new longer-range features that increase the surface waviness while still reducing roughness [67]. However, the ability of impact treatments in general to relieve near-surface tensile stresses make them a beneficial post-processing choice that can address more than just surface roughness.

2.4.2 Thermal techniques

Several thermal-based post-processing methods have demonstrated improved surface conditions for LPBF additive manufactured parts. Some of the main benefits when compared to conventional grinding or machining is the lack of tooling wear, potentially faster processing, and reduced material waste or debris. Thermal input is not limited to lasers, with plasma and spark-based techniques [68] having been demonstrated in literature. However, the use of lasers in the LPBF process makes them a popular choice when selecting a post-processing treatment. Three laser-based techniques are discussed in this section, which include laser polishing, laser ablation, and laser peening.

A laser polishing process makes use of laser radiation to locally melt surface asperities. At lower energy densities, the melted surface thickness is less than the peak-to-valley height of the surface roughness, and surface tension redistributes the molten material to local valleys on the surface (Figure 9a) [69]. At higher energy densities, surface features are modified by melting a thickness of material greater than the peak-to-valley height. Both techniques have been used in recent studies to show that the as-built surface morphology – which shows repeating features on the order of the beam diameter used during LPBF and the presence of partially fused powders – can be eliminated.

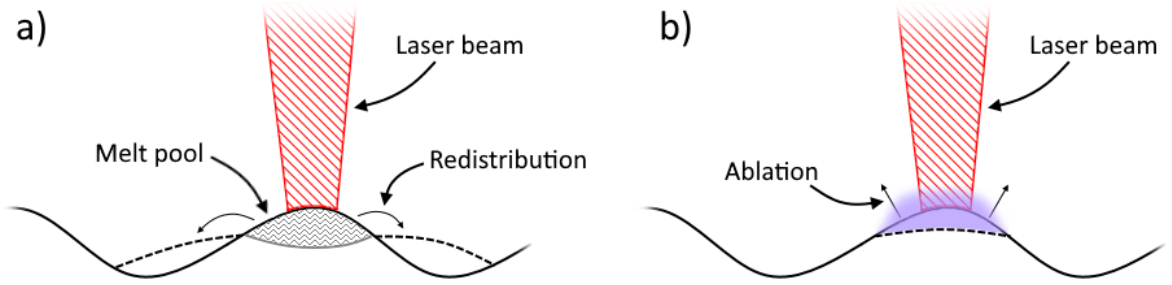

Figure 9. Laser surface modification showing a) laser polishing at lower energy densities resulting in material redistribution and b) laser ablation resulting in the removal of material

Several authors have demonstrated the use of continuous wave lasers for polishing of LPBF parts. Obeidi et al. [70] optimized laser power, travel speed, and track overlap parameters to obtain a reduced surface roughness with a single laser pass. Without optimal parameters, difficulty arose in melting the highest peaks on the as-built surface, which is an even greater concern in parts with high initial surface roughness. When a single pass is insufficient to fully melt the initial surface

features, or a very low surface roughness is required, Chen et al. [71] demonstrated that multiple laser passes are an effective option. Both studies identified that laser polishing has the potential to introduce new repeating features on the surface of the part and increase the surface roughness if not properly optimized.

Operation in the high energy density keyhole regime has been shown by Richter et al. [72] to be beneficial for surfaces with high initial roughness by removing longer wavelength features. Although high energy density process parameters may be beneficial for one-pass laser polishing, it also has the potential to introduce defects. Solheid et al. [73] found that as laser power increased, cracking occurred adjacent to the melt tracks. Further increases in energy density resulted in a greater contribution from laser ablation rather than surface re-melting, which increased the amount of surface oxidation.

Chen et al. [71] found that due to grain refinement and surface roughness reduction arising from laser polishing, the sub-surface hardness and corrosion resistance were both significantly improved in stainless steel 316L parts. Yasa et al. [74] extends this grain refinement process to modify bulk properties by using laser polishing after each individual layer of the LPBF part was manufactured. Although this results in longer processing times, properties such as bulk density, surface roughness and microhardness could be tailored. Roughness that forms as each layer is melted hinders the uniform coating of a new layer of power during the LPBF process. With non-uniform powder thickness or incomplete coverage of the surface, gas entrapment may occur, and porosities may form. Laser polishing each layer re-melts and removes porosity while also reducing the roughness, having been shown to improve LBPF part density from 99.23% to approximately 99.97% [74].

Methods based on laser ablation typically rely on the high energy density achievable with short-duration pulsed lasers rather than continuous lasers. Irradiation results in metal vaporization from a thin region of the part surface with limited melting. This surface evaporation results in the formation of an ionized plume that contributes to the absorption of incident laser energy and significantly limits the ablation depth [75]. As such, the reduction in roughness is mainly attributed to material removal from the surface (Figure 9b) rather than the melting and redistribution mechanisms observed in laser polishing.

Černašėjus et al. [76] exploited the localized surface heating that occurs during an ablation process to perform laser gas alloying on a steel LPBF part surface. In an ambient air environment, the

oxygen concentration at the surface is a function of laser power and laser scanning speed, with an increase in energy density resulting in greater oxygen uptake due to greater heating and slower cooling rates. Although the reduction in surface roughness achieved with one laser pass is lost after repeated laser passes, the formation of iron/titanium cobalt oxides and notable 35% increase in hardness resulted in up to a 17-fold reduction in mass loss during wear. As such, oxidation of the surface that frequently occurs in laser ablation processes when performed in ambient environments may be beneficial in some applications.

2.4.3 Combining surface post-processing techniques

It is not uncommon to require a combination of techniques to achieve the desired surface roughness reduction and mechanical property improvement. Some surface post-processing methods can efficiently remove large surface roughness features quickly, whereas other techniques are ideally suited to removing smaller features sizes and achieving very low surface roughness. Several examples exist in literature where multiple post-processing steps are applied. A reduction in surface roughness of 93% to below 1 µm was demonstrated by Loaldi et al. [77] by combining three post-processing techniques, although the significant improvement in surface finish is offset by the increase in cost and processing time. A similar reduction in roughness was demonstrated by Anilli et al. [78], with an 80% reduction achieved using two sequential techniques. Their analysis of a functional component demonstrates that a combination of post-processing steps can obtain LPBF-made parts that perform equally well or better than that of conventionally manufactured parts. Although machining and laser surface post-processing are the more common mechanical and thermal techniques applied to LPBF-made parts, other mechanical-thermal combinations such as hammer peening and electrospark deposition can also demonstrate high surface roughness reduction with mechanical property improvements [79].

Chapter 3. Effect of subgrain size on microhardness

3.0 Preface

This chapter is the first of three chapters that studies the influence of the solidification microstructure in ESD processed Inconel 718 on mechanical properties. The first topic of study addresses how the ESD material transfer mechanism, in which droplets of material are transferred and spread onto a surface to form a *splat*, can influence the cooling rate. Differences in cooling rate influence the size of the solidification microstructure and extent of coarsening, while microstructure size is known to affect the strength of a material according to the Hall-Petch relationship [80,81]. Experimental results measuring splat geometry, subgrain size, and microhardness are related by combining equations for heat diffusion, coarsening kinetics, and the Hall-Petch relationship. The final derived equation can relate deposited material thickness to hardness and allows for further control over the properties of ESD Inconel 718.

This chapter is based on a published paper [82].

3.1 Introduction

ESD has found several applications in wear or corrosion resistant coatings and as a repair technique for cracked and pitted components. Sartwell et al. [83] achieved successful mechanical property and dimension restoration for stainless steel, Inconel, and nickel-copper alloy components, the assessment of which was based on porosity, microhardness, wear resistance, tensile and fatigue testing, and surface finish analysis. These applications benefit from a deposited material with properties equivalent to – or better – than the base metal, which can be achieved through a finer grain structure. The Hall-Petch relationship indicates that smaller grain sizes result in a greater yield strength, alongside other improvements to ultimate tensile strength, hardness and wear resistance [36].

Nanoscale grains have been reported to form in various electrospark deposition (ESD) processed materials including aluminum-zirconium alloys [84] and Fe_2B [85]. These small grain sizes are attributed to the short pulse duration of the ESD process, allowing for rapid solidification and cooling of the material between each deposition. The use of ESD to restore oxidation resistant coatings by Farhat and Brochu [86] found that the performance of the repaired coating was

improved due to the fine grain structure of the deposited material, which allowed for improved diffusion along the grain boundaries. Improved tribological properties (increased wear resistance) of nanoscale structured ESD WC-Co coatings have also been reported in the literature [87]. The improved properties were directly attributed to the nanostructured coating, which resulted in increased hardness and the formation of lubricating oxides.

Ruan et al. [88] showed that decreasing dendrite diameter and secondary dendrite arm spacing both resulted in a microhardness increase, analogous to the Hall-Petch relationship. The presence of cellular dendritic structures in ESD processed materials have been reported for nickel based superalloys by Ebrahimnia et al. [89], which formed parallel to the ESD growth direction with submicron diameters. Other rapid solidification processes exhibit similar cellular dendritic structures for nickel-based superalloys, including laser powder bed additive manufacturing of Hastelloy X [90]. In this process, cellular dendritic structures with primary arm diameters less than 1 μm and no secondary arm formation were attributed to high cooling rates. Although the presence of subgrain structures is well documented, the ability to control the dendritic subgrain diameter in an ESD process is beneficial for optimizing mechanical properties. A model based on a subgrain coarsening mechanism is developed and used to relate the deposition splat thickness with the cellular dendritic subgrain diameter, as well as describing the effect of splat thickness on hardness in ESD processed Inconel 718.

3.2 Materials and methods

An Inconel 718 sheet obtained from McMaster-Carr was used as the substrate material for the ESD process. The substrate surface was 6 cm^2 and the substrate thickness was 3.2 mm, with the supplier provided chemical composition listed in Table 5. Inconel 718 solution-treated electrodes obtained from AlloyShop with a 3.2 mm diameter were used.

Table 5. Inconel 718 Substrate Composition (wt%)

Ni	**Fe**	**Cr**	**Nb**	**Mo**	**Ti**	**Co**	**Al**	**C**	**Mn**	**Si**	**Cu**
53.5	17.8	18.5	5.1	2.9	0.9	0.2	0.6	0.03	0.09	0.08	0.13

The deposition process was performed using a Huys Industries ESD machine. A process window varying several process parameters was used to obtain depositions with low and high energy

parameters. Due to the effect of capacitance and voltage on the input energy of the ESD process, several voltage and capacitance values were used while maintaining constant pulse frequency. These parameters are summarized in Table 6. Argon cover gas was used at a flow rate of 10 L/min and the material was deposited in a bidirectional raster scan pattern for each sample. Deposition time was kept constant by manually controlling the electrode travelling speed, with a single pass on a 1 cm^2 area requiring 20 seconds of coating time. A total of 10 passes were performed for each sample, with a 10 second peening step using a hand-held motorized tool after each pass. The use of a peening step leads to a reduction in surface roughness, improving the uniformity of subsequently deposited layers.

Table 6. ESD Process Window

Parameter	**Value(s)**
Pulse Frequency (Hz)	170
Voltage (V)	50, 100, 120
Capacitance (µF)	80, 100, 120

One sample was created for each process parameter and the samples were cross-sectioned and mounted in a conductive resin, after which they were subjected to a series of grinding (400, 600, 800 and 1200 grit) and diamond polishing (6, 3, 1 µm) steps. The samples were then etched by immersion using inverted glyceregia ($HCl:HNO_3$:Glycerol in a 5:1:1 ratio) for 1.5 and 3.5 minutes [91], with a shorter time required to etch the deposited material and a longer time required to etch the substrate.

Analysis of the prepared samples was performed on a JEOL JSM-6460 scanning electron microscope (SEM) with an Oxford Instruments INCAx-sight EDX attachment and an Oxford BX51M optical microscope (OM). Subgrain diameter measurements were performed using the intercept method for grain size determination (ASTM E112-13), modified to account for the cellular dendritic shape. A line of known length was drawn perpendicular to the subgrain growth direction, and the length was divided by the number of intersected subgrains to get the average subgrain diameter. Hardness measurements were made using a load of 0.1 kgf on a Wolpert Wilson 402 MVD micro Vickers hardness tester. Indentations on the boundary between deposition splats were avoided.

3.3 Results and Discussion

Microscopic analysis of ESD deposited Inconel 718 after etching shows a series of individually deposited splats with varying thicknesses that stack to form the coating. Higher voltage and capacitance parameters result in higher deposition rates and poorer coating quality, as seen in Figure 10a, while lower parameters result in favourable coatings with no significant voids or cracks (Figure 10b).

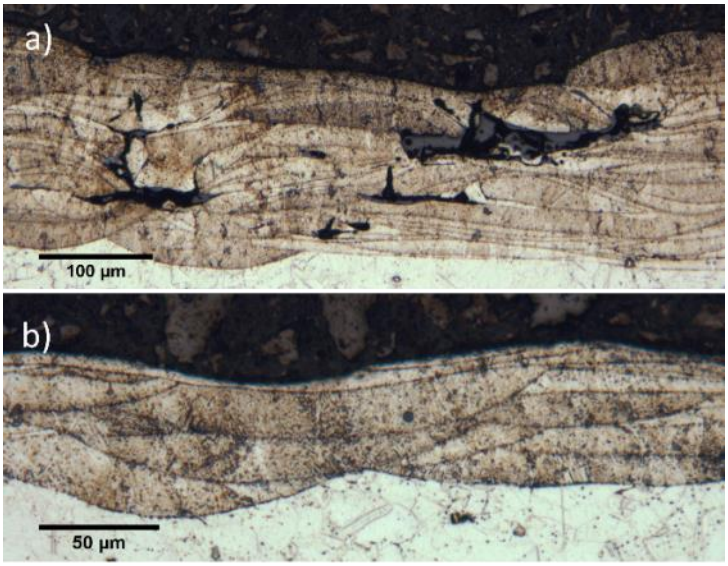

Figure 10. OM image of a) 120 V, 120 µF, 170 Hz ESD deposition and b) 100 V, 80 µF, 170 Hz ESD deposition

The ESD process deposits material through a series of short electrical pulses determined by the frequency parameter, with each of these pulses depositing a single splat on the substrate surface. The rapid cooling rates associated with ESD allow for the deposited material to solidify prior to the deposition of a subsequent splat, forming the layered microstructure in Figure 10. As can be seen by the uneven substrate-deposition interface, some of the substrate is melted during the deposition of the first layer. Higher magnification images of the deposited layers show large regions with submicron cellular dendritic subgrains, seen in previous work on the deposition of nickel alloys using ESD. Ebrahimnia et al. [89] identified these subgrains are being composed of primary dendrite cells with no secondary dendrite structures, comparable to that identified by Savage et al. [92] as occurring during cellular dendritic solidification modes in copper-nickel alloys.

These cellular dendritic subgrain structures are predicted to form epitaxially with the rapid solidification of the deposited layer, where initial subgrain formation starts at the interface of the previous layer or substrate and propagates towards the deposition surface. Figure 11 shows that grain formation is influenced by the substrate grain structure; grain boundaries extend across the substrate-deposition interface, with the structure changing from equiaxed in the substrate to epitaxial in the deposition. Electron backscatter diffraction (EBSD) techniques for an ESD Inconel 738LC deposition show splats with sufficient fusion to the substrate as having the same crystallographic orientation as substrate grains [89]. However, the presence of impurities and lack of fusion defects can result in misoriented growth.

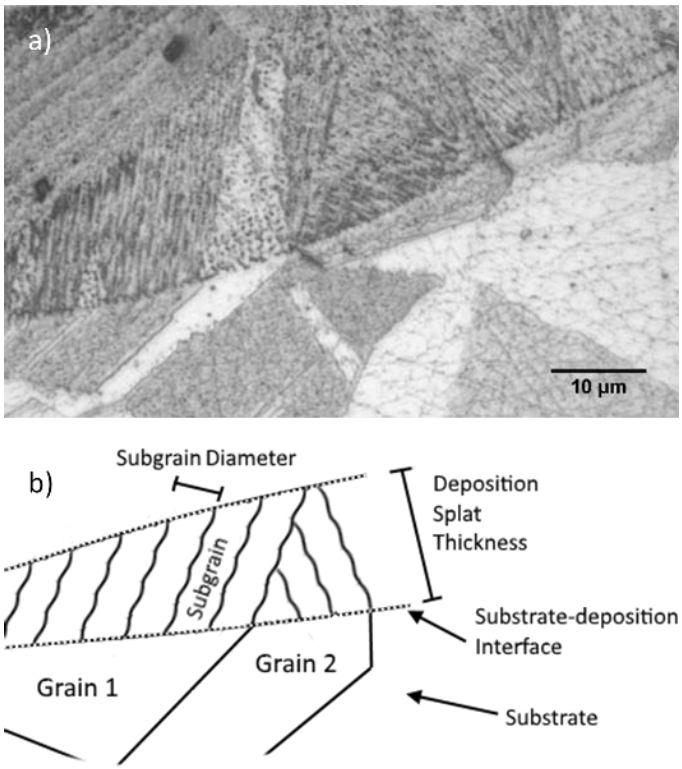

Figure 11. a) OM image along substrate-deposition interface and b) schematic of competitive cellular dendritic subgrain growth directions at the interface

The very thin splat morphology can be expected to result in predominantly unidirectional heat flux within the deposited material during solidification. Figure 12 shows cellular dendritic subgrains of approximately 800 nm in diameter, surrounded by splats with thinner or no discernable subgrain structure. Larger cellular subgrains are visible in etched samples with the use of an optical

microscope, as seen in Figure 12c and Figure 12d. These images more clearly show the existence of competing cellular subgrain growth directions.

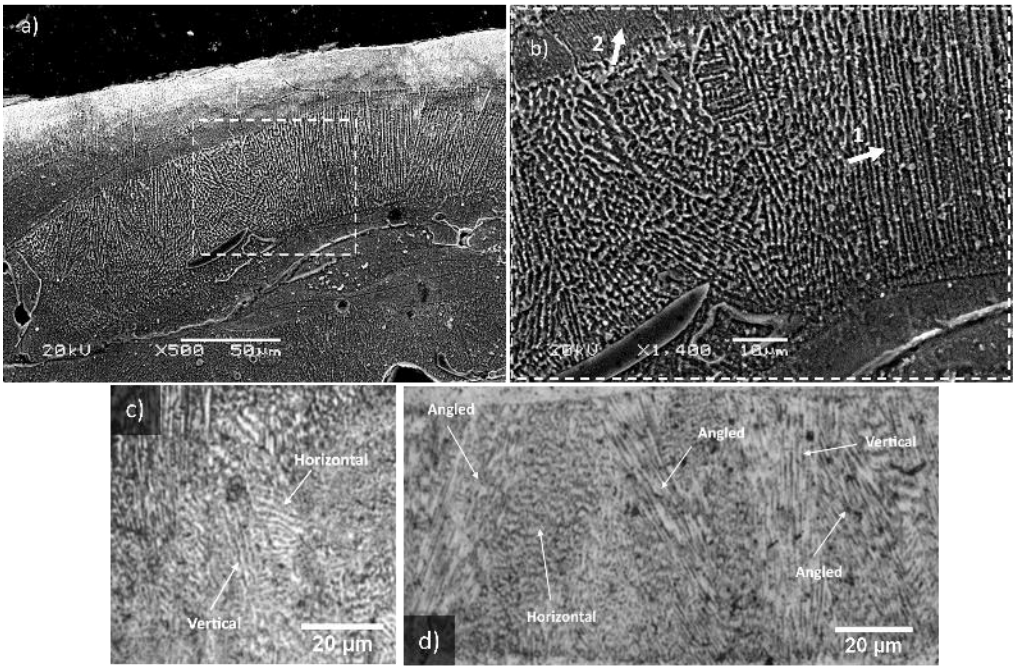

Figure 12. a) SEM image of deposition with cellular dendritic subgrain, b) area of interest, and OM images of competing cellular growth directions in c) a 100 µm thick splat and d) a 70 µm thick splat

During ESD, the cellular subgrains form at the solid-liquid interface as the deposited splat cools below its liquidus temperature. As the material continues to cool, the fine cellular structure is expected to continue coarsening. The amount of coarsening depends on the amount of time the solidified deposition remains at an elevated temperature. In Figure 12, it is possible to distinguish the difference in cellular dendritic subgrain diameters between the individual deposition splats. The subgrain diameter is defined as starting at the inner leftmost edge of a subgrain and extending to the inner leftmost edge of the adjacent subgrain Figure 11), and is calculated using the intercept method as described in the experimental section. Arrow 2 indicates a region with fine cellular structures when compared to the thick deposition splat and thicker cellular structures indicated by arrow 1. The presence of larger diameter subgrains in thicker splats suggests that the thickness of material deposited with each pulse in the ESD process is correlated to the final microstructure.

This premise stems from the larger time requirement for cooling thicker deposition splats. The longer duration at elevated temperatures is expected to act as the mechanism that induces

coarsening, resulting in larger cellular dendritic subgrain diameters for thicker splats. This type of subgrain coarsening has been shown to follow the subgrain growth equation [93],

$$d^n = k_T t + d_0^n \qquad (3)$$

where d is the final subgrain diameter, k_T is a temperature dependent rate constant, d_0 is the initial subgrain diameter, t is the time, and the growth exponent n has a theoretical value of 2 when derived using a boundary migration model in a pure single-phase system. Brook [94] proposed that n ranges between ideal values of 1 and 4 depending on several factors including the presence of impurities in single phase systems, the continuity and mobility of secondary phases, and the diffusion mechanism responsible for boundary mobility. Similarly, k_T is derived from an Arrhenius-type equation that depends on the activation energy of the grain growth mechanism.

The subgrain growth process for ESD is expected to begin with a short-lived nucleation stage during the rapid solidification process. The size of the resulting microstructure is attributed to a combination of two factors: the drive to reduce undercooling and surface energy during solidification, and the reduction in surface energy after solidification [95]. In some cases, both mechanisms can be modelled using coarsening kinetics that agree with Equation (3) [96], and typically the highest order dendrites with the smallest characteristic length scales experience coarsening [95,97]. This corresponds to the primary dendrite spacing in the case of the cellular structures observed in this work. For coarsening-controlled growth, the starting diameter of the cellular dendritic subgrains is assumed negligible in comparison to the final coarsened diameter, simplifying Equation (3) by setting d_0 to zero as was proposed by Martin et al. [98] and Kaneko [96]. A simple relationship now exists between the subgrain diameter and the coarsening time,

$$d = \sqrt[n]{k_T t} \qquad (4)$$

Experimental measurements of cooling time for each deposition are not easily made, requiring that a relationship be developed between the deposition splat thickness and cooling time. This relationship can be developed through an analysis of the heat diffusion equation, which can be simplified to one dimension, as heat can be assumed to transfer from the deposition to the substrate in the vertical axis. Equation (5) presents the one-dimensional form of the heat diffusion equation,

$$\frac{\partial T}{\partial t} = \frac{k}{c_p \rho}\left(\frac{\partial^2 T}{\partial x^2}\right) \qquad (5)$$

where T is the temperature, t is the time, k is the thermal conductivity of Inconel 718 (11.4 W m^{-1} K^{-1} [99]), c_p is the specific heat capacity of Inconel 718 (0.435 J g^{-1} K^{-1} [99]), ρ is the mass density of Inconel 718 (8.19 g cm^{-3} [99]), and x is distance in the vertical axis. Further assumptions can be made when modeling heat diffusion within this system; the size of the substrate allows it to act as an infinite heat sink while maintaining the starting room temperature and the argon atmosphere above the deposition has no ability to remove heat from the deposited material. This results in one Dirichlet boundary condition at the substrate and one Neumann boundary condition at the argon-deposition interface, as shown in Equation (6).

$$T = 298.15, \ \ \frac{\partial T}{\partial t} = 0 \qquad (6)$$

Additionally, the initial temperature is approximated as the solidus temperature for Inconel 718 (1533.15 kelvin [99]). These assumptions allow for the solution of the heat diffusion equation using the method of lines technique for partial differential equations. The spatial dimensions in Equation (5) are discretized using centered finite difference and the resulting ordinary differential equation (Equation (7)) is solved numerically using MATLAB's ode45 built-in function to find the temperature profile as the cooling process progresses.

$$\frac{\partial T}{\partial t} = \frac{k}{c_p \rho}\left(\frac{T_{i+1} - 2T_i + T_{i-1}}{(\Delta x)^2}\right) \qquad (7)$$

For a 10 and 20 µm thick deposition splat, the temperature profile throughout the material is shown as it progresses over time in Figure 13. As can be seen by the diverging temperature profiles, a longer period of time is required to cool depositions with larger thicknesses.

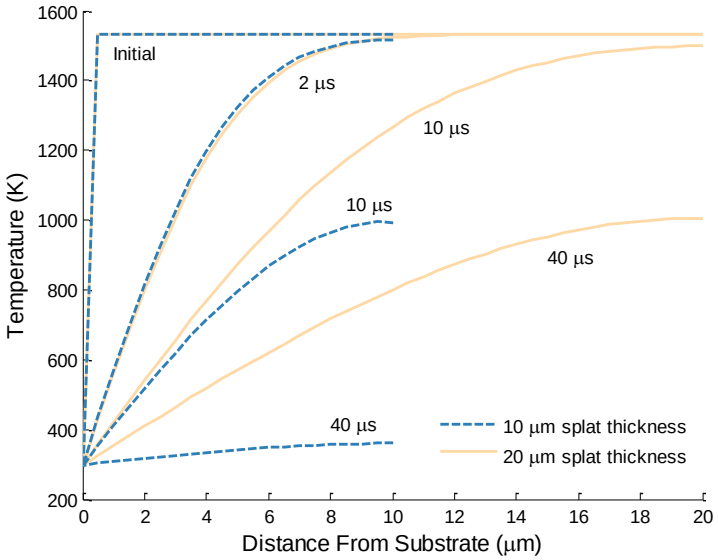

Figure 13. Temperature profile of 10 and 20 µm thick deposition splat during cooling process

To determine the effect of deposition thickness (L) on the time required to cool the deposition to the substrate temperature, the average temperature at each time step is calculated (Equation (8)) using MATLAB's trapz built-in function.

$$T_{avg} = \frac{1}{L}\int_0^L T\,\partial x \qquad (8)$$

The time required to reach an average deposition splat temperature within 1 kelvin of the substrate is calculated for depositions between 5 µm and 30 µm thick, with the results shown in Figure 14.

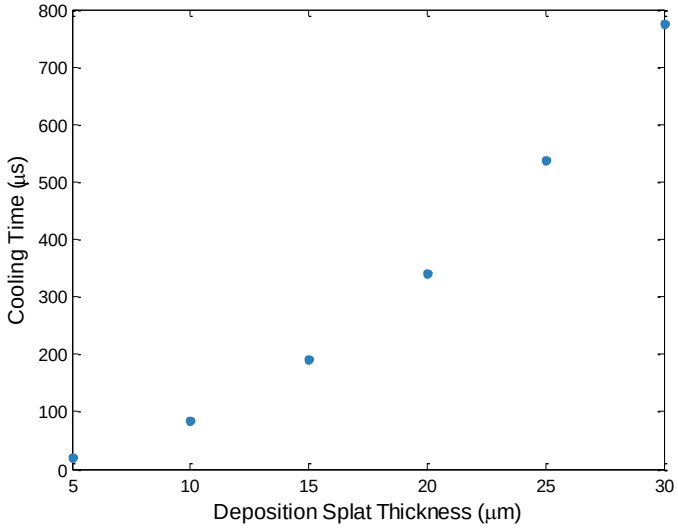

Figure 14. Time required to cool a deposition splat to an average temperature of 299.15 kelvin

An analysis of the solution shows a square dependence between the time required to reduce the temperature of a deposition and its thickness,

$$t = \beta x^2 \qquad (9)$$

related by a constant β. Varying the initial condition (temperature), substrate temperature or material dependent constants (k, c_p and ρ) result in changes to the value of β while maintaining the square relation between time and thickness. Substituting this relationship into Equation (4) results in,

$$d = Cx^{2/n} \qquad (10)$$

where C is equal to $\sqrt[n]{k_T \beta}$. The dependence of the final subgrain diameter on constants n and C (which includes both n and k_T) suggest a significant influence of the grain growth mechanism on the amount of coarsening experienced during the cooling of an ESD splat. Another influence on subgrain growth can be attributed to temperature and material properties such as density, specific heat capacity and thermal conductivity through the constant C, which is influenced by β.

Equation (10) provides a model by which to analyze experimental values. Experimental cellular dendritic subgrain diameters and the respective deposition splat thicknesses are displayed in Figure 6. The sample size used for the analysis consisted of 728 cellular dendritic subgrains – examples of which are shown in Figure 12 – and were measured using the intercept method described in the experimental methods section. Table 7 contains the best fit parameters for an exponential relationship, as well as the R^2 and normalized root-mean-square error values for the model.

Table 7. Fit parameters for subgrain size and deposition thickness relationship

	Fit Parameters		**Model Summary**	
Form	$\boldsymbol{C}$	$\boldsymbol{n}$	$\mathbf{R^2}$	**NRMSE**
Eq. 8	0.178	4.387	0.82	0.14

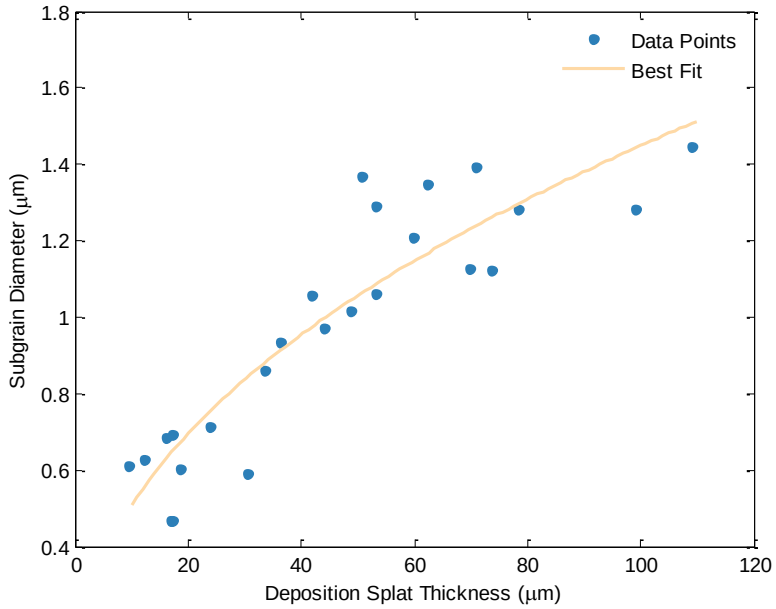

Figure 15. Average cellular dendritic subgrain size for various deposition splat thicknesses

For the current system, Equation (10) is able to relate the thickness of a deposition splat made by ESD to the diameter of the resulting cellular dendritic subgrains with relatively high accuracy, as shown with the R^2 value in Table 7. The process dependence of deposition splat thickness, in which higher energy parameters result in greater material transfer and thicker splats, indicates that a reduction in energy input during ESD results in splats with finer subgrain structures. The exponent n is found to vary from the ideally predicted value of 2, although it is still similar to previously reported experimental results for the subgrain growth equation [93]. Based on a derivation by Brook [94], a fit parameter n of approximately 4 suggests the presence of an impure system in which the grain growth mechanism occurs through the coalescence of a secondary (in this case interdendritic) phase by boundary diffusion. ESD processed materials have been shown by Ebrahimnia et al. [89] and Vishwakarma et al. [54] to exhibit segregation and secondary phases at the boundaries, which can be expected to coalesce during the subgrain coarsening process.

Contrary to the assumptions made in Equations (5) and (6), some heat loss is expected at the argon-deposition interface, and not all heat transfer occurs only in the x-axis. Additionally, the temperature profile in a deposited material is not uniform over time; a longer exposure to higher temperatures further from the substrate surface leads to some variations in subgrain coarsening within a deposition. Repeated heating and cooling from the deposition of new splats on top of previous splats may also influence the amount of coarsening. These non-idealities are likely to

introduce deviations from the model – particularly for thicker splats and those deposited in the first layer – which helps to explain the non-ideal R^2 value.

The relationship between deposition splat thickness and subgrain diameter can be extended to explain the mechanical properties of the deposited material. The Vickers hardness (HV) can be related to grain size using a relationship analogous to the Hall-Petch equation, previously applied by Hanamura et al. [100] to investigate the hardness of steels in relation to their grain size. This expression is shown in Equation (11),

$$HV = HV_0 + kd^{-1/2} \qquad (11)$$

where HV_0 and k are fitted constants and the Hall-Petch relationship is extended to subgrain diameter (d) as suggested by Rollett et al. [101]. Substitution of the relationship in Equation (10) between subgrain diameter and deposition splat thickness into Equation (11) results in a relationship between the Vickers hardness and the thickness of the deposition splat,

$$HV = HV_0 + kC^{-1/2}x^{-1/n} \qquad (12)$$

with the values of C and n previously listed in Table 7. HV_0 is analogous to the friction stress constant in a traditional Hall-Petch relationship, which is indicative of the lattice's intrinsic resistance to dislocation motion. The strengthening coefficient k is described by Russell and Lee [36] as the stress intensity required to induce plastic yielding across grain boundaries, which is expected to extend to subgrain boundaries as well. Hardness and splat thickness data obtained from ESD processed samples are shown in Figure 16, along with best fit parameters in Table 8 for the relationship in Equation (12).

Table 8. Fit parameters for deposition splat thickness and Vickers hardness

	Fit Parameters		**Model Summary**	
Form	$\boldsymbol{HV_0}$	$\boldsymbol{k}$	$\mathbf{R^2}$	**NRMSE**
Eq. 10	195.742	259.096	0.53	0.16

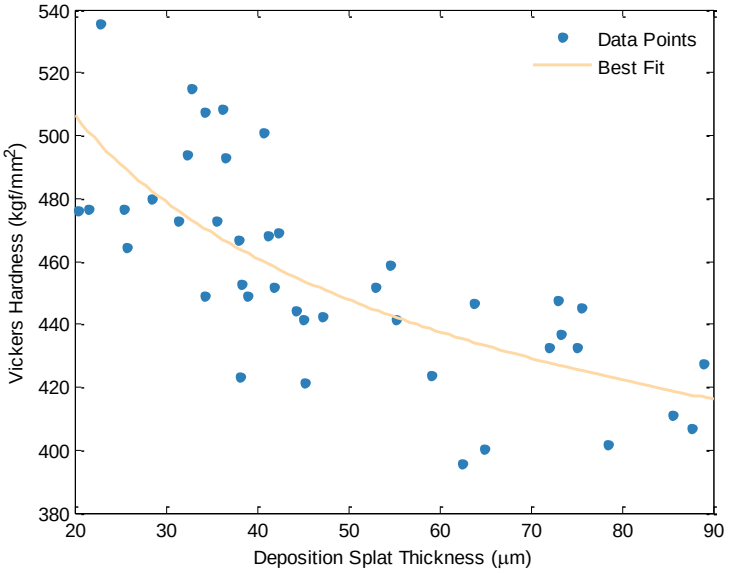

Figure 16. Vickers hardness for various deposition splat thicknesses

Due to the nature of microhardness measurements there exists significant variation in the gathered data, as shown by the lower R^2 value. EDX measurements show negligible differences in composition between areas measured at similar deposition splat thicknesses. Therefore, variation in the hardness values can likely be attributed to other material properties including variations in subgrain orientation, as suggested by the relevant testing standards (ASTM E384-16). Resistance to deformation can be dependent on cellular dendritic subgrain orientation, with some orientations providing greater or lower resistance than others. This effect is more prevalent when small indentation sizes are used, since dendritic subgrains in contact with the indenter may be uniformly oriented in high or low resistance orientations. However, the results still indicate the existence of a negative relationship between deposition hardness and splat thickness. As described by Russell and Lee [36], larger spacing between boundaries provides less barriers to dislocation movement and lower strength. This larger spacing is attributed to subgrain coarsening that occurs to a greater extent in thicker deposition splats, resulting in lower Vickers hardness. Through the models presented in Equation (10) and (12), it has been demonstrated that the deposition splat thickness influences the cellular dendritic subgrain size and deposited material properties. Improved performance of ESD processed materials is obtained with the use of lower energy input, which results in less material transfer, thinner deposition splats, finer subgrain features, and higher hardness.

3.4 Conclusion

The use of lower energy input during ESD to achieve thinner deposition splats results in improved coating quality, finer subgrain size and improved mechanical properties.

- Thinner deposition splats result in smaller diameter cellular dendritic subgrains. This is attributed to greater cooling rates and correspondingly lesser time for coarsening.
- Material within thinner deposition splats show higher microhardness as a result of the finer subgrain structure in accordance with a Hall-Petch relationship.

Chapter 4. Effect of boundaries on tensile properties

4.0 Preface

The following chapter is the second of three chapters that investigates the influence of the solidification microstructure on the properties of ESD processed Inconel 718. The point of interest in this study is the way in which failure occurs during tensile loading. Both splat boundaries and subgrain boundaries act as crack propagation pathways, allowing for a more brittle fracture with reduced ductility as seen in other literature studies. However, process parameters that result in thinner splats and smaller subgrains – both contributing to a greater number of boundaries – appears to show improved yield strength without any significant change in ultimate tensile strength. This result further supports the conclusion from the previous chapter, in which a finer subgrain microstructure increased the microhardness, while also identifying brittle phases at subgrain boundaries as a potentially addressable issue in ESD-processed Inconel 718.

This chapter is based on a published paper [102].

4.1 Introduction

The use of electrospark deposition (ESD) for the repair of damaged components has been proposed and investigated in literature [103,104]. Most applications focus on expensive components for which no other cost-effective or high-quality process exists. Oftentimes, the detrimental effects of heat affected zone formation, residual stresses and welding induced distortion limits the type of repair process that can be used. These effects can be mitigated through ESD repair techniques [83]. For this reason, aerospace and energy industries are good targets for the application of ESD, in which many high performance and high cost materials are subjected to extreme operating conditions. These applications include the repair of gas turbine engine blades suffering from issues such as chipped or damaged areas, and dimensional restoration of out-of-tolerance manufactured parts [83]. This avoids completely replacing or scrapping the affected components, providing an economic incentive for the implementation of an ESD repair process.

The ESD micro-welding process makes use of a consumable electrode deposited onto a conductive substrate through a series of short-duration electrical sparks. Material transfer results in splats that rapidly solidify and undergo metallurgical bonding with the substrate. The short pulse duration

often results in minimal heat affected zones [103], unlike other traditional welding processes. Previous studies conducted for the ESD repair of nickel-based superalloy materials have found favourable deposition properties with respect to the substrate material and other repair techniques. Wear and tensile test results of repaired Inconel 718 substrates show that wear rate, yield strength, and ultimate strength were similar to the base metal, although reductions in ductility were observed during tensile testing [83]. This was also observed for other nickel based alloys; a comparison of repair techniques for Waspaloy show that ESD is able to achieve a higher ultimate strength at the expense of a significant reduction in ductility [105].

Although mechanical properties have been reported previously, a study on the effect of microstructure on tensile properties in ESD repaired substrates is required to understand the failure mechanism of ESD repaired components. Analysis of crack propagation during tensile testing has the potential to improve ESD process parameter optimization for applications that require good mechanical properties. Interpretation of tensile testing data for ESD repaired specimens is performed, with a focus on the effect of microstructure on mechanical properties and crack propagation pathways. Results indicate that lower energy parameters result in higher yield strength, likely a result of increased splat boundaries and finer microstructure features. However, splat boundaries are found to serve as crack propagation pathways during fracture, which – along with the formation of brittle interdendritic phases – contribute to the lower recovery in ultimate strength.

4.2 Materials and methods

Double edge notched tensile testing specimens were made from a 3.3 mm thick Inconel 718 solution-annealed sheet. The supplier provided composition is listed in Table 9, and the specimen dimensions with and without a cavity are shown in Figure 17.

Table 9. Inconel 718 substrate composition (wt%)

Ni	**Fe**	**Cr**	**Nb**	**Mo**	**Ti**	**Co**	**Al**	**C**	**Mn**	**Si**	**Cu**
53.5	17.8	18.5	5.1	2.9	0.9	0.2	0.6	0.03	0.09	0.08	0.13

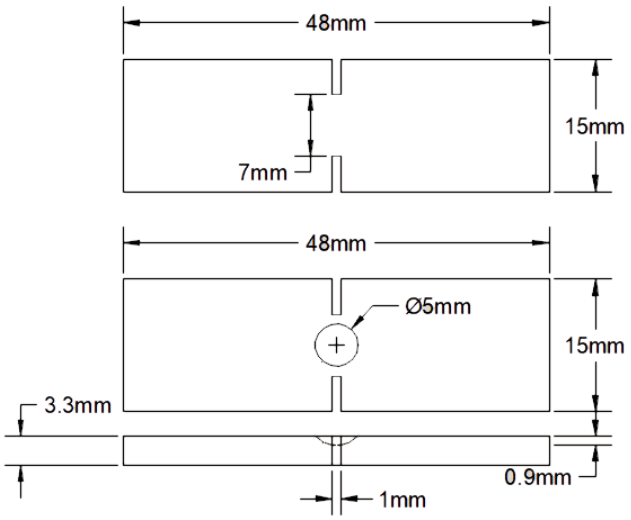

Figure 17. Schematic of tensile testing specimens with and without a cavity

Cavities with ideal dimensions of 5 mm in diameter and 0.9 mm deep (seen in Figure 17) were machined with the use of a ball nose end mill. Cavities were then repaired with a Huys Industries ESD machine using a 3.2 mm diameter Inconel 718 electrode. Local shielding was provided by ultra-pure Argon gas at a flow rate of 10 L/min. A hand-held motorized peening tool is used throughout the deposition to reduce surface roughness, and an aluminum oxide grinding stone is used to perform dimensional restoration of the filled cavities.

The ESD parameters used for the cavity repair are listed in Table 10, with the input energy per pulse (E_i) calculated using the standard formula for energy stored in a capacitor,

$$E_i = \frac{1}{2} C V^2 \qquad (13)$$

where C is the capacitance and V is the voltage.

Table 10. ESD parameters for cavity repair

	Energy Input	
Parameters	**Low**	**Medium**
Voltage (V)	50	100
Capacitance (µF)	80	80
Frequency (Hz)	170	170
Input Energy (mJ)	100	400

Three types of tensile testing specimens are created and tested: base metal specimens have no cavities, empty cavity specimens contain cavities which have not been repaired, and repaired specimens consists of cavities which have been filled with Inconel 718 via ESD. These specimens are tested to failure on an Instron model 4206 at a constant extension speed of 1 mm/min. A total of 3 base metal specimens, 3 low energy repaired specimens and 6 medium energy repaired specimens are tested. Of the 6 medium repaired specimens, 4 are tested to failure and 2 are tested until a crack begins to form. Yield strength values - but not ultimate strength - are obtained from the incomplete tests, and independent t-tests with two-tailed hypothesis are performed to evaluate differences in the mean values between low energy, medium energy and base metal specimens. A 90% confidence level is used to identify significance ($p<0.1$) and the effect size is evaluated with the use of a corrected Hedges' g value for small sample sizes [106], where $g=0.8$ is considered a large effect and $g=1.3$ is considered a very large effect [107,108].

Fractured samples are imaged with a JEOL JSM-6460 scanning electron microscope (SEM) and cross sections of the fracture surface are imaged with an Oxford BX51M optical microscope (OM). Microhardness measurements are performed with the use of a Wolpert Wilson 402 MVD micro Vickers hardness tester. Cross sectioned surfaces are polished and then etched with inverted glyceregia ($HCl:HNO_3$:Glycerol in a 5:1:1 ratio) for 1.5 to 2.5 minutes.

4.3 Results

4.3.1 ESD Microstructure

Initial observations of ESD repaired Inconel 718 cavities prior to tensile testing reveal the build-up mechanism of the repair process. Upon cross sectioning and etching with inverted glyceregia, the individual splats from the ESD repair are visible. Figure 18b shows various sized splats which stack together to form the deposited material that comprises the repaired cavity in Figure 18a.

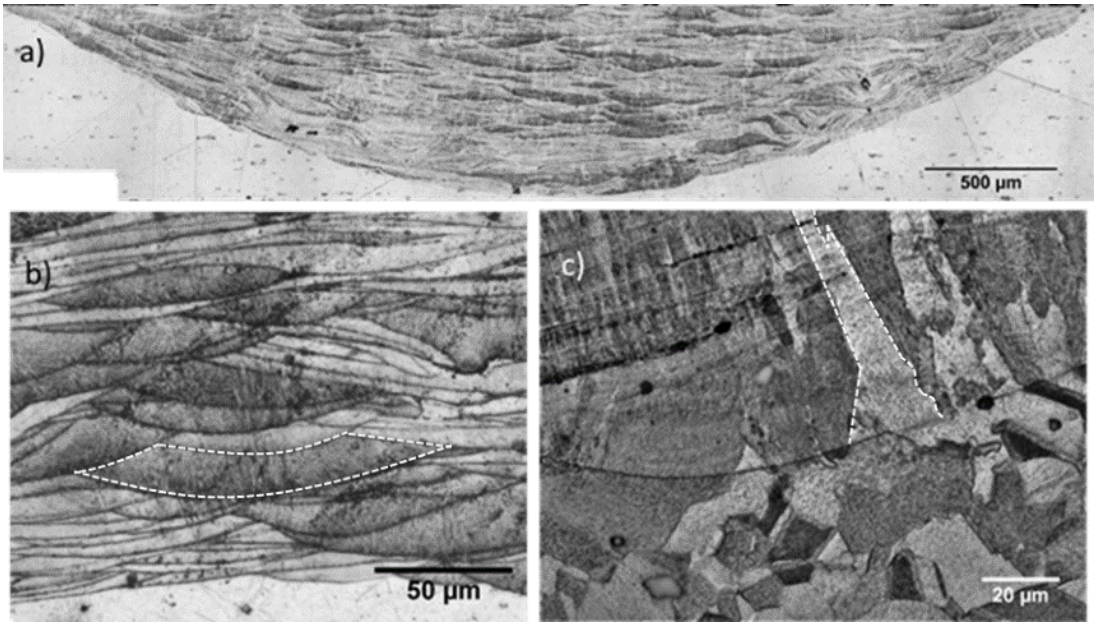

Figure 18. Cross sectional OM image after etching of a) a repaired cavity, b) the deposition splats within a repaired cavity (one splat highlighted with dashed lines) and c) epitaxial grain growth (one epitaxial grain highlighted with dashed lines) in deposited material influenced by the substrate base metal grain

The layered microstructure resembles that of other ESD processed materials and has been documented in depth in literature studies [103]. The deposition parameters listed in Table 10 were chosen to minimize the defects commonly observed within ESD, including voids, cracks and delamination. An average density of 99.35% was determined from OM images of cross-sectioned cavities, with no significant difference between medium and low energy ESD parameters. Longer etching times reveal epitaxial grains within the deposited material, some of which traverse splat boundaries in the direction of material buildup, as shown in Figure 18c. The volume of the deposited splat is related to the input energy per pulse, with larger quantities of deposited material resulting in thicker deposition splats [109]. It is expected that the average splat thickness of a deposition performed with medium energy input is larger than that of a low energy input deposition, such that fewer splat layers are required to fill a cavity. Measurements of 140 splat thicknesses showed that medium energy deposition splat thickness (11.2 µm with a standard error of ±2.0 µm and a maximum measured splat thickness of 95.3 µm) was larger than that of low energy depositions (7.1 µm with a standard error of ±0.6 µm and a maximum measured splat thickness of 33.4 µm). This corresponds with the time required for the repair of a cavity; medium

energy ESD parameters required 18 minutes while low energy parameters required 64 minutes on average.

The cellular dendritic subgrain structure and interdendritic phases of ESD processed Inconel 718 have been previously reported in literature [54], resembling that of other rapid solidification processes [110]. The effect of splat size on microstructure features can be seen in Figure 19, with larger cellular dendritic subgrains in the thicker splat. Interdendritic regions appear lighter in the SEM due to edge effects from faster etching of the γ phase and slower etching of Nb-rich boundaries with interdendritic secondary (Laves and carbide) phases [110]. This interdendritic region was previously reported to be 50 nm in width [111]. However, the width of interdendritic phase segregation in ESD appears to be influenced by splat size in a similar way as the subgrain width.

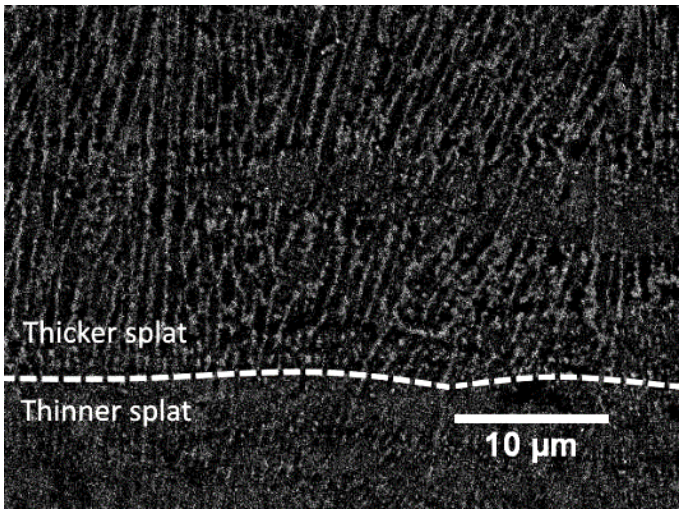

Figure 19. SEM image of subgrain microstructure in ESD processed Inconel 718 after etching

4.3.2 Mechanical Properties

Repaired tensile specimens are tested to failure and the mechanical properties are compared to base metal specimens and empty cavity specimens. Average results from these tests are shown in Table 11, with representative tensile test curves shown in Figure 20b. The standard formula for stress (σ) is seen in Equation (14),

$$\sigma = \frac{F}{A} \qquad (14)$$

where F is the applied force and A is the cross-sectional area of the specimen. For the calculation of stresses in Table 11, the original cross-sectional area (A_0) was used, which assumes no cavity was made. As a result, the empty cavity specimens decrease in strength when compared to base metal specimens by an amount equivalent to the reduction in cross-sectional area at the specimen's fracture plane. The recovery in yield and ultimate strength of repaired specimens when compared to empty cavity specimens can be attributed to the ESD material. The yield and ultimate strengths obtained by Carofalo et al. [105] for ESD repaired specimens were approximately -2% and -9% respectively when compared to base metal specimens, which closely compares to results obtained in this study (shown in Table 11).

Table 11. Tensile test results and relative performance (RP) compared to base metal specimens

Specimen Type	**Yield Strength**		**Ultimate Strength**	
	MPa	**RP**	**MPa**	**RP**
Base Metal	605		853	
Empty Cavity	508	-16%	743	-13%
Repaired (Med)	586	-3%	777	-9%
Repaired (Low)	632	+5%	791	-7%

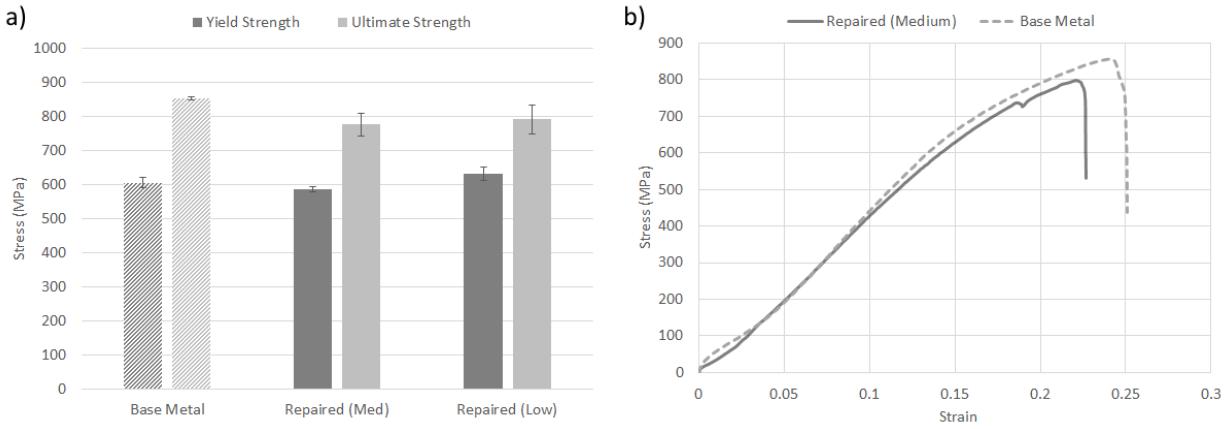

Figure 20. a) Yield and ultimate strengths with standard error and b) example stress-strain curves

No significant difference exists between the yield strength of base metal specimens and low energy repaired (p=0.334) or medium energy repaired (p=0.275) specimens. However, repairs performed using low energy input achieved higher yield strengths than those with medium energy input

(p=0.066) and displayed a very large effect size (g=1.31). Unlike the recovery in yield strength, the difference in ultimate strength between base metal and repaired specimens remains statistically significant (p=0.030) and displays a large effect size (g=1.14). Figure 20b shows the stress-strain curve of an ESD repaired tensile specimen using medium energy input, which exhibits a lower ultimate strength than the base metal and the presence of a pre-failure (deposition) fracture.

The first fracture nearer the yield point suggests that a less ductile fracture occurs in the ESD material, followed by greater plastic deformation of the base metal and subsequent ductile fracture. The pre-failure fracture leads to a change in the effective cross-sectional area of the specimen as it undergoes tensile testing. When incorporating the reduction in area due to the presence of an unfilled cavity in empty cavity specimens and the reduction in area due to the deposition fracture in repaired specimens, an adjusted ultimate strength (AUS) for the substrate base metal can be determined. The results presented in Table 12 demonstrate that the fracture of the base metal occurs at similar stresses in all specimen types. This suggests that the ESD repair process did not form a noticeably detrimental heat-affected zone in the base metal, and that the pre-failure fracture of the deposition during tensile testing does not propagate into or weaken the base metal substrate.

Table 12. Adjusted ultimate strength (AUS) of tensile specimen substrate

Specimen Type	**AUS (MPa)**
Base Metal	853
Empty Cavity	858
Repaired (Med)	857
Repaired (Low)	862

4.3.3 Fractographic Analysis

The base metal and deposition fracture surfaces were found to exhibit different morphologies. SEM images shown in Figure 21a and Figure 21b display the presence of a dimpled morphology on the base metal fracture surface and step-like facets with smoother surfaces in the deposited material. Cross sectional images of the base metal near the fracture interface (Figure 22a) show elongation of the grains in the direction of the applied tensile force, consistent with a ductile fracture.

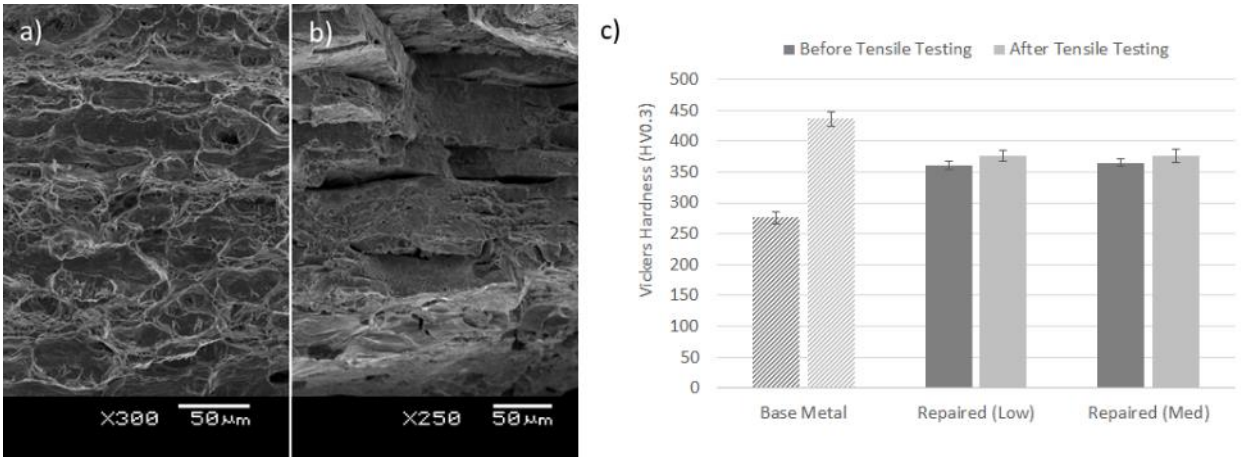

Figure 21. SEM image of a) base metal fracture surface, b) deposition fracture surface with step facets, and c) microhardness measurements and standard error of base metal and deposition in repaired specimens within 300 µm of the fracture interface before and after tensile testing

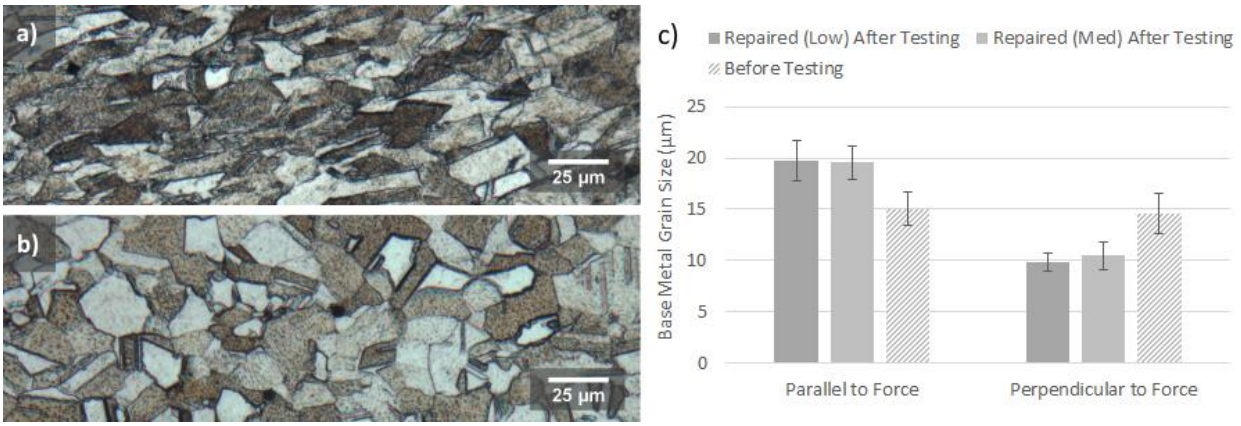

Figure 22. Grain structure of Inconel 718 base metal a) within 300 µm of the fracture interface, b) as received prior to testing and c) the grain size and standard deviation in the base metal before and after tensile testing within 300 µm of the fracture interface

Measurement of the grain size for the base metal of repaired specimens show an average 30% elongation along the direction of the applied tensile stress as well as a 31% reduction in grain size along the direction perpendicular to the applied stress (Figure 22c). Microhardness measurements show a significant increase in Vickers hardness (from 276 HV to 436 HV as shown in Figure 21c) for the base metal along the fracture interface after tensile testing. This strain hardening behaviour arises due to a pileup of dislocations in the crystal lattice, which occurs during plastic deformation [112]. Unlike the base metal, the ESD material does not exhibit a significant increase in

microhardness, again suggesting that the deposited material does not undergo significant plastic deformation and experiences a more brittle fracture. Microhardness measurements were also performed parallel to the buildup direction on the top surface of medium energy ESD repaired cavities and were compared to results obtained for the perpendicular direction given in Figure 21c. Hardness in the parallel direction (381.0 HV with a standard error of ±7.2 HV) was higher than that of the perpendicular direction (365.5 HV with a standard error of ±5.6 HV) by 4.2%, indicating the presence of a small hardness anisotropy.

4.4 Discussion

4.4.1 Effect of Microstructure on Crack Propagation and Fracture Toughness

Figure 23 shows the crack initiation location at the surface of the ESD Inconel 718, which then proceeds to propagate towards the center of the specimen.

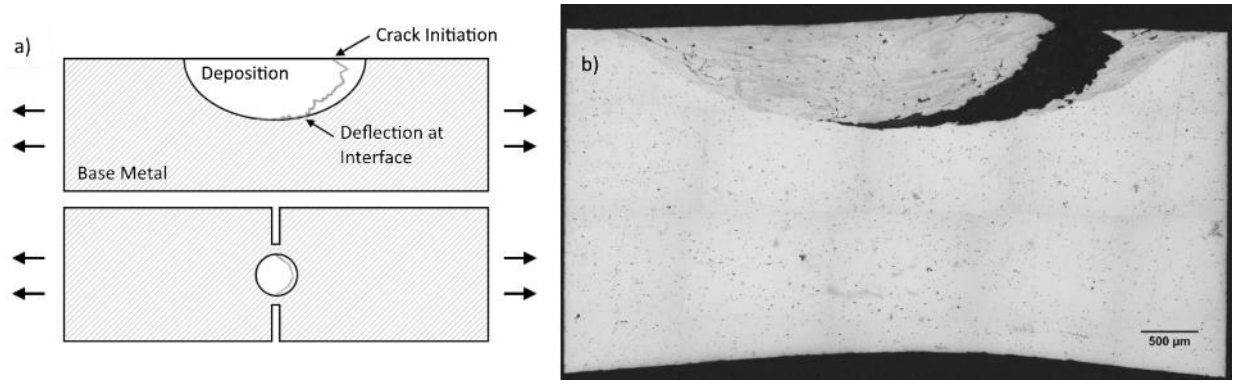

Figure 23. a) Side and top view schematic of crack location relative to deposition geometry and b) cross-sectional OM image of a lightly etched specimen tested until the initial fracture of the deposited material

Cracks initiating in the weld metal, in this case likely due to the presence of brittle secondary phases [113], tend to propagate in the direction of greatest plastic strain concentration [114]. The highest plastic strain concentration – as measured by grain elongation and hardness changes during tensile testing (Figure 21 and Figure 22) – is located in the base metal on the plane through the center of the repaired cavity, where the specimen's cross-sectional area is the smallest. This can be seen in Figure 23b, where the bottom of the specimen exhibits necking as a result of plastic deformation. As was confirmed by the calculation of an adjusted ultimate strength in Table 12, the pre-failure crack within the deposition does not propagate into or otherwise affect the base metal

substrate of repaired specimens. Work published in literature attributes this result to a greater fracture toughness in the lower strength material [114].

When fracture of the deposited material occurs, propagation of the crack is redirected by splat boundaries. A cross-sectional image of the fracture surface (Figure 24) shows the step-like facets caused by two primary directions of crack propagation.

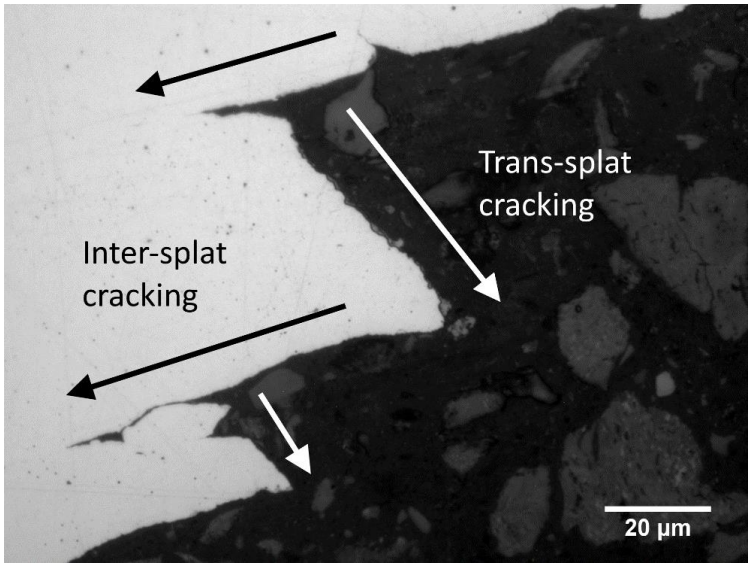

Figure 24. OM image of inter-splat and trans-splat cracking along fracture surface cross-section

Previously, Figure 21b displayed the fracture surface of the deposited material with the formation of step-like facets. Several secondary cracks can be seen along the splat boundaries on the step facets, visible in Figure 21b and more clearly seen in Figure 24 along the inter-splat cracking direction. The presence of step facets and secondary cracks suggest that crack propagation occurring along a splat boundary (inter-splat) is met with varying resistance (fracture toughness), occasionally encouraging crack propagation though the splat (trans-splat). This mixed cracking mechanism results in step facet formation similar to previously reported metals with lamellar structures [115]. Evidence of secondary inter-splat cracking is only found branching from the fracture surface as seen in Figure 24, with the rest of the deposition free from these cracks.

The occurrence of crack propagation at two primary angles to the applied tensile stress, corresponding with cracking in the inter-splat direction and in the trans-splat direction, suggest differences in the fracture toughness between the interfaces and splats of ESD materials. The relative resistance to crack propagation can be determined by considering the relative energy

dissipated during fracture for each crack propagation angle. Considering that both trans-splat and inter-splat cracks propagate at angles other than 90° from the applied stress, mixed mode effects must be considered. The applied stress (σ_0) can be broken down into Mode I (σ_I) and Mode II (σ_{II}) components, as shown in Figure 25 and by Equations (15) and (16). Mode I corresponds to stress acting perpendicular to the crack face, while Mode II refers to an in-plane shear perpendicular to Mode I in the direction of crack propagation.

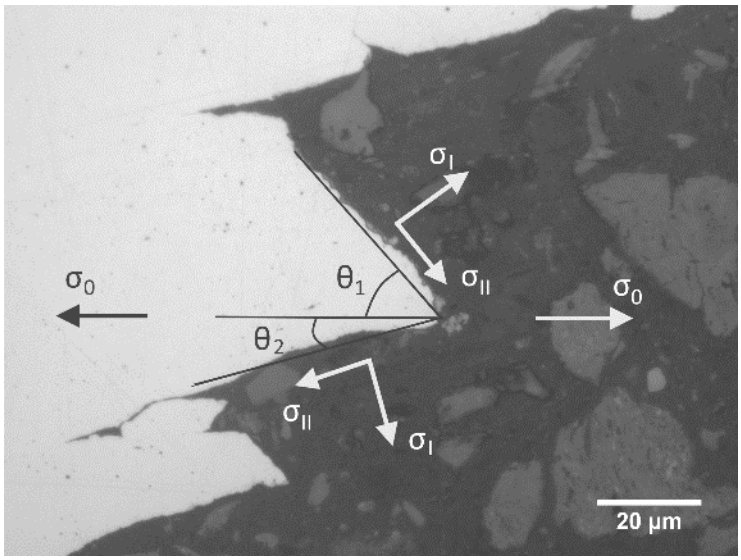

Figure 25. Examples of σ_I, σ_{II}, and θ for trans-splat (θ_1) and inter-splat (θ_2) cracks

$$\sigma_I = \sigma_0 \sin^2(\theta) \qquad (15)$$

$$\sigma_{II} = \sigma_0 \sin(\theta)\cos(\theta) \qquad (16)$$

Stress intensity factors (SIF) are used to describe the stress state at the crack tip caused by the Mode I and Mode II stresses. When the stress intensity factor at the tip of a crack reaches a critical value, fracture occurs as the crack propagates through the material. The stress intensity factor caused by Mode I loading (K_I) and Mode II loading (K_{II}) can be determined from the individual Mode I and Mode II stress components as shown in Equations (17) and (18),

$$K_I = f\sigma_I\sqrt{\pi a} \qquad (17)$$

$$K_{II} = f\sigma_{II}\sqrt{\pi a} \qquad (18)$$

where a is the crack length for an edge crack and f is a geometry dependent factor equal in this case to 1.122 [116]. Stress intensity factors can be used to determine the energy release rate (G),

with the critical value of G required for crack propagation known as the fracture toughness [117]. In order for a crack to propagate through a material, energy release must equal or exceed that required to form new surfaces at the tip of the crack. Therefore, the higher the energy release rate required for crack propagation, the higher the fracture toughness of the material. Equation (19) relates the energy release rate to the Mode I and Mode II stress intensity factors,

$$G = \frac{1 - v^2}{E}[K_I^2 + K_{II}^2] \qquad (19)$$

where v is Poisson's ratio and E is Young's Modulus. The model presented here is based on linear elastic theory, which assumes the material is linear elastic and isotropic in the direction of crack propagation. Much work has been done to understand crack kinking away from interfaces and crack deflection at interfaces [118]. In either case, the relative value of the energy release rates for a crack propagating through a splat (G_{splat}) or along an interface (G_{int}) can be used to assess which of the two scenarios is most likely. The ratio is as defined in Equation (20) for an interface within a homogeneous material (the same Young's modulus and Poisson's ratio on either side of the interface).

$$\frac{G_{int}}{G_{splat}} = \frac{K_{I\,int}^2 + K_{II\,int}^2}{K_{I\,splat}^2 + K_{II\,splat}^2} \qquad (20)$$

Calculations of the energy release rate (G) at various angles is performed using Equation (20) and the result is shown in Figure 26. As expected, energy release rate increases for higher propagation angles with primary Mode I loading, and decreases at lower angles where Mode II loading has a higher influence. A comparison of energy release rates between the two angles of propagation in ESD Inconel 718 (average of 45° for trans-splat and 23° for inter-splat) show a 0.291 G_{int}/G_{bulk} ratio. This suggests that splat boundaries of ESD Inconel 718 have a critical energy release rate (fracture toughness) approximately 30% that of the splat material inside the boundaries.

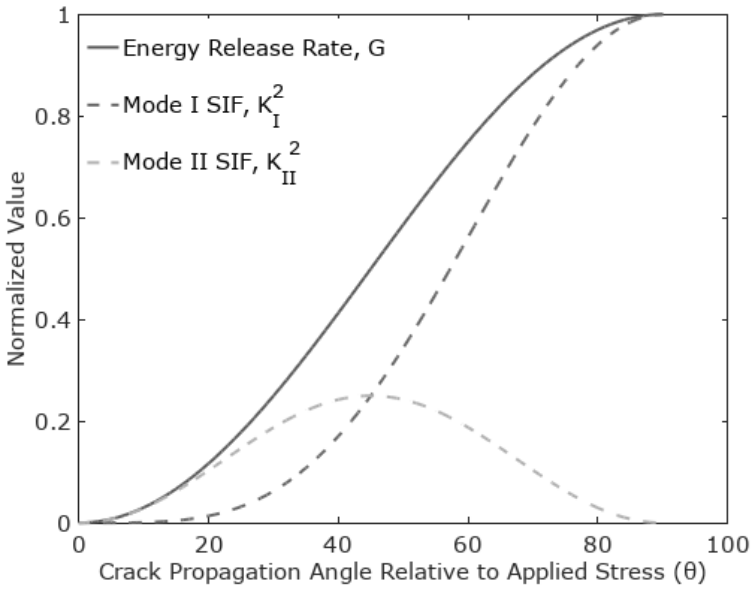

Figure 26. Energy release rate dependence on crack propagation angle and contributing stress intensity factors

In the case that a crack is propagating towards an interface, the inequality in Equation (21) must hold for the crack to deflect along the interface. An interface fracture toughness less than 0.291 times the fracture toughness of the bulk material will cause deflection. However, an interface fracture toughness greater than 0.291 times the splat fracture toughness will result in penetration across the interface. This inequality can also be used to describe the reverse scenario, in which a crack propagating along an interface may kink into the splat. The inequality in Equation (21) would hold for a crack that continues to propagate along the interface, whereas the reverse inequality describes the situation in which a crack propagating along an interface kinks into the splat material.

$$G_{int} < 0.291 G_{splat} \qquad (21)$$

4.4.2 Effect of Microstructure on Tensile Properties

Several microstructure features associated with ESD can be used to explain the performance of repaired cavities under tensile stress. Low energy ESD parameters result in more splat boundaries, which were found to be more readily revealed during etching than grain boundaries (1.5 minutes vs. 2.5 minutes of etching required, respectively). More reactive boundary atoms are dissolved by etchants at a faster rate than those within the boundaries, with the etching rate affected by the concentration of dislocation induced lattice distortions or impurity atoms [119,120]. Additionally,

thinner splats were shown to have higher microhardness due to finer subgrain features as shown in the previous chapter. With an increase in the number of boundaries acting as obstacles to dislocation movement known to have a positive effect on yield strength [119], an increase in the number of subgrain and splat boundaries can contribute to the observed increase in yield strength for low energy ESD repaired specimens.

Although boundaries have the positive effect of improving the yield strength of repaired specimens, the dislocation density and concentration of impurities at the boundary is expected to vary. As was shown previously in Figure 18c, some grains extend across splat boundaries, suggesting a lower dislocation density at these locations. This reduction in defects is expected to increase the fracture toughness and induce a change in crack propagation from the inter-splat direction to the trans-splat direction. In addition to variations in fracture toughness along splat boundaries, the material within a splat is also expected to vary in its fracture toughness. Thicker deposition splats result in coarser subgrain structures and coarser interdendritic regions, similar to higher energy input in other solidification processes [121]. Interdendritic regions with Laves phase precipitation are expected to be detrimental to the ultimate strength and fracture toughness of the ESD Inconel 718, however are not expected to detrimentally affect the yield strength in the as-deposited condition. Literature has shown the quantity of Laves phase in pre-precipitation hardened Inconel 718 to have no effect on the room temperature yield strength while negatively impacting the ultimate strength and ductility [122]. Laves phases are reported to have lower fracture toughness than the surrounding matrix, while preventing the formation of strengthening γ'' phases during precipitation hardening by removal of alloying elements from the nickel matrix [121–123]. Therefore, the thickness of a deposited splat is indirectly expected to vary the trans-splat fracture toughness and mechanical properties such as ultimate strength and ductility.

Variations in fracture toughness and mechanical properties at splat boundaries (attributed to dislocation density) and in the splat (attributed to subgrain microstructure size and Laves phase formation), are expected to account for the mixed inter-splat and trans-splat crack propagation mechanism. A trade-off exists as a result of the unique splat microstructure of ESD materials. An increase in the number of splat boundaries and higher microhardness from smaller subgrain sizes in thinner splats is identified as the reason for the yield strength increase in lower energy ESD repaired cavities, a beneficial property for repair applications due to the tendency to operate within

the elastic region of a material. However, splat boundaries exhibit a fracture toughness of approximately 30% of the material within the splat bulk. This microstructure influenced crack propagation pathway, along with the presence of a brittle Laves phase, is expected to contribute to earlier fracture when compared to an Inconel 718 material of equivalent hardness with no splat interfaces or Laves phases. Lower energy ESD can be expected to have more splat boundaries – making inter-splat fracture more likely – while also increasing the fracture toughness of trans-splat cracking due to less Laves phase formation. This trade-off likely explains the lack of statistically significant difference in ultimate strength ($p=0.805$) between the low energy and medium energy ESD process parameters used to repair specimen cavities.

4.5 Conclusion

Mechanical properties of repaired Inconel 718 specimens were found to be dependent on microstructure, which is a result of the ESD process parameters used. The effect of ESD microstructure on yield strength and fracture toughness can be summarized as follows:

1. ESD splat boundaries and subgrain microstructure size are correlated to yield strength recovery. Cavities repaired with low energy ESD parameters are known to result in thinner splats, leading to an increased number of splat boundaries and finer subgrain microstructures. The splat boundaries are expected to act as barriers to dislocation movement which – in combination with the higher strength of finer subgrains – contributes to the observed increase in yield strength.
2. The observed combination of trans-splat and inter-splat cracking directions, in which cracks propagate through splats and along splat boundaries, suggest that fracture toughness is not constant along the boundaries or in the splats. ESD splat boundaries have lower fracture toughness than material within the splat. Crack propagation angles obtained from fractured surfaces indicate that the fracture toughness of splat boundaries is approximately 30% that of the subgrain boundaries within the splat material. Higher dislocation densities and impurities at splat boundaries are expected to contribute to the lower fracture toughness.

Chapter 5. Effect of micro-segregation on phase transformations

5.0 Preface

This is the last of three chapters that focuses on the effect of solidification microstructure on the properties of ESD processed Inconel 718. The micro-segregation and brittle phases that form at subgrain boundaries during solidification are shown to not only affect mechanical properties as was discussed in the previous chapter, but to also affect phase transformations that occur at elevated temperatures. This is relevant to the development of appropriate heat treatment processes and for determining the response of ESD-processed Inconel 718 when exposed to transient overheating events. The Nb segregation at subgrain boundaries encourages the formation of the δ phase when exposed to temperatures from 700-900 °C, which influences the crack propagation mode while also indirectly reducing the strength of the alloy by decreasing the amount of γ".

This chapter is based on a published paper [124].

5.1 Introduction

Rapid solidification processing of metal alloys has been widely used for the application of coatings, the repair and joining of components, and the additive manufacturing of entire parts. Laser, electron beam, arc, and electrospark techniques can fall under this classification, which are based on molten droplet transfer or self-quenching mechanisms [125]. The high cooling rates achieved by these mechanisms – through a combination of high temperature gradient and/or high solidification front velocity [48] –is expected to reduce but not eliminate micro-segregation of alloying elements [125]. Micro-segregation arises during solidification due to the solid phase's rejection of less soluble and slower diffusing elements into the liquid phase. At the terminus of solidification, the final liquid cools to form a eutectic or phases enriched in these elements. This compositional variation between the core subgrains and subgrain boundary regions of an alloy can influence mechanical properties, microstructure evolution, and phase transformations during subsequent processing or use.

In some rapid solidification processed Ni-superalloys such as alloy 625 and alloy 718, the subgrain boundaries contain a Nb-rich eutectic and Nb-rich Laves phase. This Laves phase is reported as detrimental to some mechanical properties, with low fracture toughness that facilitates crack

propagation [102], reduces creep lifetime [126], and reduces fatigue life at high stress amplitudes [45,127]. Although solution annealing heat treatments can be applied to homogenize the microstructure and redistribute micro-segregated elements, these alloys are frequently used in a direct aged condition where a strengthening phase is precipitated without first homogenizing the microstructure. Comparatively few studies have focused on the microstructure evolution and phase transformations resulting from compositional variation when these non-homogenized materials are exposed to elevated operating temperatures. Lass et al. have observed the growth of the δ phase (Ni_3Nb) along subgrain boundaries in laser powder bed fusion additive manufactured alloy 625 during the industry-recommended post-process heat treatment [128]. Similar observations were presented by Qi et al. [129] and Zhang et al. [130] for alloy 718, with a more in-depth study on the formation of the δ phase performed by Lyu et al. [131], who found that the precipitation rate of the δ phase in a rapid solidification processed (RSP) alloy 718 could be influenced by encouraging a more homogenized initial microstructure. These results can be attributed to partial dissolution of the Laves phase, which increases the amount of available Nb, and the low diffusion of Nb, which results in Nb-rich subgrain boundaries that encourage nucleation of the δ phase at elevated temperatures. A useful application of this phenomenon was presented by Liu et al. [132], which made use of the Laves to δ phase transformation to then homogenize alloy 718 with a lower temperature heat treatment. More recently, Huang et al. [133] constructed time-temperature-transformation diagrams for the various phases in laser additive manufactured alloy 718, finding notable differences when compared to the wrought material.

Exposure of alloys to elevated temperatures occurs frequently during standard heat treatments, transient overheating events during use [134,135], or even during the reheating of previous layers that occur in additive manufacturing processes [136], indicating that an improved understanding of the microstructural evolution is warranted. The methodology used here quantifies the effect of micro-segregation during rapid solidification processes on δ phase formation at elevated temperatures in Nb-rich Ni-superalloys, which can similarly be used to predict the size of secondary phases in other micro-segregated alloys after heat-treatment. As demonstrated in this study, the exposure of RSP alloy 718 to elevated temperatures results in the formation of δ precipitates at subgrain boundaries, whereas homogenized alloy 718 forms δ precipitates primarily along grain boundaries. An observed decrease in δ precipitate size and increase in the number of precipitates in RSP alloy 718 is well explained with the use of a nucleation site model, providing

support for previous assumptions that the presence of Nb at subgrain boundaries is what encourages nucleation of the δ phase at those locations. An analysis of the δ phase coarsening kinetics suggest that the rate of Laves phase dissolution is not the limiting factor. Instead, the diffusion of Nb within the matrix is found to be the limiting factor for δ phase coarsening in a rapid solidification processed Nb-rich Ni-superalloy.

5.2 Material and Methods

Rapid solidification processing is performed using electrospark deposition, which operates by discharging a capacitor to form a short duration spark that transfers material from an electrode (anode) to a substrate (cathode). Small droplets of electrode material (< 1 nL) splash onto the substrate surface and rapidly solidify. The small volume of transferred material, comparatively large substrate size which acts as a heat sink, and a typical 95 % cooling time between subsequent capacitor discharges result in an overall low heat input and very fast cooling rates up to 10^9 °C/s at the terminus of solidification [20]. Electrospark deposition was performed using a Huys Industries manual ESD machine at 90 V, 120 μF, and 170 Hz, with four passes performed in a raster scan pattern. A 5.0 grade ultra high purity argon shielding gas was delivered coaxially during deposition at a flow rate of 10 L/min.

For this study, an as-received alloy 718 substrate in the solution annealed condition (in accordance with SAE AMS5596 and ASTM B670 specifications) was coated with an alloy 718 electrode (3 mm diameter) using electrospark deposition. The composition of both materials is listed in Table 13. Each sample therefore contains both rapid solidification processed (RSP) alloy 718 and solution annealed (SA) alloy 718. This configuration allows for both material conditions to be heat treated and evaluated simultaneously. Since electrospark deposition results in a heat affected zone size of up to 80 μm for this material combination [137], care was taken to evaluate the substrate sufficiently far from the coating.

Table 13. EDX composition (wt%) of alloy 718 used as the electrode and substrate

Alloy 718	**Ni**	**Cr**	**Fe**	**Nb**	**Mo**	**Ti**	**Al**
Electrode	49.6	18.1	17.2	5.8	5.1	1.5	0.9
Substrate	50.1	17.2	17.4	5.9	4.1	1.4	1.0

The RSP alloy 718 and SA alloy 718 were aged with a two-step process to obtain a precipitation hardened state in which alloy 718 is more commonly used. The temperature was ramped to 720 °C at 5 °C/min in an argon environment and held for 8 hours, after which the samples were furnace cooled to 620 °C and held for 10 hours. At the conclusion of the holding period, the samples were removed from the furnace and allowed to air cool. These two material conditions, rapid solidification processed and aged (RSP + aged) and solution annealed and aged (SA + aged) are then subjected to elevated temperatures of 700 °C, 800 °C, and 900 °C for various durations to determine the effect of micro-segregation on phase transformations. These heat treatments were performed in an air environment to simulate typical usage.

Sample cross-sections were etched with inverted glyceregia composed of HCl:HNO3:Glycerol in a 5:1:1 ratio for up to 2 minutes depending on the extent of heat treatment, and images of the microstructure were obtained using a Zeiss UltraPlus scanning electron microscope (SEM) with an energy-dispersive X-ray spectroscopy (EDX) attachment. Measurements of the δ phase long axis were made using ImageJ software, and MATLAB was used to obtain best fit curves for the experimental data. A JEOL7000F SEM with an Oxford electron backscatter diffraction (EBSD) detector was used for determination of grain boundary misorientation, and a MicroLab 350 Auger Microprobe is used for obtaining the composition of small phases using Auger electron spectroscopy (AES). Tensile testing was performed on an Instron 5548 micro tensile tester at 1 mm/min, using non-standard tensile specimens as shown in Figure 27. The small specimen sizes were designed to accommodate the small deposition volumes and long deposition times associated with high-quality ESD repairs. ESD process parameters were kept the same as those used for the microstructure analysis, and the specimens were created using a double U-joint repair in which one cavity was created and repaired at a time. The two notches were created using a Struers Accutom-50 precision saw and water cooling, to avoid microstructural changes from heat input during cutting. Microhardness measurements were performed on a Wolpert Wilson 402 MVD micro Vickers hardness tester using 100 gf and a 15 s dwell time.

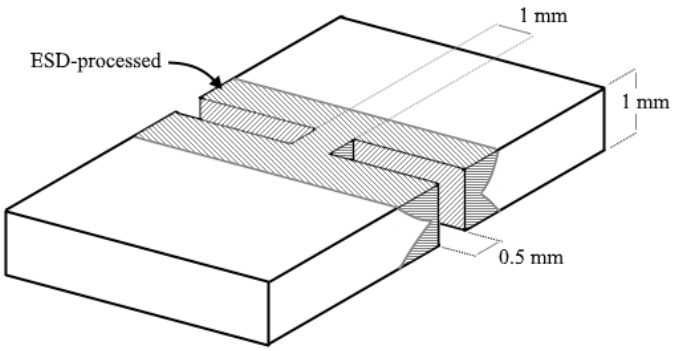

Figure 27. Specimen used for tensile testing with ESD repaired U-grooves

5.3 Results and Discussion

5.3.1 Microstructure Evolution

The rapid solidification processed (RSP) alloy 718 is primarily composed of low angle (2°) boundaries, indicative of a slight misorientation between adjacent subgrains that form during solidification. After heat treatments are applied, the RSP alloy 718 retains its subgrain microstructure (Figure 28 area a and Figure 29a compared to Figure 29b) that includes the interdendritic eutectic and Laves phases at the subgrain boundaries. The aging heat treatment does result in the precipitation of carbides, as well as γ" (Ni_3Nb), and γ' ($Ni_3(Al,Ti)$) strengthening phases within the cellular subgrains (Figure 29b). The subgrain size is strongly dependent on the cooling rate, with a measured primary cell spacing ranging from 0.4 to 1.5 μm indicating that very high cooling rates are present [82]. The morphology of the subgrain is determined by the ratio of the temperature gradient *G* at the solid/liquid interface to the solidification rate (interface velocity) *R*. The obtained cellular or cellular dendritic morphology is indicative of a *G*/*R* ratio too large to fully form secondary dendrite arms.

In contrast to the RSP alloy 718, the solution annealed (SA) alloy 718 contains equiaxed grains almost completely composed of high angle (60°) grain boundaries, which are retained after heat treatment (Figure 28 area b). The lack of low angle solidification subgrain boundaries is indicative of recrystallization having occurred. After the aging heat treatment, the SA + aged alloy 718 forms carbides, γ", and γ' phases within the grain boundaries (Figure 29c). This aging heat treatment results in optimal strength and mechanical properties, arising from a γ" precipitate size of approximately 20 nm.

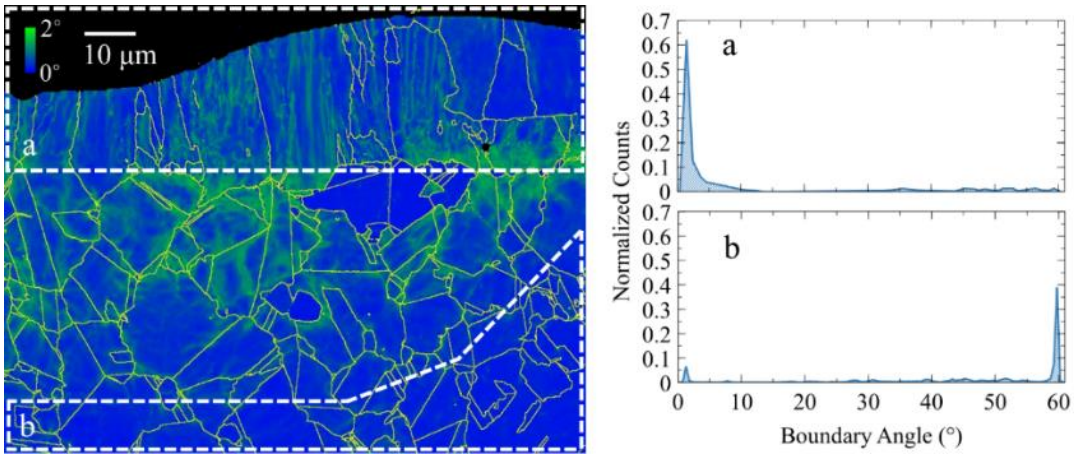

Figure 28. EBSD kernel average misorientation map of a direct aged alloy 718 a) coating and b) substrate with a respective count of grain boundary angle. Sample was exposed to 900 °C for 0.5 h to allow for proper indexing of the coating.

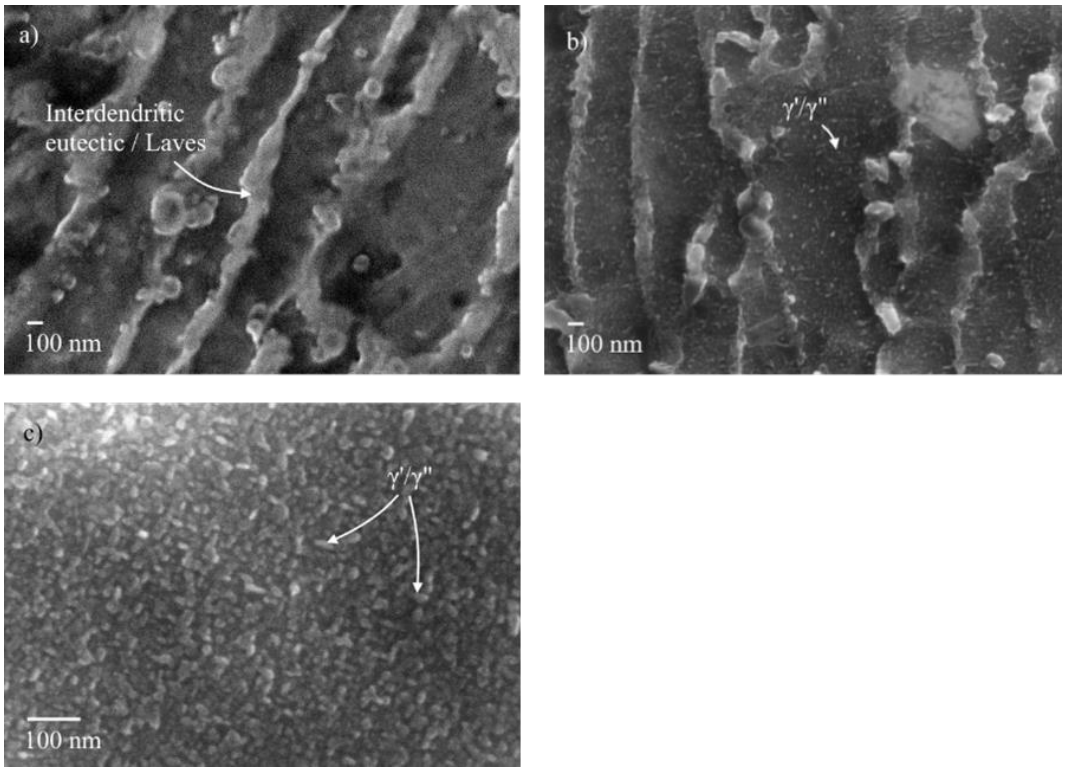

Figure 29. SEM images of the microstructure in a) RSP alloy 718, b) RSP + aged alloy 718, and c) SA + aged alloy 718

Exposure of the RSP + aged alloy 718 and SA + aged alloy 718 to elevated temperatures and longer durations results in significant phase evolution. RSP + aged alloy 718 forms the δ phase at the interdendritic region along the subgrain boundaries, as shown in Figure 30a. AES results in

Figure 30d show the clear presence of Nb and Ni peaks at these locations. The presence of C and O peaks are due to contamination and oxidation on the sample surface, and their high peaks can be attributed to the high surface sensitivity of AES. Higher magnification images (Figure 30b) show that precipitation of the γ" phase with Ni_3Nb composition - identifiable due to its elliptical cross-sections and the presence of Nb and Ni Auger peaks in Figure 30f - also occurs preferentially near the Nb-enriched subgrain boundaries. However, the spherical γ' phase forms throughout the γ matrix, since its $Ni_3(Al,Ti)$ composition is not influenced by Nb micro-segregation at the subgrain boundaries. AES spectra of these spherical phases show clear Ti and Ni peaks (Figure 30c), and analysis of the γ matrix in the core dendrite region also shows a sharp Ti peak, alongside the expected Cr, Fe and Ni peaks (Figure 30e).

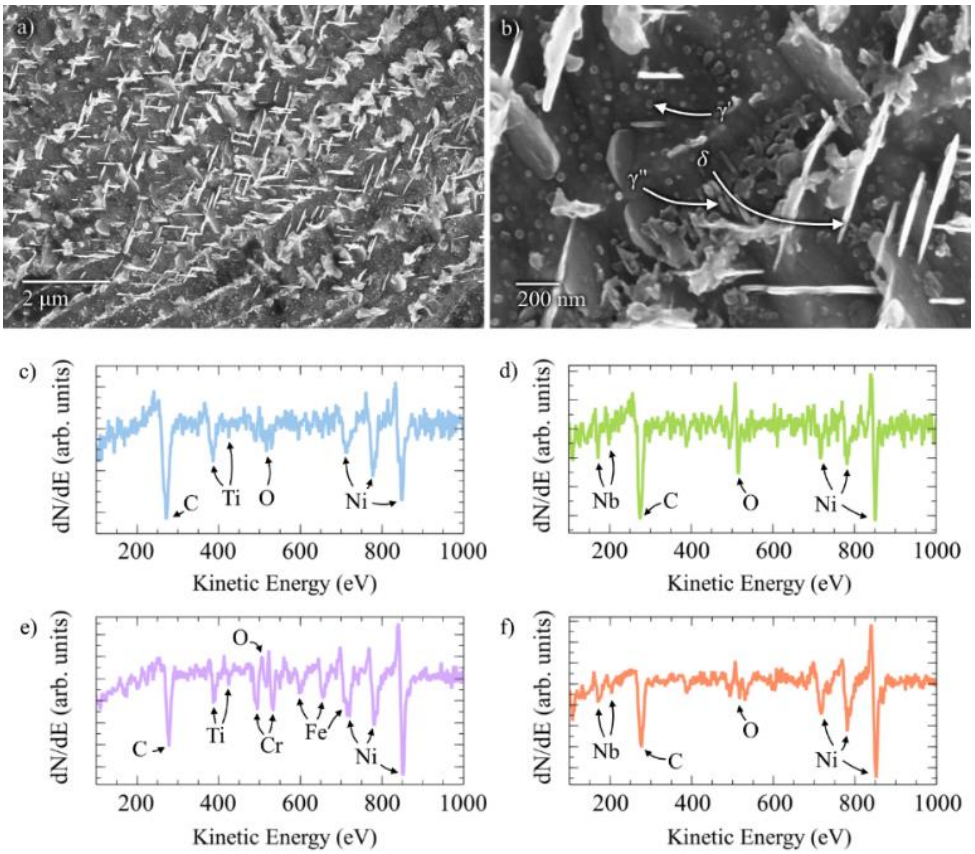

Figure 30. SEM images of the etched microstructure in a) RSP + aged alloy 718 exposed to 800 °C for 4 h, b) higher magnification image of the interdendritic region, AES derivative spectrum of c) γ' phase, d) δ phase, e) γ matrix in the dendrite core, and f) γ" phase

Similar microstructure evolution is observed in RSP + aged alloy 718 at 700 °C (Figure 31a), 800 °C (Figure 31b), and 900 °C (Figure 31c), although with differing times required before the δ phase is observed. The microstructure in Figure 31 shows differences in subgrain growth directions between adjacent grains in the RSP + aged alloy 718. This difference can be attributed to the substrate grain orientation, a small portion of which is shown in the images in Figure 31. During solidification, the heterogeneous nucleation of grains on the substrate is expected to be more favourable than the growth of new grains via homogeneous nucleation. As such, the nucleated grains adopt the crystallographic orientation of the grains in the substrate and the subgrains that form can appear tilted when viewed along the cross-section.

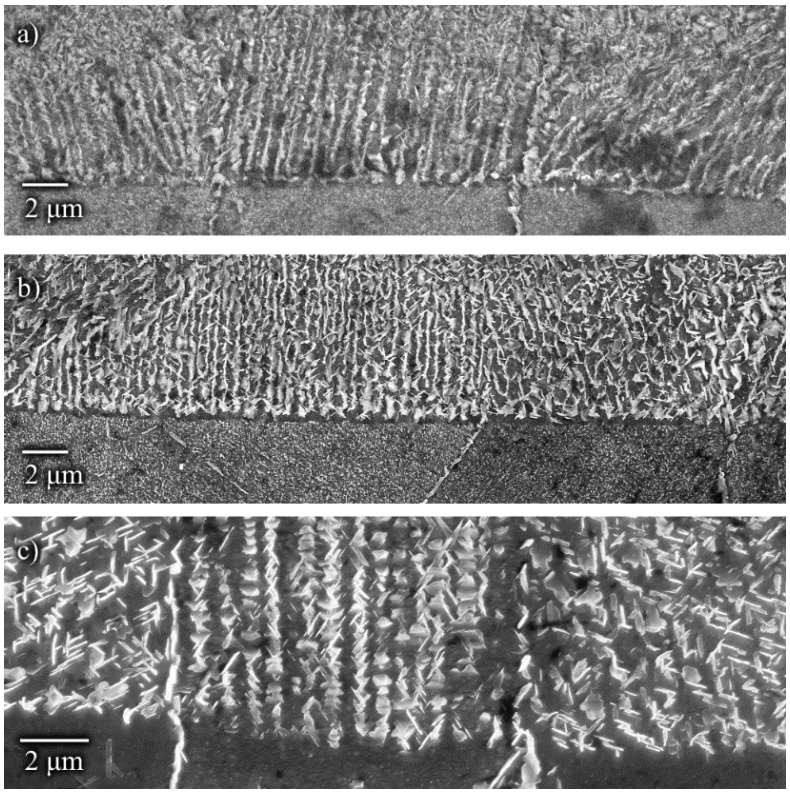

Figure 31. SEM images of the etched microstructure in RSP + aged alloy 718 after exposure to a) 700 °C for 100 h, b) 800 °C for 2 h, and c) 900 °C for 0.5 h. A portion of the substrate is visible at the bottom of each image.

In SA + aged alloy 718, the γ” phase also experiences coarsening while the δ precipitates grow at the grain boundaries (Figure 32a). The formation of a γ” depletion region surrounding the δ phase (Figure 32b) suggests that formation of δ precipitates occurs alongside the dissolution of γ”, and contrasts sharply with the RSP + aged alloy 718 which showed a clustering of both γ” and δ

precipitates at the subgrain boundaries (Figure 30b). Alongside coarsening of the γ" phase, a change in the γ" morphology from a rounded, short disc shape to a more elongated shape with sharper features is observed. Similar changes in morphology have been previously observed in the literature for over-aged γ" particles in alloy 718 [37,138,139] and other similar alloys [140].

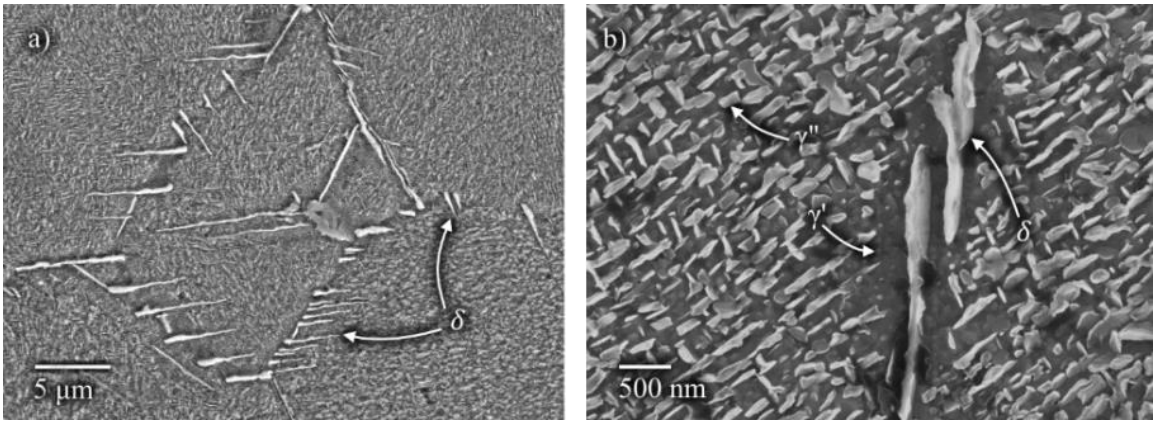

Figure 32. SEM images of etched microstructure in a) SA + aged alloy 718 exposed to 800 °C for 24 h and b) higher magnification image showing δ phase with adjacent region depleted of γ"

5.3.2 Formation of the δ phase

The formation of a new phase occurs in three stages: nucleation, growth, and coarsening. Nucleation occurs when a cluster of atoms forms a thermodynamically stable nuclei larger than the critical radius, which is a function of the change in volume Gibbs free energy and interfacial energy [141]. The presence of compositional variations due to micro-segregation is expected to facilitate the formation of nuclei at subgrain boundaries for the δ phase in alloy 718. Once the critical radius is surpassed, growth of the precipitate occurs via the attachment of atoms diffusing from the surrounding solid solution. As growth progresses, coarsening begins to occur via the dissolution of smaller precipitates. The number of sites at which nucleation occurs therefore governs the number of precipitates that form and, along with the coarsening rate, governs the precipitate size. These aspects can be used to explain the disparity in δ precipitate microstructure between RSP + aged and SA + aged alloy 718.

In the case of RSP + aged alloy 718, Nb is available at subgrain boundaries due to micro-segregation during solidification. SA + aged alloy 718 has been shown to experience grain boundary segregation and precipitation [142,143] when exposed to elevated temperatures. To quantify the number of potential nucleation sites at grain and subgrain boundaries, a nucleation

site model is applied. Grains and subgrains are approximated as adjacent tetrakaidecahedrons, with surfaces, edges, and corners considered sites that favor nucleation. The number of grain/subgrain surface (N_s), edge (N_e) and corner nucleation sites (N_c) are expressed in Equations (22) to (24), respectively. These equations are constructed by taking expressions for surface area, edge length, or corner sites in one embedded tetrakaidecahedron as shown by Rajek [144] and extended to a volume of 1 m^3.

$$N_s = \frac{6\left(1+2\sqrt{3}\right)\lambda^2 + 2\lambda(2H+\lambda)}{16\sqrt{2}\lambda + 12\lambda^2 H}\left(\frac{N_A}{V_m}\right)^{\frac{2}{3}} \quad (22)$$

$$N_e = \frac{36\lambda + 8H}{24\sqrt{2}\lambda + 18\lambda^2 H}\left(\frac{N_A}{V_m}\right)^{\frac{1}{3}} \quad (23)$$

$$N_c = \frac{6}{8\sqrt{2}\lambda + 6\lambda^2 H} \quad (24)$$

In Equations (22) to (24), N_A is Avogadro's number, V_m is the molar volume of Ni (6.6×10^6 m^3mol^{-1}), λ is dependent on the grain/subgrain diameter (d) as shown in Equation (25), and H is dependent on the grain/subgrain diameter and length (D) as shown in Equation (26).

$$\lambda = \frac{d}{\sqrt{10}} \quad (25)$$

$$H = \sqrt{\left(D^2 - \frac{d^2}{5}\right)} - 2\sqrt{\frac{d^2}{5}} \quad (26)$$

The use of diameter and length values representative of the microstructure visible in Figure 28 and Figure 29b result in a 3.5 times increase in available nucleation sites within the RSP + aged alloy 718 when compared to the SA + aged alloy 718 (Table 14). The corresponding difference in precipitate size can be evaluated by considering the thin disk-like shape of the δ phase [145] and a 3.5 times difference in volume as a result of the difference in nucleation sites. Assuming the precipitate size is scaled proportionately along the thickness and diameter dimensions, the following expression can be used to relate the volumes of δ precipitates in the RSP + aged alloy 718 (V_{RSP}) and SA + aged alloy 718 (V_{SA}):

$$V_{SA} = 3.5V_{RSP} = 2.4l_{RSP}\pi\left(\frac{2.4d_{RSP}}{2}\right)^2 \quad (27)$$

where the diameter (d_{RSP}) and thickness (l_{RSP}) of a δ precipitate in the RSP + aged alloy 718 (with the subgrain boundaries) are expected to be smaller by a factor of 2.4 when compared to a δ precipitate in the SA + aged alloy 718 (without subgrains boundaries). Although the difference in the number of nucleation sites is used to establish a relationship between the δ precipitate sizes in the two alloy 718 conditions, the actual δ precipitate sizes are also a function of the coarsening rate, which is influenced by the heat treatment time and temperature.

Table 14. Nucleation sites in an RSP + aged alloy 718 and SA + aged alloy 718 using a tetrakaidecahedron model

	RSP + aged		**SA + aged**
	Subgrain	**Grain**	**Grain**
d [m]	5×10^{-7}	7.6×10^{-6}	5.7×10^{-6}
D [m]	2×10^{-5}	2×10^{-5}	5.7×10^{-6}
N_s [m^{-3}]	4.5×10^{25}	4.9×10^{24}	1.4×10^{25}
N_e [m^{-3}]	8.2×10^{22}	4.7×10^{20}	1.5×10^{21}
N_c [m^{-3}]	2.0×10^{18}	9.9×10^{15}	9.1×10^{16}
Total sites [m^{-3}]	5.0×10^{25}		1.4×10^{25}

The coarsening of δ precipitates in RSP + aged and SA + aged alloy 718 is expected to follow the Lifshitz-Slyozov-Wagner theory of Ostwald ripening for volume diffusion-controlled coarsening. This has previously been used to model the growth of γ" precipitates [146,147], with modifications made to account for the disc-shaped particle morphology [148]. These same modifications can be used for the disc-shaped δ phase, such that the coarsening of the δ particles follows:

$$d^3 = kt + d_0^3 \qquad (28)$$

where t is the time, d is the particle diameter, d_0 is the initial particle diameter at $t = 0$, and k is a combination of the diffusion coefficient (D), temperature (T), precipitate interfacial energy (γ), equilibrium concentration of the solute species (c_0), precipitate volume (V_m), particle aspect ratio (K), and the ideal gas constant (R) as shown in Equation (29). The diffusion coefficient can be further expanded into Equation (30), which is shown to depend on the activation energy (E_a) and temperature.

$$k = \frac{128}{9\pi}\frac{\gamma K c_0 V_m^2 D}{RT} \qquad (29)$$

$$D = D_0 \exp\left(\frac{-E_a}{RT}\right) \qquad (30)$$

Equation (28) is used to produce best fit curves for experimental measurements of δ precipitate size in RSP + aged and SA + aged alloy 718 after exposure to 800 °C, shown as the dashed lines in Figure 33. Equation (27) is used to generate a prediction of the δ precipitate size in SA + aged alloy 718 based on the measured sizes (orange circles) in RSP + aged alloy 718. The 99% confidence interval for this prediction is shown in Figure 33 as the grey shaded region and an excellent match between the predicted and measured precipitate size for SA + aged alloy 718 (in red) is obtained. This suggests that the difference in precipitate size between RSP + aged and SA + aged alloy 718 is accurately explained by the increase in nucleation sites made available due to micro-segregation that occurs at subgrain boundaries during solidification, and the change in precipitate size over time follows a Lifshitz-Slyozov-Wagner model.

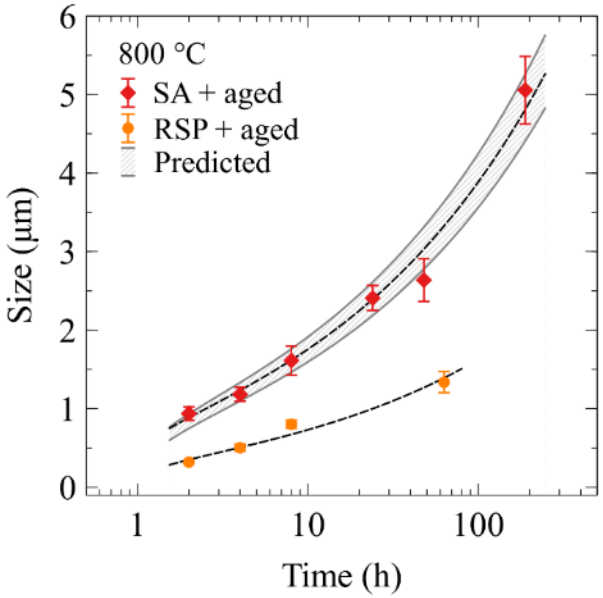

Figure 33. a) Growth of δ phase in RSP + aged and SA + aged alloy 718

Experimental measurements of the δ particle diameters at three temperatures in the RSP + aged alloy 718 are shown in Figure 34a. Equation (28) is used to apply a best fit curve to the measured data at each of the studied temperatures and the fit parameters are reported in Table 15. The value of k – which indicates how strongly the heat treatment affects the precipitate size – increases by

two orders of magnitude within the temperature range investigated. This is explained by the temperature dependence of the diffusion coefficient (D), as shown in Equation (30), and suggests that the coarsening mechanism of the δ phase along the subgrain boundaries is dependent on diffusion. When exposed to 700 °C and 800 °C, the δ phase was not observed until 100 h and 2 h respectively. Samples in which no δ precipitates were observed are marked in Figure 34a as having a 0 µm size.

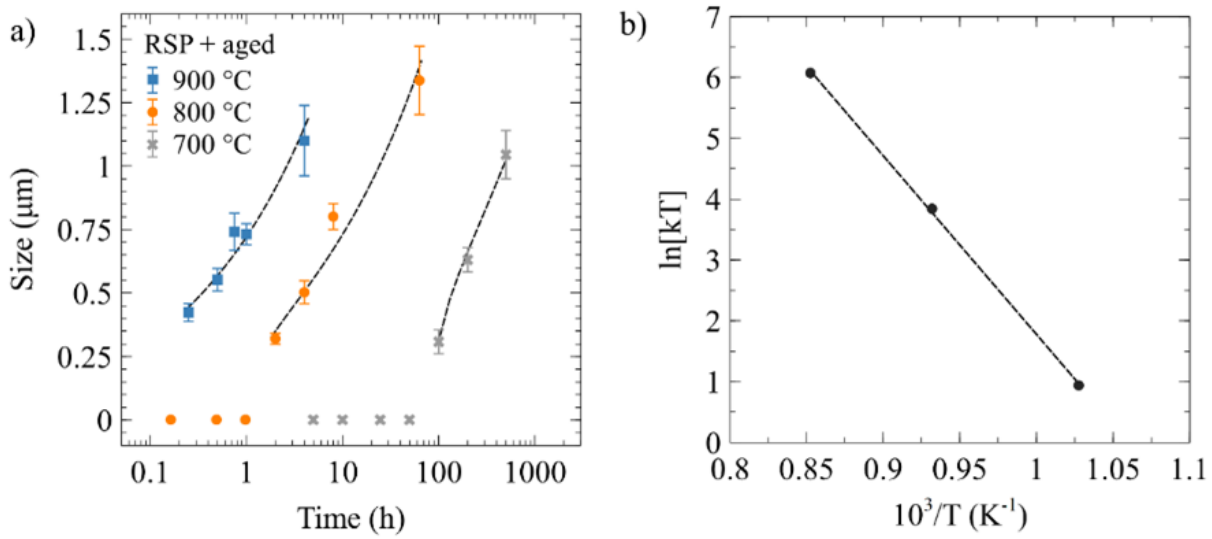

Figure 34. a) Size of the δ phase in RSP + aged alloy 718, b) an Arrhenius plot derived from the δ size measurements in (a)

Table 15. Model parameters for Equation (28) obtained from Figure 34a and the R-squared (R^2) statistic for model fit

Temperature (°C)	k **(µm² h⁻¹)**	d_0 **(µm)**	R^2
700	0.0026	-0.62	0.99
800	0.043	-0.35	0.97
900	0.38	-0.20	0.96

A further understanding of the δ phase coarsening mechanism can be obtained by determining the activation energy for diffusion. The expression resulting from the substitution of Equation (30) into Equation (29) can be rearranged into an Arrhenius form as shown in Equation (31), under the assumption that γ, K, c_0, V_m and D_0 are independent of temperature. The value of $\ln(kT)$ can then be plotted (Figure 34b) against $1/T$ using the values in Table 15, and the activation energy (E_a)

can be determined from the slope of the best fit line. This activation energy for δ coarsening (244 kJ mol^{-1}) compares favorably to the activation energy for Nb diffusion in a Ni-superalloy (237 kJ mol^{-1} [149]), suggesting that Nb diffusion through the matrix is the limiting factor for δ phase coarsening in RSP alloy 718 with micro-segregation at the subgrain boundaries, rather than the dissolution of the Laves phase (275 kJ mol^{-1} [150]). One might expect that Laves dissolution would be rate limiting, since the activation energy for Laves dissolution is greater than that of Nb diffusion. However, if sufficiently large sources of solutionized Nb are available in the Ni matrix, the comparatively slow dissolution of the Laves phase would be of lesser consequence. Due to the formation of a Nb-rich interdendritic eutectic at the subgrain boundaries, this is likely the case in RSP alloy 718.

$$\ln(kT) = -\frac{E_a}{R}\frac{1}{T} + \ln\left(\frac{128}{9\pi}\frac{\gamma K c_0 V_m^2 D_0}{R}\right) \qquad (31)$$

5.3.3 Effect of the δ phase on mechanical properties

A comparison of RSP + aged alloy 718 after 0 h, 4 h, and 70 h of exposure to 800 °C shows an initial degradation in mechanical properties between 0 h and 4 h, and less significant changes afterwards (Figure 35). Both ultimate tensile strength (UTS) and microhardness experienced a decrease of 15% and 21%, respectively, after 70 h of heat treatment. The observed trend is broadly comparable to results previously reported in literature for alloy 718 [37], which observe a rapid initial drop and a more gradual decline afterwards.

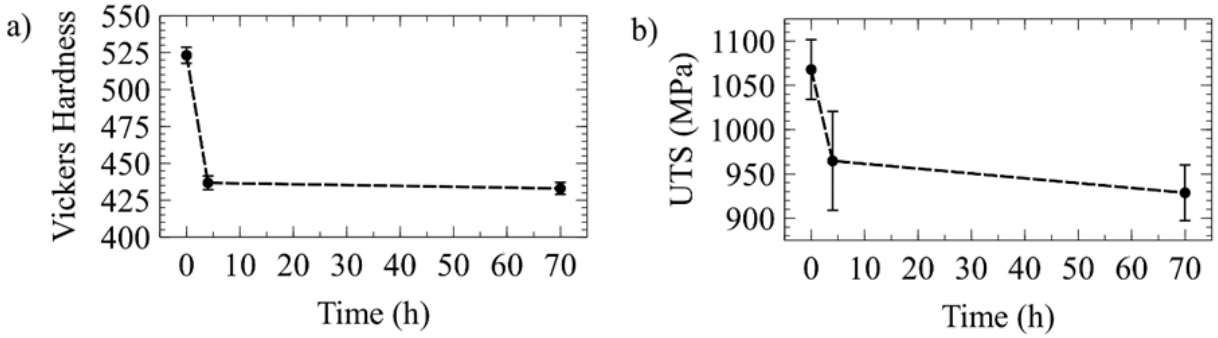

Figure 35. The influence of exposure time at 800 °C for a RSP + aged alloy 718 on a) microhardness and b) ultimate tensile strength (UTS)

All samples had sharp features on the fracture surface (Figure 36a), with dendritic features visible at higher magnification (Figure 36b), suggesting that plastic deformation is limited. As was shown previously in RSP [102] and RSP + aged [137] alloy 718, the crack propagation pathway continues to occur along subgrain and droplet boundaries according to the relative fracture toughness [102] even after the formation of the δ phase. However, in samples heat treated for 4h and 70h, many instances of secondary crack propagation show unbroken δ precipitates bridging the crack path (Figure 36c), as well as δ precipitates protruding from the primary fracture surfaces (Figure 36d). As a result, crack propagation does appear to be influenced by the presence of δ precipitates. Crack initiation was found to occur from the part surface or from Al- and Ti-rich oxide defects (Figure 36e) regardless of heat treatment time.

The crack propagation mechanism appears to switch from the typical particle cracking mode reported when only the Laves phase is present to a combination of micro void formation and interface debonding [151]. In addition to differences in properties between the δ and Laves phase, the orientation and growth of the δ phase into the γ matrix may introduce increased resistance to crack propagation by increasing the crack path tortuosity and slowing crack propagation occurring at lower stress levels. This has been shown in direct aged alloy 718 to have a notable influence on fatigue and creep properties [152], with a greater amount of δ phase particles more effectively reducing the crack propagation rate. For RSP + aged alloy 718, the use of longer heat treatments that produce δ precipitates > 1 μm in size are expected to be more effective at increasing crack propagation resistance, based on studies from other materials with grain boundary precipitates [151]. In combination with the dissolution of the brittle Laves phases, this would be expected to improve mechanical properties. However, these potential positive mechanisms occur alongside negative effects such as the coarsening of the γ” phase – the primary strengthening phase in alloy 718 – and the transformation of γ” into δ [37]. Previous studies have shown that a proper balance can be achieved between the reduced strength from dissolution of the γ” phase and formation of the δ phase, such that strength requirements are still met for most applications while significantly improving fatigue and creep properties [152].

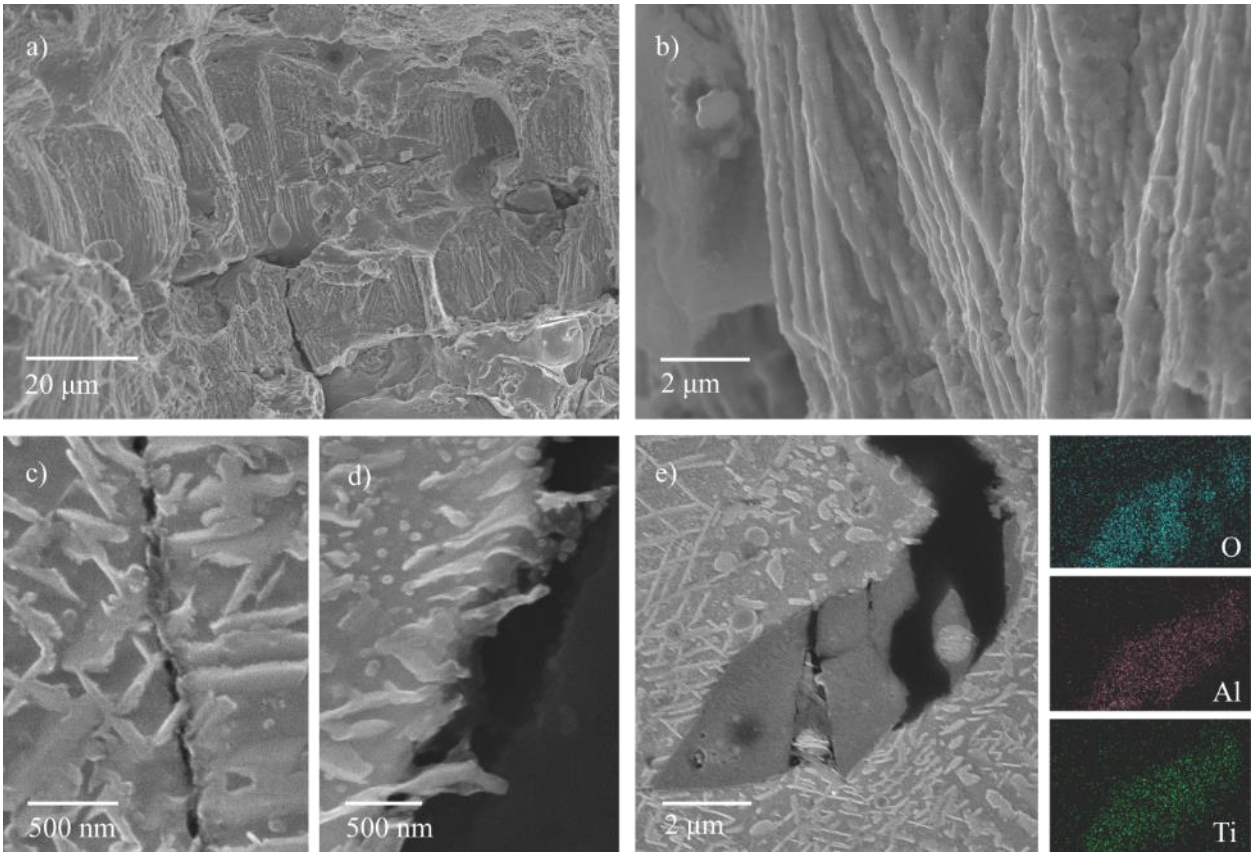

Figure 36. SEM images from tensile specimens exposed to 800 °C for 70 h showing a) fracture surface, b) high magnification of fracture surface showing dendritic features, cross-sections of fractured surface showing c) secondary crack pathway and d) crack pathway along primary fracture surface, and e) site of crack initiation with EDX maps for O, Al, and Ti

5.4 Conclusion

Micro-segregation at subgrain boundaries affects the precipitation of the δ phase in rapid solidification processed and aged (RSP + aged) alloy 718 by providing a greater number of nucleation sites, which results in a greater number of proportionally smaller δ precipitates than in a solution annealed and aged (SA + aged) alloy 718 without micro-segregation or subgrain boundaries. The coarsening of δ precipitates in RSP + aged alloy 718 follows a Lifshitz-Slyozov-Wagner model and the activation energy for coarsening matches that of Nb diffusion, suggesting that Laves or γ" dissolution is not the limiting factor.

The methodology used in this study establishes a clear relationship between the nucleation site density and the secondary phase size in rapid solidification processed alloys with critical alloying

elements found at the subgrain boundaries. This influences not only the precipitate size, but also the distribution, which can be expected to influence mechanical properties. In the present study, the formation of fine subgrain boundary δ phase precipitates in RSP + aged alloy 718 is found to negatively influence hardness and ultimate tensile strength. Although δ precipitates appear to positively influence the crack propagation pathway during tensile fracture, the observed decrease in mechanical properties is primarily attributed to coarsening and transformation of the γ" strengthening phase that occurs alongside δ phase coarsening. This highlights the importance of understanding the microstructure evolution in micro-segregated alloys, which can allow for the prediction and control of precipitate size, precipitate distribution, and mechanical properties.

Chapter 6. Application of ESD to LPBF-made parts

6.0 Preface

This chapter addresses the application of ESD as a surface modification technique for additive manufactured parts. ESD is used to apply a coating of Inconel 718 on an LPBF-made Hastelloy X substrate to address the negative influence of high surface roughness and near-surface porosity on fatigue performance. Previous studies on the effect of microstructure on mechanical properties and phase transformations were used to guide processing conditions for this study. Even though the use of heat-treatment processes to remove the solidification microstructure and/or precipitate the strengthening phase were investigated, the best fatigue life was achieved in the non heat-treated condition. Additionally, even though oxides were sometimes identified as a source of crack initiation in the previous studies, crack initiation in fatigue tests was found to initiate from the surface of the LPBF part in the as-built and post-processed condition.

This chapter is based on a published paper [79].

6.1 Introduction

Additive manufacturing (AM) processes such as laser powder bed fusion (LPBF) provide significant advantages over traditional manufacturing. With reduced material waste when compared to subtractive processes and considerable geometrical freedom, LPBF is an especially attractive option for the manufacturing and lightweighting of parts made from high value materials. However, despite significant research into the subject, LPBF parts still suffer from relatively low surface quality. This has been shown to result in reduced fatigue performance, since fatigue cracks frequently initiate from surfaces at locations with higher stress concentrations [12,13,153]. Increased surface roughness can also negatively affect aerodynamic performance – such as in the case of turbine blades or vanes – by interacting with the boundary layer of air that flows across the surface and introducing flow instabilities [154–156].

The causes of surface roughness have been attributed to a variety of factors, including print positioning on the build plate [157], the ejection of spatter particles [158,159], the stair-step effect, and LPBF process parameters such as the printed surface orientation and thermal history [157,160,161], linear energy density, laser power, and hatch spacing [162,163]. Although process

parameters can be optimized to obtain acceptable quality surfaces [164], the other contributing factors make surface quality highly variable within a single part or between parts on the same build plate. For commercial applications, some amount of post-processing that addresses surface quality is usually required.

Many surface finishing techniques are available and can be chosen based on the required final surface roughness, desired surface properties, and geometrical complexity of the part being processed. Machining is a traditional method for reducing external surface roughness [55,165], but results in material waste and is difficult to use on complex geometries. Machining is also more challenging on work hardening materials such as Ni-superalloys [166]. A reduction in surface roughness is possible via in situ layer re-melting [77] or post-process laser polishing [167] in additive manufactured parts. This technique has been demonstrated for nonplanar surfaces as well [168], although more geometrically complex parts with overhangs, lattice structures or internal channels that are not easily accessible must be addressed using other techniques.

One technique for reducing the surface roughness of internal channels – abrasive flow machining – requires a fluid with abrasive particles capable of eroding or producing micro-cuts on the part surface. Applications to additive manufactured parts have found notable reductions in surface roughness [169], although the long processing times and inconsistent material removal that depend on local shear strain rates introduce some challenges [170]. Another technique is chemical etching or electropolishing, which is shown to achieve a significant surface roughness reduction [171]. However, several disadvantages exist: this process often results in excessive material removal that can affect part tolerances [172], large features are not easily removed, the preferential dissolution of some phases in multiphase alloys can cause short range roughening [173], and conventional electropolishing methods are generally expensive, hazardous to workers, and environmentally harmful [174]. A combination of surface finishing techniques can be beneficial for applications that require a greater reduction in surface roughness and can overcome the individual disadvantages of a single process [175]. A 2-step abrasive flow machining and electrochemical machining process was successfully shown to reduce surface roughness by 80% in LPBF-made laser cutting nozzles, while improving performance over the as-built condition to match that of a conventionally manufactured part [78]. Another example identifies a 3-step process of glass

blasting, vibration deburring, and dry electropolishing capable of reducing surface roughness by 93% [77].

The influence of surface finishing techniques on fatigue properties have been frequently demonstrated in literature. Abrasive and impact surface finishing techniques have shown notable improvements in fatigue life; the use of ultrasonic shot peening on thin struts built by electron beam melting was shown to achieve a 2 times improvement in the cycles to failure, while sandblasting was shown to improve the cycles to failure by an order of magnitude [176]. The improvements are typically attributed to a reduced surface roughness, the introduction of compressive residual stresses or microstructural changes.

Many of these surface finishing techniques have the common characteristic of deforming or removing material from the surface. Rather than use a subtractive process, this study demonstrates the use of an additive electrospark deposition (ESD) technique and machine hammer peening to reduce surface roughness while improving the properties of external surfaces in LPBF-made Hastelloy X parts. The ESD process melts rough features on the part surface and introduces beneficial surface properties by depositing an Inconel 718 coating, while machine hammer peening flattens surface features and allows for longer ESD processing times. The combination of these two processes achieves greater surface roughness reduction with shorter processing times than the individual application of ESD or hammer peening. Several heat treatments are also investigated to address residual stresses and promote a precipitation hardening effect in the deposited Inconel 718. Although Inconel 718 and Hastelloy X are both Ni-superalloys, appropriate processing of Inconel 718 can obtain a significantly higher hardness and strength than Hastelloy X [38]. As a result of ESD and hammer peening, the surface and fatigue properties of LPBF-made Hastelloy X parts are significantly improved.

6.2 Materials and Methods

6.2.1 Laser Powder Bed Fusion (LPBF)

In this study, an EOS M290 equipped with an Ytterbium fiber laser and gas atomized Hastelloy X powder with a D50 (median diameter) of 29.3 µm were used to manufacture cubic LPBF parts (10 × 15 × 30 mm). All samples were made with similar processing parameters (laser power of 200 W, laser velocity of 900 mm/s, layer thickness of 0.06 mm and hatching spacing of 0.08 mm)

using a rotated stripe scanning strategy. The build plate temperature was maintained at 80 °C during the process. These samples were then post-processed for surface roughness analysis, microhardness measurements, and microstructure characterization. The same process parameters were also used to create fatigue testing samples described below.

6.2.2 Electrospark Deposition (ESD) and hammer peening

The side surfaces of LPBF parts were post-processed using a manually operated ESD machine and handheld machine hammer peening tool provided by Huys Industries. ESD operates by discharging a capacitor through a consumable electrode and conductive substrate. A 3.2 mm diameter Inconel 718 electrode was used as shown in Figure 37a. During the process, small molten droplets from the electrode (Figure 37b) are transferred to the substrate and solidified (Figure 37c). Ultra-high purity argon shielding gas was delivered coaxially around the electrode during deposition, and ESD parameters of 100 V, 80 µF and 150 Hz were used based on previous studies that show high density and good mechanical properties [102,137]. Coatings were applied to 10 mm by 10 mm regions for various spark durations (25 s, 75 s, 125 s) in a raster scan pattern, with the pattern rotated 90 ° between layers. The machine hammer peening tool operates by driving a 2.5 cm long, 4.8 mm diameter hardened tool steel rod using a rotating 21 g weight offset by 0.64 mm (Figure 38). Rotation occurs at a frequency of 100 Hz, and the vibration amplitude at the rod tip is 0.5 mm. When peening was used, the ESD process was stopped every 12.5 s and peening was applied to the entire coated area.

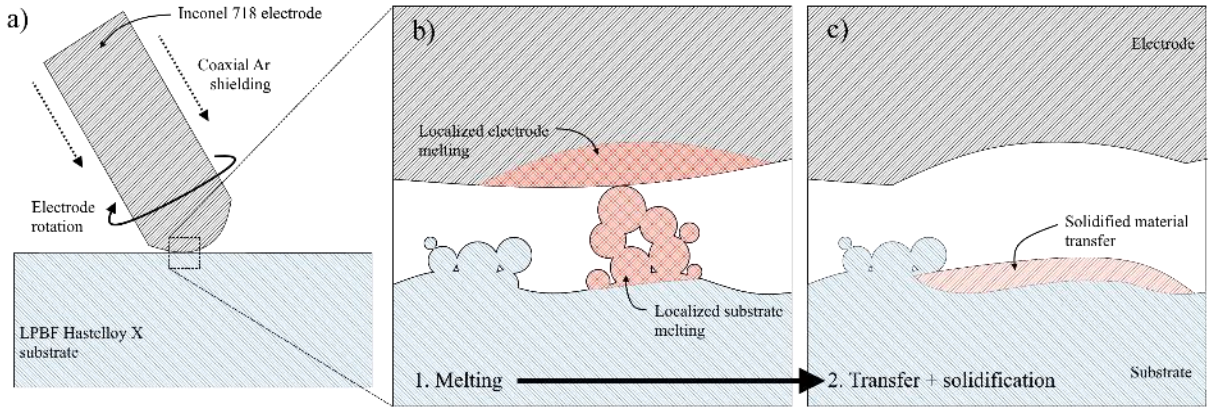

Figure 37. Schematic showing a) overview of electrode and substrate, b) localized melting of electrode and substrate during ESD, and c) material transfer and solidification

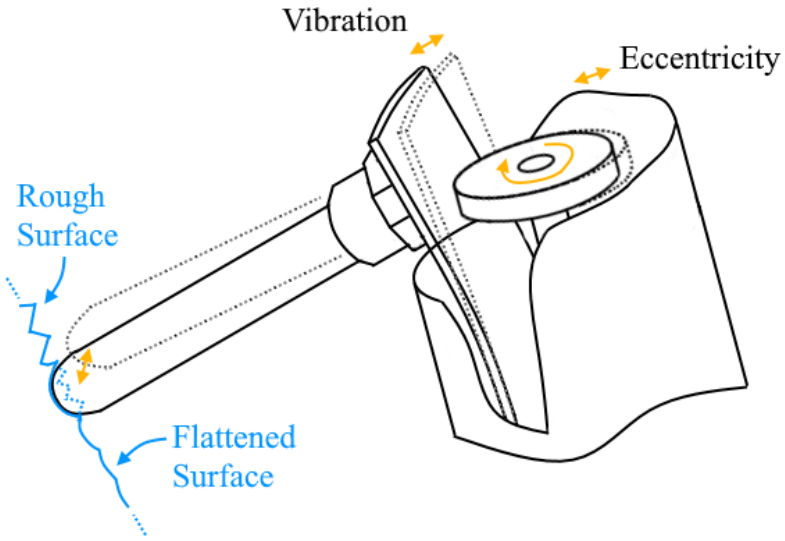

Figure 38. Schematic of hammer peening tool mechanism showing vibration of a rod driven by the rotation of an eccentric weight

6.2.3 Heat Treatment

Inconel 718 coated Hastelloy X samples were studied in several heat-treated conditions, described in Table 16. All heat treatments were performed in a horizontal quartz tube furnace under ultra-high purity argon gas, with a flow rate of 4 L/min and 250 Pa of positive pressure. The aging temperature and time is selected based on the industry standard for Inconel 718 [177], and the solution annealing temperature and time is selected based on literature studies of secondary phase dissolution in rapid solidification processed Inconel 718 [178].

Table 16. Heat treatments for Inconel 718 coated Hastelloy X samples

Sample	**Heat Treatment**
Direct Aged (DA)	720 °C for 8 hrs, 620 °C for 10 hrs, air cooled
Solution Annealed (SA)	1100 °C for 1 hr, water quenched
Solution Annealed and Aged (SAA)	1100 °C for 1 hr, water quenched 720 °C for 8 hrs, 620 °C for 10 hrs, air cooled

6.2.4 Characterization

Microstructure characterization was performed using a Zeiss UltraPlus scanning electron microscope (SEM) with an AMETEK EDAX Apollo XL energy-dispersive X-ray spectroscopy

(EDX) attachment. A TESCAN SEM was used for the analysis of fatigue fracture surfaces, and an Oxford electron backscatter diffraction (EBSD) detector in a JEOL7000F SEM was used for analysis of samples after heat treatment. A surface profile was obtained with a Keyence VK-X250 confocal laser microscope, and hardness results were obtained using a load of 0.1 kgf on a Wolpert Wilson 402 MVD micro Vickers hardness tester.

A combination of ESD, peening, and heat treatments were used to create several post-processed samples for surface profile analysis, microhardness evaluation, and fatigue testing. A breakdown of samples created for each analysis is provided in Table 17.

Table 17. Post-processed LPBF Hastelloy X samples

Analysis	**Sample**	**Sample Description**
Surface Profile	As-built	No surface treatment
	ESD	With ESD Inconel 718 coating
	ESD+HP	With ESD Inconel 718 coating and hammer peening
	HP	With hammer peening
Microhardness	ESD	With ESD Inconel 718 coating
	ESD+HP	With ESD Inconel 718 coating and hammer peening
	ESD+HP+DA	With ESD Inconel 718 coating, hammer peening and direct aging heat treatment
	ESD+HP+SA	With ESD Inconel 718 coating, hammer peening and solution annealing heat treatment
	ESD+HP+SAA	With ESD Inconel 718 coating, hammer peening, and solution annealing + aging heat treatment
Fatigue life	As-built	No surface treatment
	HP	With hammer peening
	ESD+HP	With ESD Inconel 718 coating and hammer peening
	ESD+HP+DA	With ESD Inconel 718 coating, hammer peening and direct aging heat treatment

6.2.5 Fatigue Testing

Post-processing of ESD+HP samples for fatigue testing consists of two layers of ESD Inconel 718 applied to the necked region of the fatigue specimens (built in a vertical orientation with

dimensions shown in Figure 39a), with peening performed at the conclusion of each layer. A second set of post-processed HP samples received an equivalent amount of peening as ESD+HP samples, without the application of an Inconel 718 coating using ESD. The last set of post-processed samples (ESD+HP+DA) were processed similarly to the ESD+HP samples, with the addition of a direct aging heat treatment. The resulting post-processed samples are compared to samples in the as-built condition, shown in Figure 39b.

An Instron 8872 servohydraulic fatigue testing system was used to test the room temperature fatigue performance of LPBF Hastelloy X samples with and without post-processing using a stress ratio ($R = \frac{S_{min}}{S_{max}}$) of 0.1 in tension-tension mode. Low cycle fatigue testing was performed at a maximum stress of 550 MPa while the high cycle fatigue testing was done at a maximum of 350 MPa. A frequency of 5 Hz was used for all samples except the post-processed samples tested at high cycle fatigue conditions. These samples were tested at a frequency of 5 Hz until 10^6 cycles, and then switched to 30 Hz due to the long test durations.

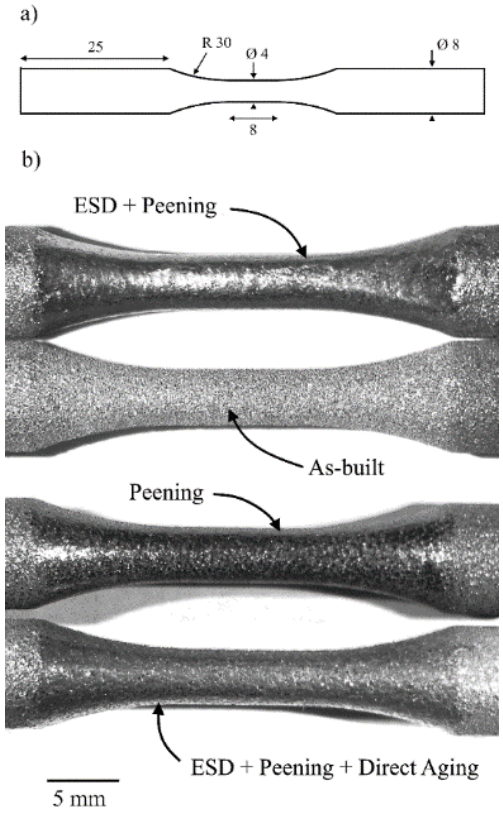

Figure 39. a) Fatigue testing specimen dimensions in mm and b) samples in the as-built and post-processed conditions

6.2.6 Surface profile processing

To distinguish long-range and short-range imperfections (waviness and roughness), raw height data (Figure 40a) was processed in MATLAB by applying a gaussian filter according to ISO 16610-21 [179]. The long wave component (Figure 40b) was used to calculate the arithmetic mean height of the surface waviness (W_a), while the short wave component (Figure 40c) was used to calculate the arithmetic mean height of the surface roughness (S_a).

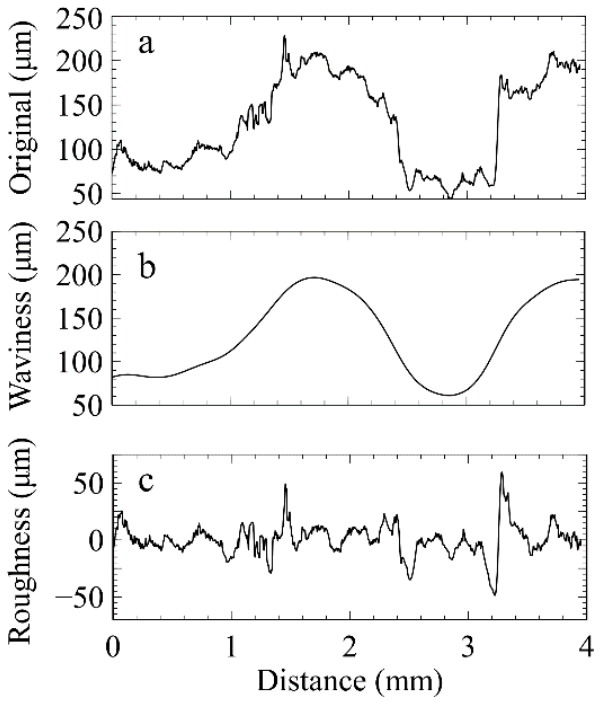

Figure 40. a) Original surface profile of an as-built sample, b) long wave portion of surface profile, and c) short wave portion of surface profile

6.3 Results and discussion

6.3.1 ESD post-processing

The most notable features on the side surface of as-built parts are the partially fused particles (PFPs) shown in Figure 41a. The adherence of these powder particles to the side surface can be attributed to loose powder adjacent to the melt pool or spatter directed into the melt pool during the LPBF process [158]. In these conditions, partial melting of the powder in the liquid melt pool or the formation of sinter necks between the powder and the recently solidified melt pool will occur. Some roughness can also be attributed to the underlying surface, which shows distinct melt

pool tracks because of the contour step performed on each layer. Since the side walls are vertical, other common contributors to surface roughness – such as the staircase effect in which angled surfaces are created using discrete steps – are not present [157].

After a short 25 s ESD time, the surface shows splash features (Figure 41b) as a result of material transfer from the electrode. PFPs are no longer visible, likely due to re-melting of the substrate surface and coverage by material transferred from the electrode during ESD. A notable improvement to surface roughness is obtained by intermittent peening during ESD, and is clearly visible in the ESD+HP sample shown in Figure 41c. Although deposition time is also 25 s, splash features are not visible, and the uneven surface has been mostly flattened except for some regions that were too deep to reach with the peening tool.

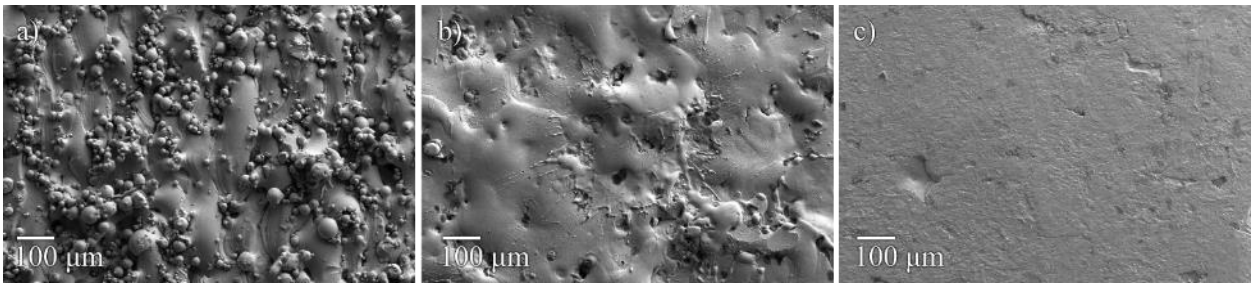

Figure 41. SEM images of the side surface of an as-built LPBF Hastelloy X part a) in the as-built condition, b) after ESD coating of Inconel 718 without peening, and c) after ESD coating of Inconel 718 with peening (ESD+HP)

The etched cross-section of an ESD+HP sample part after 75 s of ESD processing time is shown in Figure 42a. A closer look at the interface between the coating and substrate shows evidence of the Hastelloy X surface melting during ESD that removes PFPs from the surface. The cross-section in Figure 42b shows a Hastelloy X particle – distinguishable due to its equiaxed grain structure – that has been partially melted by the ESD process. The composition profile shown in Figure 42c identifies a 10 µm region of deposited material with lower Nb and greater Mo content than is expected from Inconel 718. Due to the spot size limitations of EDX measurements, the transition region in which Hastelloy X and Inconel 718 mix can be said to be 10 µm or less in size. Good metallurgical compatibility is expected based on the similar compositions of both materials, and the SEM/EDX analysis was unable to identify any intermetallics in the transition region.

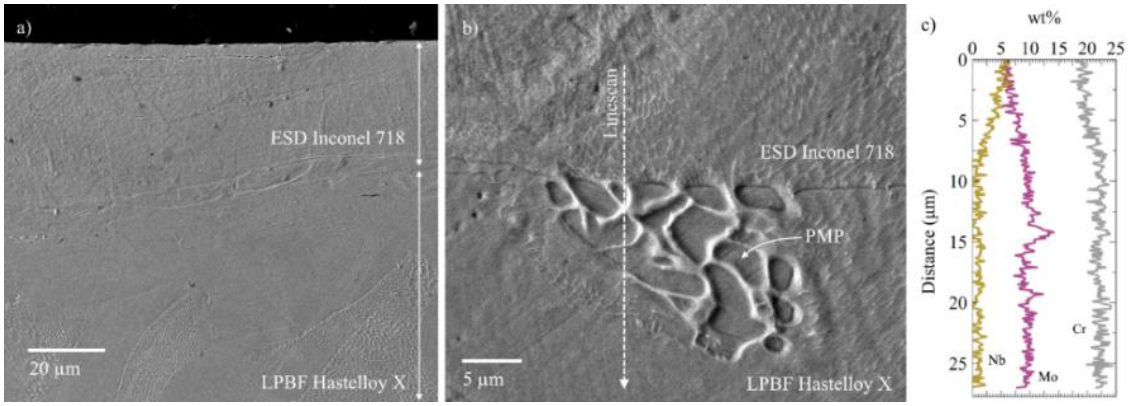

Figure 42. SEM images of a) an etched ESD+HP sample cross-section, b) partially melted particle visible at the coating/substrate interface, and c) EDX line-scan as indicated in (b).

As shown in Figure 43a, the short deposition times (25 s) decrease the short-range surface roughness from an initial S_a of 13.2 µm in the as-built samples to 6.7 µm in ESD processed samples, 6.5 µm in hammer peened (HP) samples, and 2.4 µm in ESD+HP samples (49%, 51%, and 82% decreases, respectively). The waviness also decreases from the as-built condition although to a lesser extent, from a W_a of 8.8 µm to 7.2 µm in ESD samples, 6.3 µm in hammer peened (HP) samples and 4.9 µm in ESD+HP samples (18%, 28%, and 45% decreases, respectively). The surface profiles shown in Figure 43c clearly show the effect of ESD on the surface roughness and waviness. The initial as-built surface has small localized peaks attributed to PFPs that are the major contributor to surface roughness, which are removed by the ESD process. Some longer-range waviness is present on the as-built surface and remains relatively unchanged after 25s of ESD processing. With longer deposition times and increased material deposition these wavy features grow preferentially while the roughness remains below the as-built condition.

The ability of peening to maintain a low surface waviness in conjunction with ESD can be attributed to the mechanism by which ESD occurs. As described in [26], irregular contact geometry strongly influences where the current discharge, spark discharge, and mass transfer occurs. Current discharge occurs when the electrode and substrate make contact, which on a wavy substrate surface is at the highest protruding region. When the contact is broken, spark discharge occurs, and molten droplets are transferred from the electrode to the substrate. Due to strong electrostatic forces, material is preferentially transferred to high points on the substrate surface [26,180]. When using ESD on a LPBF-made surface, current discharge initially occurs through clusters of protruding PFPs. The sinter necks that join these PFPs to the bulk part provide for a poor connection, resulting

in higher resistance, increased joule heating, and lower thermal diffusion. The result is an initial melting of these features (Figure 41b), which reduces the surface roughness even without the use of peening (seen in Figure 43a for short deposition times of 25 s). Further depositions produce elevated regions that further exacerbate the uneven transfer of material, forming islands as shown in Figure 43c. However, the use of intermittent peening during ESD slows the preferential deposition on elevated regions by flattening surface irregularities that appear at shorter intervals (roughness) and preventing preferential buildup on these irregularities from forming longer interval defects (waviness). This allows longer deposition times to have more uniform coatings.

The surface melting caused by ESD is critical to achieving a low surface roughness at short processing times; a comparison to samples which were only peened (HP) in Figure 43a shows that a combination of ESD and hammer peening is required to obtain low surface roughness, with either process being less effective when used alone. In conjunction with peening, an ESD process can be used to address both the need for reduced surface roughness and to change the surface properties of LPBF parts.

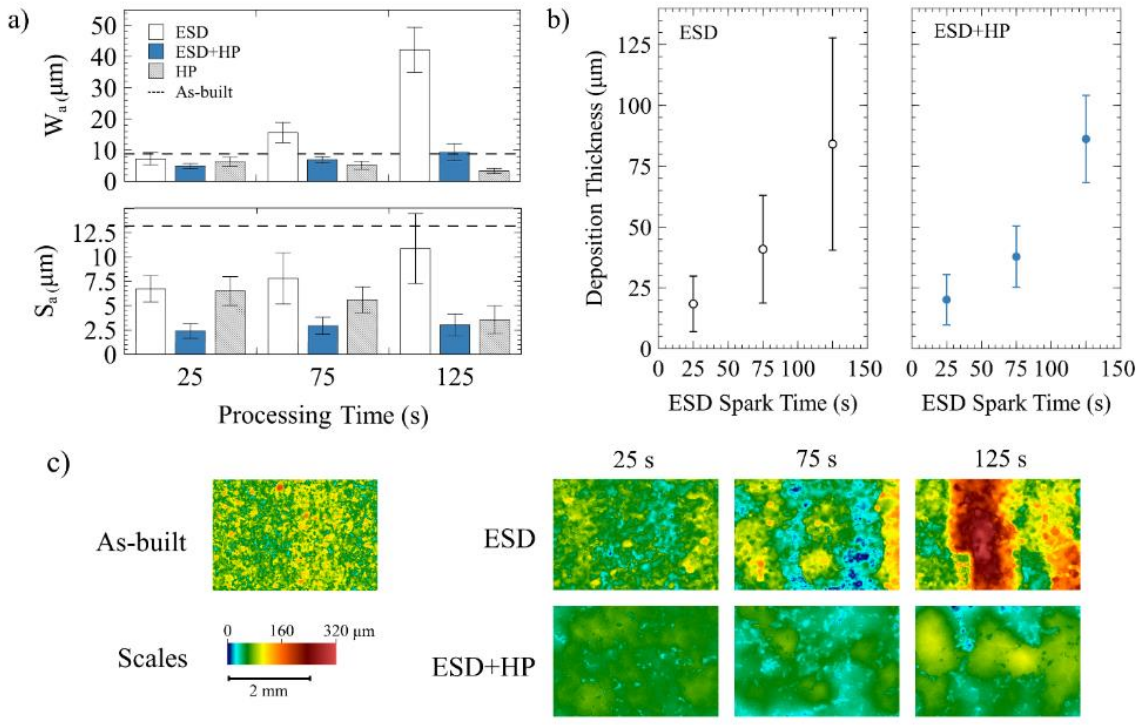

Figure 43. Comparison of a) surface roughness with standard deviations, b) coating thickness with standard deviations, and c) 2D surface roughness maps for ESD coatings made using various deposition times for as-built, ESD, and ESD+HP processed samples

The use of peening – and by extension the surface condition of the part being coated – in ESD+HP samples has no effect on the deposition thickness, although it does have an effect on the coating distribution by minimizing the surface waviness as described previously. The similarities in deposition thickness can be seen in Figure 43b, along with a clear difference in the standard deviation of peened (ESD+HP) and non-peened (ESD) samples. This unequal variance is quantified with the use of a Levene test [181], which shows in Table 18 a significant difference in the variance of the thicknesses between ESD+HP and ESD samples after 75s and 125s of ESD spark time. With the use of a Box-Cox transformation (λ=0.3) to meet the assumptions of a normal distribution and equal variance required for an ANOVA, the effect of peening, deposition time, and their interaction could be analyzed. Only deposition time was found to influence the deposition thickness (Table 19), with p-values for peening or the interaction between the two factors above 0.05. These results, which suggest that the use of peening has no effect on the average deposition thickness but does reduce variance in the deposition thickness at longer deposition times, indicates that the quantity of material transferred during ESD is not affected by the morphology of the substrate surface. Instead, only the distribution of the transferred material changes when peening is used.

Table 18. Levene test for average deposition thickness data in Figure 43b comparing ESD+HP and ESD samples

		ESD Spark Time		
Test	**Null Hypothesis (NH)**	**25s**	**75s**	**125s**
Levene	There is no difference in the variation of the deposition thickness	$p = 0.568$ Fail to reject NH	$p < 0.001$ Reject NH	$p < 0.001$ Reject NH

Table 19. Average deposition thickness ANOVA for the effect of peening and deposition time (Figure 43b)

	Sum of Squares	**df**	**Mean Square**	**F**	**p**
Peening	3.44	1	3.44	1.52	0.218
Time	1671.4	2	835.7	369.78	< .001
Peening × Time	5.49	2	2.75	1.22	0.297
Residuals	1299.5	575	2.26		

Inconel 718 coatings in ESD+HP samples show significantly higher hardness than LPBF Hastelloy X (471 HV vs. 283 HV), as well as the formation of a roughly 200 μm wide thermo-mechanically

affected zone (TMAZ) in the Hastelloy X near the deposition interface (Figure 44a). The effect of peening on hardness in both the deposition and TMAZ is made clear in Figure 44b, which shows a 47 HV decrease and significant reduction of the TMAZ when peening is not used (ESD samples). However, the deposition hardness without peening (424 HV) is still high when compared to Inconel 718 in the cast (225 HV), LPBF (325 HV) or electron beam melted (355 HV) condition [182]. The difference is attributed to a faster cooling rate that forms a finer subgrain microstructure (Figure 45a) and the presence of fine secondary phases (Figure 45b) that form during deposition [49,82]. Some secondary phases are identified using EDX as oxides, ranging from sub-micron sizes to several tens of microns. As seen clearly in Figure 45c, the oxides are rich in Al, Ti, and Nb, while also containing similar Cr and Mo content as the surrounding matrix. The following elements are arranged in terms of high to low standard free energies of formation for their oxides: Al, Ti, Nb, Cr, Fe, Mo, and Ni [183]. As such, the inclusion of Mo in the oxide is unusual and may be attributed to EDX peak overlap with Nb. The formation of these oxides is a common issue even in well-controlled high purity argon atmospheres [184,185], and may be assisted by the diffusion and segregation of elements at elevated temperatures that are favourable to oxidation [186].

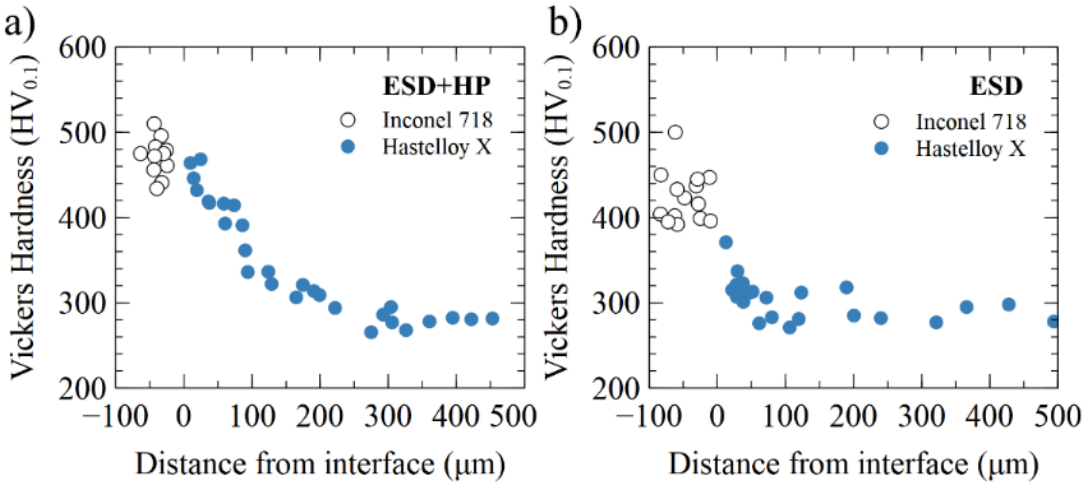

Figure 44. Microhardness values for Inconel 718 coating on Hastelloy X a) with peening (ESD+HP samples) and b) without peening (ESD samples)

The LPBF Hastelloy X substrate also exhibits a cellular subgrain microstructure (

Figure 46a) with approximately twice the primary dendrite spacing compared to the ESD processed Inconel 718 (0.8 μm vs. 0.4 μm). Oxides were also identified within as-built LPBF Hastelloy X (

Figure 46b), although with slight differences in composition compared to ESD processed Inconel 718. The oxides were determined to contain Al, Ti, and Cr, but no Mo or Nb were detected. The lack of Nb is expected since Hastelloy X does not contain much Nb, while the lack of Mo can be explained by the lower oxidation potential of Mo compared to Al, Ti and Cr, as well as no opportunity for EDX peak overlap with Nb.

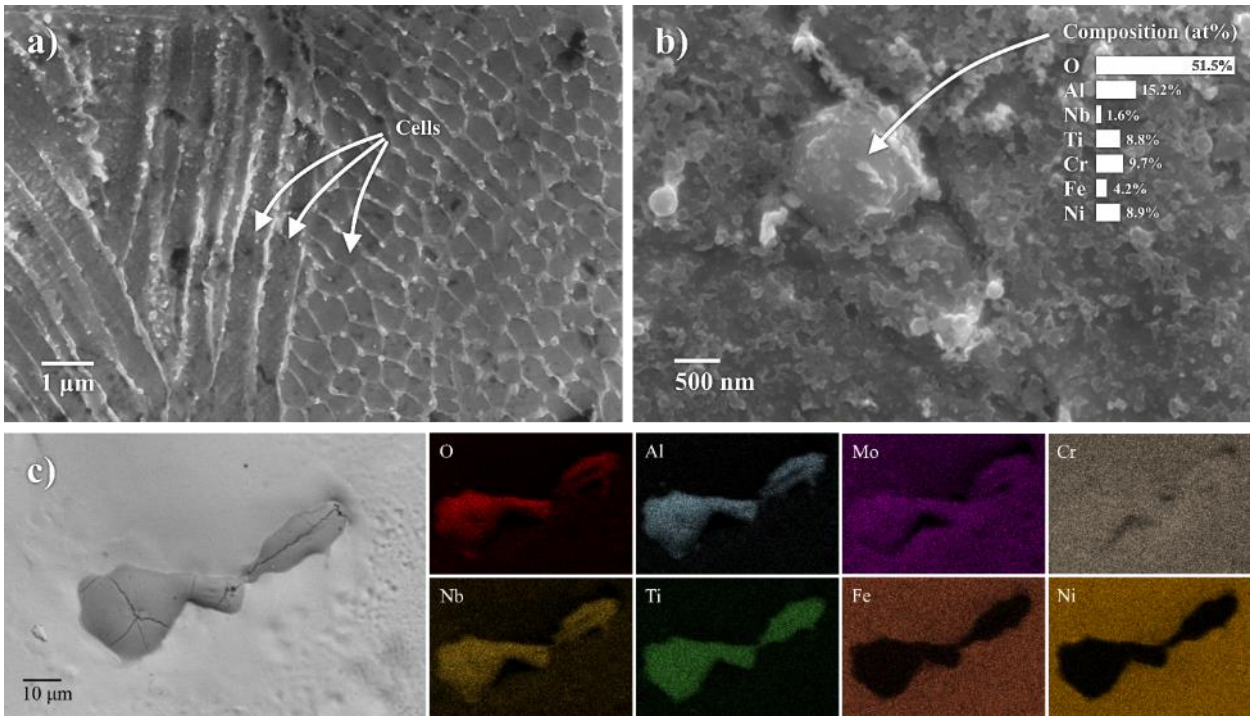

Figure 45. Microstructural features found within ESD Inconel 718 coating, including a) cellular dendritic subgrains, b) small spherical oxide with EDX composition, and c) large irregularly shaped oxide with corresponding EDX composition maps

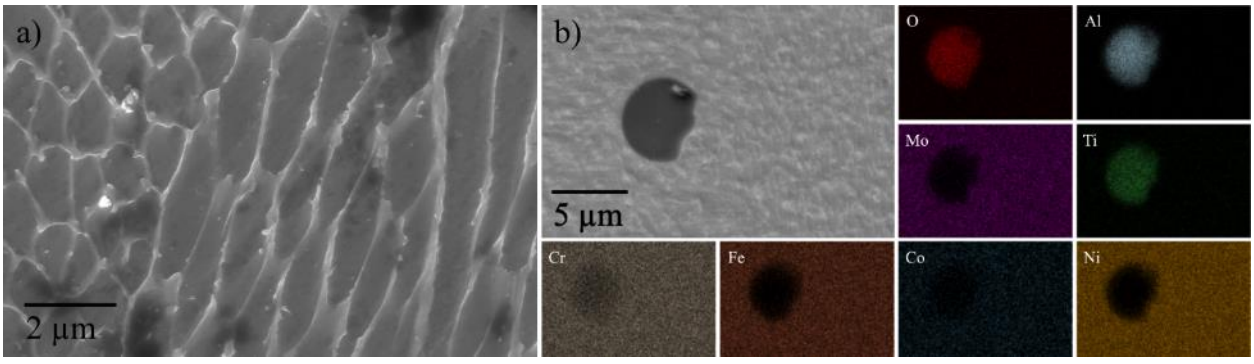

Figure 46. Microstructural features found within LPBF Hastelloy X, including a) cellular subgrains and b) irregularly shaped oxide with corresponding EDX composition maps

6.3.2 Heat treatment of ESD post-processed parts

Three heat treatments are investigated to determine their effect on microstructure and hardness of ESD+HP samples. The first is a direct aging heat treatment that aims to precipitate the strengthening γ" phase in the deposited Inconel 718 coating. The result of this treatment on microhardness is shown in Figure 47a. The second is an annealing heat treatment that aims to solutionize interdendritic phases, recrystalize the microstructure, and remove residual stresses in the Inconel 718 coating. The result of this treatment on microhardness is shown in Figure 47b. The third heat treatment is a combination of the prior two; a solution annealing step is performed, followed by an aging heat treatment. The result is shown in Figure 47c.

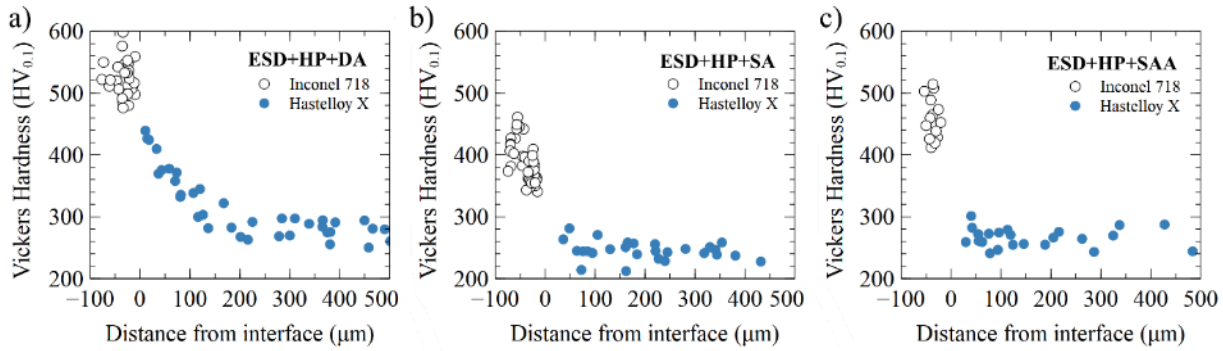

Figure 47. Microhardness values for peened Inconel 718 coating on Hastelloy X after a) direct aging (ESD+HP+DA samples), b) solution annealing (ESD+HP+SA), and c) solution annealing and aging (ESD+HP+SAA)

Similar to the previously reported effect of direct aging on ESD processed Inconel 718 [137], ESD+HP+DA samples show an increased Inconel 718 hardness of 523 HV (from 471 HV) while having no significant effect on the TMAZ or Hastelloy X substrate. Aging of Inconel 718 results in the formation of carbides (Figure 48a,b) and the formation of γ" and γ' precipitates (Figure 48c) with Ni_3Nb and $Ni_3(Al,Ti)$ compositions, respectively. Since these samples are direct aged without a solutionizing step, the interdendritic eutectic and potential Laves phase that forms during solidification is retained (Figure 48d). Without sufficient quantities of Nb, Al, or Ti in Hastelloy X, the typical γ" and γ' precipitates that contribute to an increase in strength and hardness after aging in other Ni-superalloys do not form. As such, only the deposited Inconel 718 is expected to noticeably benefit from the direct aging heat treatment.

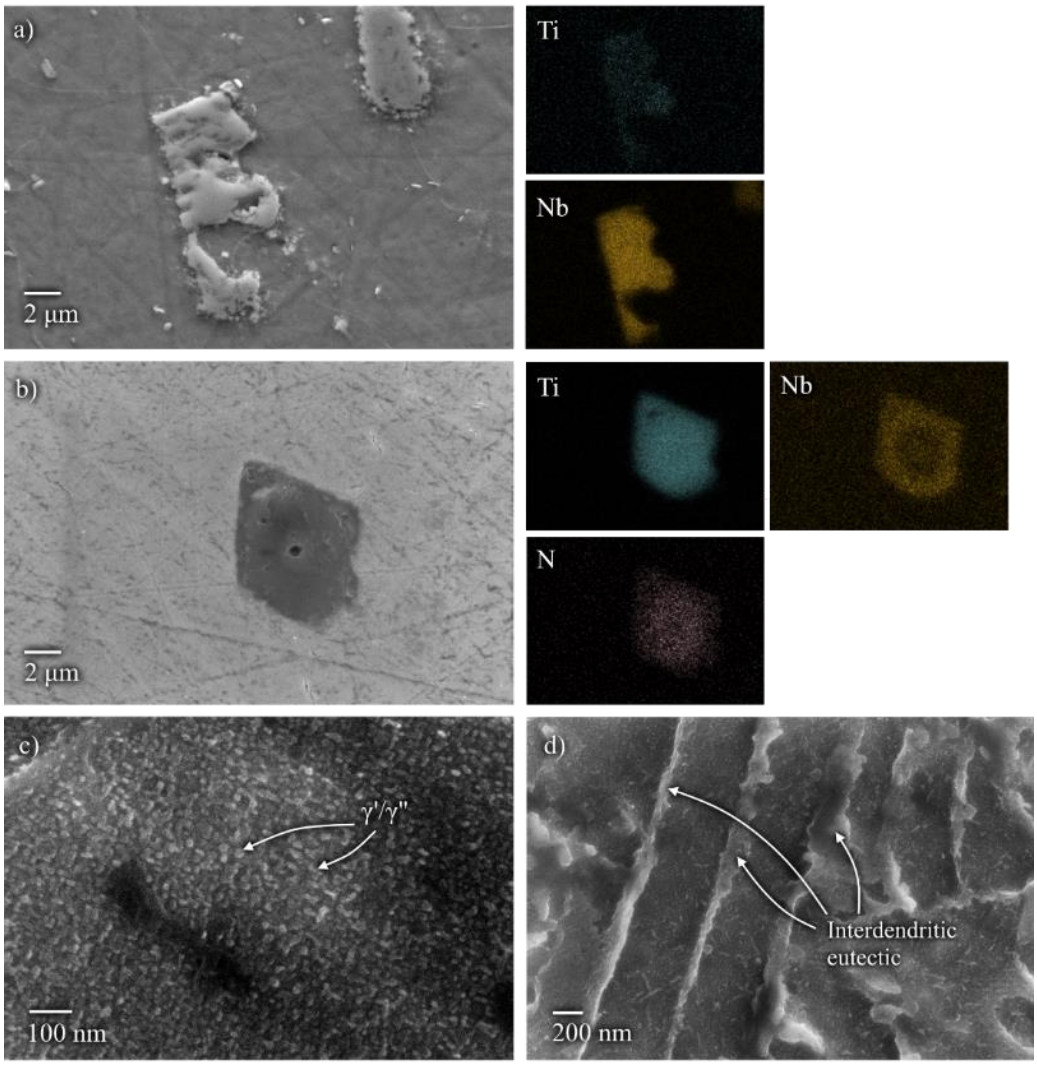

Figure 48. SEM images of phases obtained after aging Inconel 718, including a) (Nb,Ti)C, b) (Ti,Nb)CN, c) γ" and γ' and d) retained interdendritic eutectic after direct aging that formed during solidification

The use of a solution annealing heat treatment in ESD+HP+SA samples reduces hardness in the deposition (from 471 HV to 390 HV) and in the TMAZ (Figure 47b). This is attributed to the microstructural changes in the coating area after the solutionizing heat-treatment. To better characterize these changes, EBSD analysis has been performed. In the ESD+HP sample coatings, the inability to obtain clear EBSD results (Figure 49a) is due to severe distortion in the highly deformed coating region. Literature has shown that more advanced indexing techniques are required to resolve the low quality Kikuchi patterns obtained in this region [187]. The inability to index ESD coatings also occurred in ESD sample coatings without peening, and therefore cannot

be attributed solely to stresses introduced by peening. Some residual stresses can be attributed to two additional mechanisms: quenching of transferred material upon contact with a substrate that constrains its thermal contraction, and differences in coefficients of thermal expansion leading to thermal stress [188]. The very rapid cooling experienced during ESD makes the first mechanism a likely source of residual stresses, while the similar material composition between the Inconel 718 coating and Hastelloy X substrate suggests a smaller contribution from differing coefficients of thermal expansion. The resulting distorted crystal structure causes Kikuchi bands to appear diffuse [189], making EBSD analysis of grain orientation difficult. Shrinkage also affects the substrate as seen in the Kernel average misorientation (KAM) maps, which show that the local misorientation is increasing from the substrate core to the substrate/coating interface (Figure 49b). The higher misorientation near the interface is attributed to the combination of peening and ESD, during which the first mechanism – shrinkage of the coating during cooling – and peening both apply a stress on the substrate and distort the crystal structure of the grains. This also corresponds to the higher hardness in the Hastelloy X substrate near the interface.

After solution annealing, the dislocation annihilation and rearrangement that occurs during recovery allows for proper indexing of the coating (Figure 49c). A narrow misoriented region with a columnar grain morphology (Figure 49d) is found in the coating surrounded by equiaxed ultrafine grains. This region of high misorientation is related to the pre-existing columnar grains which form due to epitaxial grain growth during rapid solidification. However, the misorientation-free regions in both the coating and TMAZ (Figure 49d) reveals that static recrystallization occurs, with much finer recrystallized grains in the coating than in the substrate. With high dislocation density being a driving force for recrystallization, the difference in final grain size can be attributed to the higher misorientation originally present in the coating that increases the nucleation rate during recrystallization. As such, even after an annealing heat treatment, the deposition hardness remains above that of cast, LPBF, and EBM Inconel 718. In addition to the ultrafine grain size, some secondary phases such as oxides are not solutionized during the heat treatment and continue to contribute to the increased hardness.

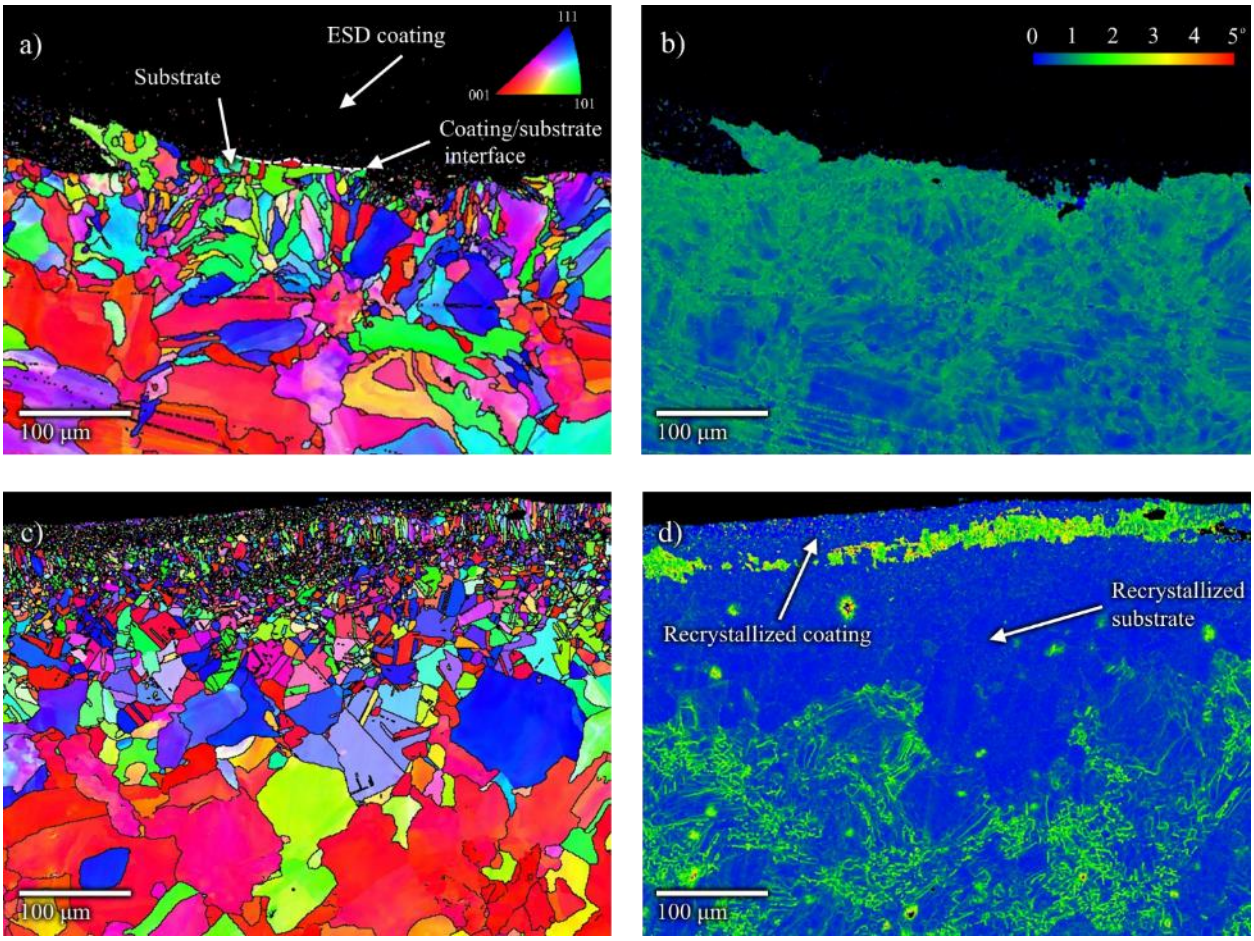

Figure 49. EBSD maps for a) as-deposited coating and substrate, b) KAM map of the as-deposited sample, c) annealed and aged (ESD+HP+SAA) sample, and d) KAM map of the annealed and aged (ESD+HP+SAA) sample

At the conclusion of an aging heat treatment performed on solution annealed samples (ESD+HP+SAA), the hardness of the deposition increases to 460 HV. The 70 HV increase in the Inconel 718 hardness when comparing the annealed coating to the annealed and aged condition is attributed to the precipitation of the γ" phase. However, since residual stresses and some secondary phases have been removed during annealing, the deposition is 63 HV softer in the annealed and aged state when compared to the direct aged state.

A comparison of time-temperature-transition diagrams show that Inconel 718 is more sensitive than Hastelloy X to an aging heat treatment at 720 °C, with Inconel 718 forming the beneficial γ" phase [190]. This explains the significantly greater effect of aging on the hardness and strength of Inconel 718. Due to minimal precipitation strengthening in Hastelloy X, the hardness outside of

the TMAZ does not differ significantly after heat treatments. However, the annealing treatment may alleviate some residual stresses that occur during LPBF, which may account for the 38 HV drop between the as-built and annealed condition in Figure 47b. Both materials also form carbide phases rapidly at 720 °C, with Hastelloy X forming M_6C and $M_{23}C_6$ carbides [191]. These often have a negative influence on ductility in Hastelloy X, in addition to the negative influence on ductility from the sigma phase reported to form between 650 °C and 760 °C [192].

6.4 Fatigue Response

The room temperature low and high cycle fatigue responses (LCF and HCF, respectively) of as-built LPBF Hastelloy X are compared in Figure 50 to post-processed specimens in the hammer peened (HP), ESD and hammer peened (ESD+HP), and ESD and hammer peened with a direct aging heat treatment (ESD+HP+DA) conditions. Two stress levels, 550 MPa for LCF and 350 MPa for HCF, were chosen for comparison, and three samples per each condition were tested at each stress level. The best performing condition (ESD+HP) showed a fatigue life improvement from 3 times to two orders of magnitude depending on the stress level. Most ESD+HP samples tested in LCF conditions showed a fatigue life improvement of up to 5 times, whereas those tested in HCF conditions experienced runout ($> 10^7$ cycles) for a minimum fatigue life improvement of 50 times. However, one ESD+HP sample at each test condition failed sooner, showing only 3- and 10-times improvement (for LCF and HCF, respectively) over the as-built condition. Early fatigue failure is attributed to sub-surface lack of fusion defects, while failure of the better performing samples occurred in the Inconel 718 coating due to surface defects during ESD. Further failure analysis is provided in Figure 51. Other post-processed conditions achieved smaller improvements in fatigue life over the as-built condition. The use of hammer peening alone (HP samples) provided a 1.7- and 2.4-times improvement at LCF and HCF conditions, respectively, while the ESD+HP+DA samples showed a 2- and 10-times improvement, respectively.

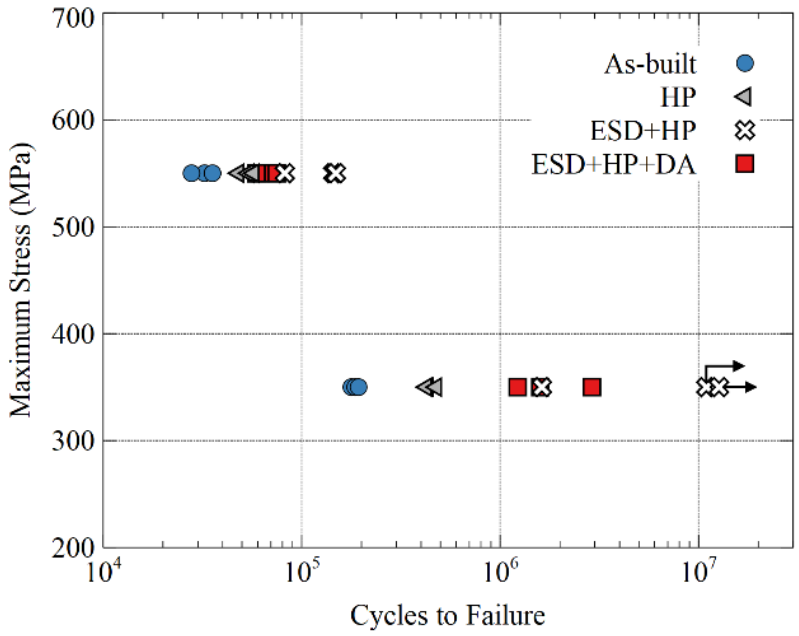

Figure 50. Results of fatigue testing as-built and post-processed specimens in LCF and HCF conditions. Arrows indicate samples with interrupted tests without failures up to 10^7 (runout).

Even with defects arising from LPBF and ESD, the fatigue life of samples in the ESD+HP condition are significantly improved. A comparison with the recent literature shows that the proposed ESD+HP post-processing is more effective in increasing the fatigue performance than a combined polishing (to S_a of 0.33 μm) and hot isostatic pressing (HIP) technique, which could only achieve up to 9×10^5 cycles at a maximum stress of 350 MPa [193]. The significant improvement obtained by ESD+HP over the as-built or polished and HIPed condition reported in the literature can be attributed to a combination of factors including the reduction in surface roughness, the higher strength of the as-built Hastelloy X substrate and Inconel 718 coating, and residual stresses introduced as a result of hammer peening and quenching stress during ESD.

ESD parameters for the ESD+HP samples were chosen specifically to reduce the as-built surface roughness of 13.2 μm to a post-processed S_a of 2.4 μm, in accordance with the results presented earlier (Figure 43a). This reduction in surface roughness has the effect of reducing the size of notch-like features at the surface, which often act as stress risers and crack initiation sites. The influence of roughness is reflected in calculations of the endurance limit stress ($\Delta\sigma_D$), which is effectively the maximum stress below which the crack propagation of a defect does not occur. Equation (32) is used while implementing a linear fracture mechanics approach [194]:

$$\Delta\sigma_D = \frac{\Delta K_{th}}{f K_t \sqrt{\pi a}} \qquad (32)$$

where f is a crack geometry dependent factor (1.122 for surface cracks), ΔK_{th} is the threshold stress intensity for crack propagation, a is the crack length and K_t is a stress concentration factor dependent on surface roughness. This dependence for a sample under a tensile stress state is shown in Equation (33) [195]:

$$K_t = 1 + 2\left(\frac{S_a}{\rho}\right)\left(\frac{S_y}{S_z}\right) \qquad (33)$$

where S_a is the arithmetic mean height, ρ is the valley profile radius, S_y is the maximum absolute peak to valley height, and S_z is the 10-point height. The description of K_t in Equation (33) incorporates several roughness and geometrical parameters that describe the influence of surface roughness on crack propagation from a surface notch, which is effective at predicting the fatigue life of additive manufactured parts [196]. Values of these roughness parameters for an ESD post-processed surface and original as-built surface are shown in Table 20. The use of these parameters in Equation (33) suggests a decrease in the stress concentration factor (K_t) after ESD post-processing of 2.9 times, resulting in a predicted endurance limit stress 2.9 times greater than in the as-built condition according to Equation (32). With an actual endurance limit stress of 149 MPa for the as-built samples [197], the runout obtained with ESD+HP post-processed samples at 350 MPa suggests that an endurance limit stress at least 2.35 times greater was achieved.

Table 20. Surface parameters and stress concentration factor determined with Eqn. (33)

	As-built	**ESD + HP**
S_a [μm]	13.2	2.4
S_y [μm]	152.48	90.54
S_z [μm]	73.81	34.97
ρ [μm]	8.98	8.63
K_t	7.07	2.44

Since a combination of ESD and hammer peening demonstrated a lower surface roughness than hammer peening alone, a greater fatigue life for ESD+HP samples when compared to HP samples is justified. This also suggests that the compressive residual stresses introduced by the peening process, which have been shown to delay crack initiation and propagation originating at the surface [198], is not likely a major contributor to the improved fatigue life. The presence of an ESD

processed Inconel 718 coating in the ESD+HP samples is expected to account for some of the difference in performance. One contributor to the improved fatigue life may be attributed to the introduction of residual stresses from the quenching of deposited material during ESD. Additionally, the influence of Inconel 718's better mechanical properties would be reflected in the value of ΔK_{th} in Equation (32), since the threshold stress intensity factor for propagation varies depending on the material and microstructure. One benefit to ESD processed Inconel 718 is the small grain size, which has been shown to improve fatigue life by increasing boundary tortuosity and increasing the crack growth resistance in Ni-superalloys [199,200].

The lack of heat treatment in the ESD+HP condition was also found to be beneficial, since the Hastelloy X substrate and Inconel 718 coating retain both their high hardness and residual stresses introduced during peening and ESD/LPBF. High temperature heat treatments were found to be detrimental to fatigue life in literature, which caused softening of Hastelloy X [193]. However, more modest heat treatment temperatures were also found detrimental in this study. A direct aging heat treatment in ESD+HP+DA samples introduced γ" precipitates to increase strength in the Inconel 718 coating (Figure 47a), yet still resulted in a smaller fatigue life improvement over the as-built condition when compared to ESD+HP samples (Figure 50). Since temperatures and heat treatment times are too low to relieve residual stresses from the LPBF, ESD, or hammer peening processes (as concluded from Figure 47a), one potential cause is the formation of detrimental grain boundary phases in the Hastelloy X. These have been found to reduce room-temperature ductility in the temperature range used for direct aging in this study [192]. However, these precipitates are less brittle at elevated temperatures and were found to not influence the typical service temperature properties of Hastelloy X [192]. Although further studies are required to identify the influence of heat treatment on the microstructure and fatigue properties of LPBF-made Hastelloy X, the decrease in fatigue performance between ESD+HP and ESD+HP+DA samples indicates that the room-temperature fatigue performance is highly sensitive to heat treatment.

Fracture surface analysis was performed on the only ESD+HP sample that failed at an HCF stress level of 350 MPa. Several sub-surface lack of fusion defects like the one shown in Figure 51a were identified near the surface of this sample, with failure appearing to originate from these defects. The close proximity of these defects to the surface of the part is likely responsible for the premature failure, with previous studies having shown that defects nearer the surface result in a lower fatigue

life [10]. An analysis of an as-built sample tested at a LCF stress level of 550 MPa shows that failure originated from roughness-related defects on the part surface, as can be seen in Figure 51b. This also remains true of ESD+HP samples tested at 550 MPa, with Figure 51c showing that cracking originates at the part surface. This alleviated initial concerns that brittle phases in the as-deposited Inconel 718 would encourage crack initiation and propagation [122]. A previous study identified a low fracture toughness along the interdendritic regions and droplet boundaries found in ESD processed Inconel 718 subjected to tensile testing [102]. However, the brittle interdendritic Laves phase that forms in Inconel 718 does not fracture at the low stresses investigated within this study, and has instead been shown to improve fatigue strength by hindering crack propagation [45]. Another concern is the large oxide phases identified within the Inconel 718 coating (Figure 45c), which show cracking prior to fatigue testing and could be considered potential crack initiation sources. No evidence of this was observed, with none of the observed oxides near the surface (Figure 51c) acting as crack initiation sites.

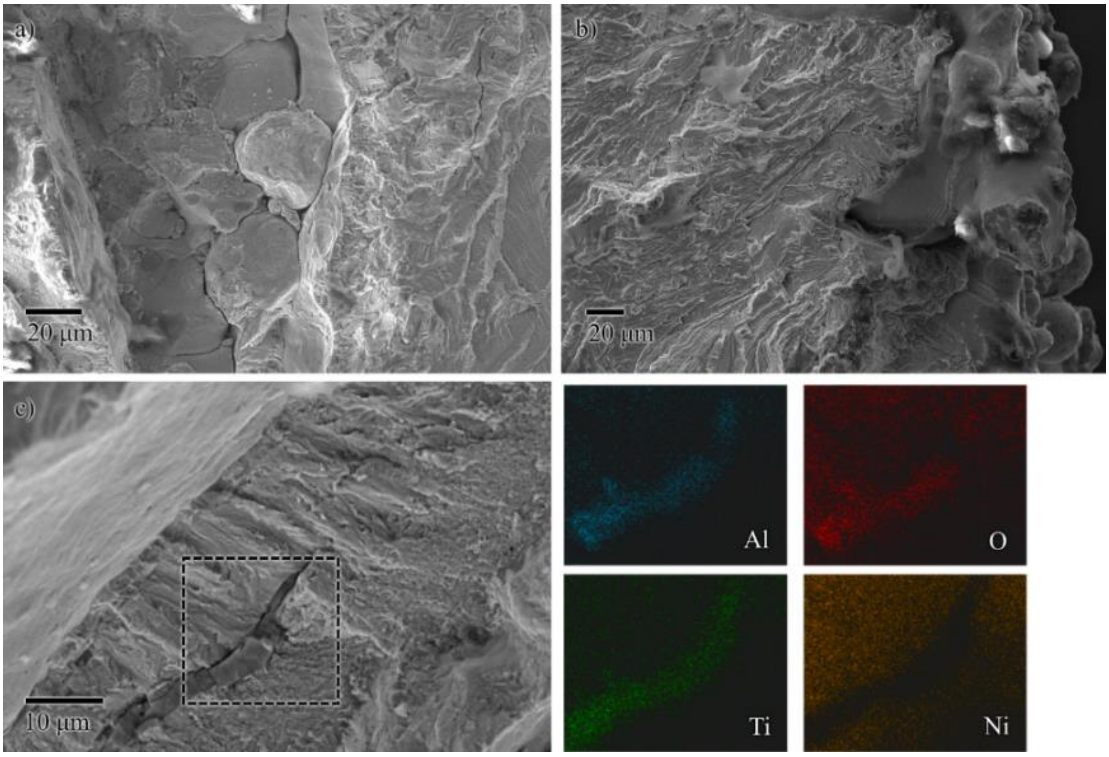

Figure 51. Fracture initiation sites in a) ESD+HP sample at 350 MPa maximum stress level, b) as-built sample at 550 MPa maximum stress level, c) ESD+HP sample at 550 MPa maximum stress level with EDX map of oxide particle

6.5 Conclusion

The surface treatment of laser powder bed fusion (LPBF) made Hastelloy X samples was performed using a combined electrospark deposition (ESD) and hammer peening technique. This post-processing method addresses the surface roughness and the surface property issues of LPBF through the deposition of an Inconel 718 coating.

- A surface roughness (R_a) reduction of 82 %, surface hardness increase of 85 %, and Inconel 718 coating of 20 μm was obtained with an ESD spark time of 25 s in a 1 cm^2 area and hammer peening. Although peening reduced surface roughness, increased the hardness of the deposited coating, and increased the size of the thermo-mechanically affected zone (TMAZ), it was not found to influence the average coating thickness.
- The use of typical Inconel 718 heat treatments had limited effect on the LPBF additive manufactured Hastelloy X substrate hardness while significantly altering the microstructure and hardness of the Inconel 718 coating. Direct aged samples showed an increase in hardness alongside a precipitation of the γ" and γ' phases. An annealing and aging heat treatment partially recrystallized the Inconel 718 grain structure and eliminated the TMAZ prior to forming the strengthening γ" and γ' phases.
- The use of an ESD Inconel 718 coating and hammer peening on LPBF additive manufactured Hastelloy X resulted in a greater than 50 times improvement in cycles to failure (reaching > 10^7 cycles) at a stress of 350 MPa and an up to 5 times improvement in cycles to failure (to 1.5×10^5 cycles) at a stress of 550 MPa. The improvement in the endurance limit can be primarily attributed to a reduction in surface roughness and better properties of the coating material.

Chapter 7. Summary

7.1 Conclusion

Although each chapter provides a conclusion specific to the chapter's respective study, this conclusion aims to present a broader summary in the context of the larger objective: the development of an ESD process for the repair and coating of heat-sensitive parts. Three studies were performed to determine the influence of subgrain microstructure and the role of boundaries in the mechanical properties and phase transformations of ESD-processed Inconel 718. These results provide the understanding needed to explain the behaviour of ESD-processed materials and tailor process parameters for applications that require high-performance repairs and coatings. The methods used and the main findings are summarized below:

- Thinner deposition splats are found to cool more quickly, resulting in finer subgrain features. The relationship between deposition splat thickness and subgrain diameter is well fit by an exponential relationship based on the coarsening equation and was extended to the Hall-Petch relationship. The resulting relationship appropriately fits experimental data relating the deposition splat thickness and microhardness. Thinner deposition splats with finer subgrains have higher microhardness, such that depositions performed with lower energy input process parameters, in which smaller droplet volumes are transferred, will exhibit better mechanical properties.
- Evaluations of tensile strength in ESD repaired cavities showed that process parameters which resulted in thinner deposition splats and higher microhardness also demonstrated higher yield strength. Thinner splats and smaller subgrains introduce a greater number of boundaries in the deposited material, which are known to resist the movement of dislocations and increase yield strength. From these studies, coatings and repairs performed with lower energy parameters result in increased coating hardness and improved tensile properties than those performed with higher energy parameters. Therefore, lower energy parameters are recommended when a lower deposition rate is acceptable.
- A crack propagation study was performed to determine the reason for the lower ultimate strength in ESD repaired cavities compared to the base metal. Unique step-like facets were observed along the fracture surface of repaired cavities, caused by an alternating crack path

direction along splat and subgrain boundaries. Stress intensity factors were used to determine the relative fracture toughness of the two boundaries, based on the angle of crack propagation relative to the applied tensile load. Using this method, splat boundaries were determined to have 30% of the fracture toughness of subgrain boundaries. Fracture toughness at the subgrain boundaries is negatively affected due to micro-segregation and brittle phases, while splat boundaries are assumed to be affected by dislocation density and impurities.

- Micro-segregation of Nb at subgrain boundaries during solidification provides a greater number of nucleation sites for the δ phase in an ESD-processed alloy 718 when compared to a homogenized alloy 718. A nucleation site model which allows for a relative comparison of nucleation sites is able to explain the greater number of proportionally smaller δ precipitates forming in the ESD-processed alloy 718 when exposed to elevated temperatures. Results show that the formation of the δ phase at 700 °C and above is detrimental to strength since it is accompanied by dissolution of the γ" strengthening phase.

The results from the previous studies guided the application of ESD as a technique to address poor surface conditions and low fatigue life in LPBF additive manufactured parts. LPBF-made Hastelloy X parts are treated with an ESD processed Inconel 718 coating and a hammer peening process. This study demonstrates ESD as a viable technique for the coating of additive manufactured parts, capable of selectively enhancing areas susceptible to crack initiation and fatigue failure. The smaller heat input associated with the ESD process should also allow for the application of this technique to the small features possible with an LPBF process.

- The deposition mechanism during ESD, where current discharge occurs through protrusions on the surface, has the benefit of melting those protrusions. This results in an initial decrease in surface roughness. Intermittent hammer peening is shown to reduce the preferential buildup of material that develops during longer ESD processing times. The combination of ESD and hammer peening obtains lower surface roughness (82 %) than their individual use.
- Several heat treatments performed on ESD coated samples identified direct aging as the most beneficial heat treatment process for obtaining high hardness Inconel 718 coatings.

A solution annealing heat treatment was found to induce recrystallization in the Inconel 718 coating, while eliminating the micro-segregation present at subgrain boundaries.

- Experimental measurements of the surface roughness in as-built LPBF-made Hastelloy X parts and those post-processed with both ESD Inconel 718 coating and hammer peening provided the data needed to calculate the endurance limit stress based on threshold stress intensities for crack propagation. The reduction in surface roughness due to post-processing was predicted to result in a 2.9-times increase in the endurance limit stress. The improvement at a maximum stress level of 350 MPa was significant, with a 50-times increase in fatigue life and two of the three post-processed samples experiencing runout. A comparison of these samples to those only post-processed with hammer peening, which showed an improvement in fatigue life of 2.4-times, shows that the significant improvement in fatigue life cannot solely be attributed to compressive stresses introduced by hammer peening.

7.2 Outlook

This thesis has two primary objectives, both of which lead to future research directions and applications in industry:

- The influence of microstructure on room temperature hardness, tensile strength, and fatigue life has been thoroughly studied in this thesis. However, these alloys are also often used at both cryogenic and elevated temperatures. Expanding these studies to consider the influence of temperature on mechanical properties with fine subgrain structures, splat boundaries, and delta phase formation at subgrains would be beneficial for targeting specific applications.
- The notable improvement in fatigue life possible with the use of ESD surface post-processing is expected to be a significant benefit to industry. The comparatively small deposition rate and geometrical limitations associated with ESD are expected to limit the application of this technique to externally accessible surfaces and critical regions of additive manufactured parts. An ideal application envisions the use of finite element stress analysis to locate regions in additive manufactured parts that are susceptible to fatigue failure, and the application of ESD coatings in those regions.

- One of the included studies aimed to improve fatigue life in a Hastelloy X part made using LPBF additive manufacturing by depositing an Inconel 718 coating using ESD. The better mechanical properties of Inconel 718 were expected to contribute to the improved performance, however achieving similar improvement in fatigue performance using other alloys as the coating (similar or dissimilar to the substrate) would be of interest. Specifically of interest for high temperature applications are oxidation resistant alloys (aluminides or NiCoCrAlY), which are already used in industry and have already been demonstrated processable using ESD [17]. Additional research may also consider extending the ESD surface post-processing technique to other additive manufacturing processes.

7.3 Research Contributions

The following research contributions were made throughout the course of this thesis work.

7.3.1 Articles Published/Accepted in Peer-reviewed Journals

1. **P.D. Enrique**, A. Keshavarzkermani, N.Y. Zhou, Effect of Micro-segregation on High Temperature Microstructure Evolution in Rapid Solidification Processed Nb-rich Ni-superalloys, Adv. Eng. Mater. (2021). https://doi.org/10.1002/adem.202001396.
2. A. Keshavarzkermani, R. Esmaeilizadeh, **P.D. Enrique**, H. Asgari, N.Y. Zhou, A. Bonakdar, E. Toyserkani, Static recrystallization impact on grain structure and mechanical properties of heattreated Hastelloy X produced via laser powder-bed fusion, Mater. Charact. (2021). (Accepted)
3. **P.D. Enrique**, S. Peterkin, N.Y. Zhou, Parametric study of Automated Electrospark Deposition for Ni-superalloys, Weld. J. (2021). (Accepted)
4. M.S. Khan, **P.D. Enrique**, G. Song, M.I.S.T. Faria, Y. Zhou, Laser-assisted wire cladding using a retrofitted laser welding system, Surf. Eng. (2020) 1–8. https://doi.org/10.1080/02670844.2020.1820266.
5. **P.D. Enrique**, A. Keshavarzkermani, R. Esmaeilizadeh, S. Peterkin, H. Jahed, E. Toyserkani, N.Y. Zhou, Enhancing fatigue life of additive manufactured parts with electrospark deposition post-processing, Addit. Manuf. 36 (2020) 101526. https://doi.org/10.1016/j.addma.2020.101526.

6. **P.D. Enrique**, C. Li, C. DiGiovanni, S. Peterkin, N.Y. Zhou, Electrospark deposition interlayers for dissimilar resistance welding of steel to aluminum, Manuf. Lett. 24 (2020) 123–126. https://doi.org/10.1016/j.mfglet.2020.04.009.
7. **P.D. Enrique**, E. Marzbanrad, Y. Mahmoodkhani, A. Keshavarzkermani, H. Al Momani, E. Toyserkani, N.Y. Zhou, Design of binder jet additive manufactured co-continuous ceramic-reinforced metal matrix composites, J. Mater. Sci. Technol. 49 (2020) 81–90. https://doi.org/10.1016/j.jmst.2020.01.053.
8. **P.D. Enrique**, H. Al Momani, C. DiGiovanni, Z. Jiao, K.R. Chan, N.Y. Zhou, Evaluation of Electrode Degradation and Projection Weld Strength in the Joining of Steel Nuts to Galvanized Advanced High Strength Steel, J. Manuf. Sci. Eng. 141 (2019). https://doi.org/10.1115/1.4044253.
9. A. Keshavarzkermani, R. Esmaeilizadeh, U. Ali, **P.D. Enrique**, Y. Mahmoodkhani, N.Y. Zhou, A. Bonakdar, E. Toyserkani, Controlling mechanical properties of additively manufactured hastelloy X by altering solidification pattern during laser powder-bed fusion, Mater. Sci. Eng. A. 762 (2019) 138081. https://doi.org/10.1016/j.msea.2019.138081.
10. **P.D. Enrique**, E. Marzbanrad, Y. Mahmoodkhani, Z. Jiao, E. Toyserkani, N.Y. Zhou, Surface modification of binder-jet additive manufactured Inconel 625 via electrospark deposition, Surf. Coatings Technol. 362 (2019) 141–149. https://doi.org/10.1016/j.surfcoat.2019.01.108.
11. A. Keshavarzkermani, E. Marzbanrad, R. Esmaeilizadeh, Y. Mahmoodkhani, U. Ali, **P.D. Enrique**, N.Y. Zhou, A. Bonakdar, E. Toyserkani, An investigation into the effect of process parameters on melt pool geometry, cell spacing, and grain refinement during laser powder bed fusion, Opt. Laser Technol. 116 (2019) 83–91. https://doi.org/10.1016/j.optlastec.2019.03.012.
12. **P.D. Enrique**, Z. Jiao, N.Y. Zhou, Effect of Direct Aging on Heat-Affected Zone and Tensile Properties of Electrospark-Deposited Alloy 718, Metall. Mater. Trans. A. 50 (2019) 285–294. https://doi.org/10.1007/s11661-018-4997-1.
13. **P.D. Enrique**, Y. Mahmoodkhani, E. Marzbanrad, E. Toyserkani, N.Y. Zhou, In situ formation of metal matrix composites using binder jet additive manufacturing (3D printing), Mater. Lett. 232 (2018) 179–182. https://doi.org/10.1016/j.matlet.2018.08.117.

14. R. Liang, O.M. Schneider, N. Lun, **P.D. Enrique**, D.C. Saha, L.C.M. Li Chun Fong, I. Jaciw-Zurakowsky, M.R. Servos, P. Peng, N.Y. Zhou, Concurrent photocatalytic degradation of organic contaminants and photocathodic protection of steel Ag–TiO2 composites, Materialia. 3 (2018) 212–217. https://doi.org/10.1016/j.mtla.2018.08.033.
15. **P.D. Enrique**, Z. Jiao, N.Y. Zhou, E. Toyserkani, Effect of microstructure on tensile properties of electrospark deposition repaired Ni-superalloy, Mater. Sci. Eng. A. 729 (2018) 268–275. https://doi.org/10.1016/j.msea.2018.05.049.
16. **P.D. Enrique**, Z. Jiao, N.Y. Zhou, E. Toyserkani, Dendritic coarsening model for rapid solidification of Ni-superalloy via electrospark deposition, J. Mater. Process. Technol. 258 (2018) 138–143. https://doi.org/10.1016/j.jmatprotec.2018.03.023.

7.3.2 Articles to be Submitted to Peer-reviewed Journals

1. **P.D. Enrique**, C. DiGiovanni, N. Mao, R. Liang, S. Peterkin, N.Y. Zhou, Resistance is not futile: The use of projections for resistance joining of metal additive manufactured parts.

7.3.3 Presentations, Posters, and Magazines

1. **P.D. Enrique**, N. Scotchmer, E. Toyserkani, N.Y. Zhou, Repair of additive manufactured products by electro-spark deposition, Manufacturing and Materials Joining Innovation Center, Columbus, Ohio, 2021 (Presentation)
2. **P.D. Enrique**, Z. Jiao, S. Peterkin, N.Y. Zhou, Development of electro spark deposition technology for Ni-superalloy repair, WELD 2020 (Magazine)
3. **P.D. Enrique**, N.Y. Zhou, Repair of Inconel 718 with electrospark deposition, presented at the 16th International Forum on Intelligent Manufacturing Technology, Beijing, China, 2019 (Presentation)
4. **P.D. Enrique**, E. Toyserkani, N.Y. Zhou, Binder-jet additive manufactured metal matrix composites made by reactive sintering post processing, NSERC Network for Holistic Innovation in Additive Manufacturing, Vancouver, Canada, 2019 (Poster)
5. A. Martinez, S. Patel, **P.D. Enrique**, M. Vlasea, Topology optimized wind turbine blades using sustainable biomaterials, RAPID + TCT, Detroit, United States, 2019 (Poster)

6. **P.D. Enrique**, Z. Jiao, N. Scotchmer, E. Toyserkani, N.Y. Zhou, Low energy welding for Ni-based superalloy repair in aerospace applications, Canadian Aeronautics and Space Institute ASTRO'18, Quebec City, Canada, 2018 (Presentation)
7. **P.D. Enrique**, N.Y. Zhou, Electrospark deposition repair of Ni-superalloy components in aerospace applications, TraCLight Transatlantic Conference, Waterloo, Canada, 2018 (Presentation)

References

[1] M.P. Nascimento, H.J.C. Voorwald, Considerations about the welding repair effects on the structural integrity of an airframe critical to the flight-safety, Procedia Eng. 2 (2010) 1895–1903. https://doi.org/10.1016/j.proeng.2010.03.204.

[2] M.P. Nascimento, H.J.C. Voorwald, J.D.C. Payão Filho, Fatigue strength of tungsten inert gas-repaired weld joints in airplane critical structures, J. Mater. Process. Technol. 211 (2011) 1126–1135. https://doi.org/10.1016/j.jmatprotec.2011.01.016.

[3] L. Li, Z. Liu, M. Snow, Effect of defects on fatigue strength of GTAW repaired cast aluminum alloy, Weld. J. (Miami, Fla). 85 (2006) 1–6.

[4] R.P. Mudge, N.R. Wald, Laser engineered net shaping advances additive manufacturing and repair, Weld. J. (Miami, Fla). 86 (2007) 44–48.

[5] J. Bennett, D. Garcia, M. Kendrick, T. Hartman, G. Hyatt, K. Ehmann, F. You, J. Cao, Repairing Automotive Dies with Directed Energy Deposition: Industrial Application and Life Cycle Analysis, J. Manuf. Sci. Eng. Trans. ASME. 141 (2019) 1–9. https://doi.org/10.1115/1.4042078.

[6] SpaceX Launches 3D-Printed Part To Space, Creates Printed Engine Chamber, (2014) 4. http://www.spacex.com/news/2014/07/31/spacex-launches-3d-printed-part-space-creates-printed-engine-chamber-crewed (accessed June 22, 2018).

[7] GE reports successful first test of Advanced Turboprop Engine, Met. Addit. Manuf. (2018) 56. http://www.metal-am.com/ge-reports-successful-first-test-advanced-turboprop-engine/ (accessed June 21, 2018).

[8] Metal AM engine part completes maiden flight on Finnish fighter jet, Met. Addit. Manuf. (2018) 33. http://www.metal-am.com/metal-engine-part-completes-maiden-flight-finnish-fighter-jet/ (accessed June 21, 2018).

[9] D. Greitemeier, C. Dalle Donne, F. Syassen, J. Eufinger, T. Melz, Effect of surface roughness on fatigue performance of additive manufactured Ti–6Al–4V, Mater. Sci. Technol. 32 (2016) 629–634. https://doi.org/10.1179/1743284715Y.0000000053.

[10] S. Leuders, M. Thöne, A. Riemer, T. Niendorf, T. Tröster, H.A. Richard, H.J. Maier, On the mechanical behaviour of titanium alloy TiAl6V4 manufactured by selective laser melting: Fatigue resistance and crack growth performance, Int. J. Fatigue. 48 (2013) 300–307. https://doi.org/10.1016/j.ijfatigue.2012.11.011.

[11] E. Wycisk, A. Solbach, S. Siddique, D. Herzog, F. Walther, C. Emmelmann, Effects of defects in laser additive manufactured Ti-6Al-4V on fatigue properties, Phys. Procedia. 56 (2014) 371–378. https://doi.org/10.1016/j.phpro.2014.08.120.

[12] G. Kasperovich, J. Hausmann, Improvement of fatigue resistance and ductility of TiAl6V4 processed by selective laser melting, J. Mater. Process. Technol. 220 (2015) 202–214. https://doi.org/10.1016/j.jmatprotec.2015.01.025.

[13] S. Bagehorn, J. Wehr, H.J. Maier, Application of mechanical surface finishing processes for roughness reduction and fatigue improvement of additively manufactured Ti-6Al-4V parts, Int. J. Fatigue. 102 (2017) 135–142. https://doi.org/10.1016/j.ijfatigue.2017.05.008.

[14] N. Sanaei, A. Fatemi, Analysis of the effect of surface roughness on fatigue performance of powder bed fusion additive manufactured metals, Theor. Appl. Fract. Mech. 108 (2020) 102638. https://doi.org/10.1016/j.tafmec.2020.102638.

[15] D. Kong, C. Dong, X. Ni, X. Li, Corrosion of metallic materials fabricated by selective laser melting, Npj Mater. Degrad. (2019). https://doi.org/10.1038/s41529-019-0086-1.

[16] J. Stiglich, B. Campillo, I. Rosales, R. Perez, Wear characteristics of WC-6Co coating deposited using pulsed electrode surfacing technique, Surf. Eng. 15 (1999) 307–311. https://doi.org/10.1179/026708499101516650.

[17] G. Goodall, C. Kaplin, M. Brochu, Autogenous electrospark deposition of NiCoCrAlY, Can. Metall. Q. 50 (2011) 145–152. https://doi.org/10.1179/000844311X12949291727817.

[18] Y. Liu, D. Wang, C. Deng, L. Huo, L. Wang, R. Fang, Study on fabrication of ceramic coatings on Ti-6Al-4V alloy by combined ultrasonic impact treatment and electrospark, Surf. Eng. 31 (2015) 892–897. https://doi.org/10.1179/1743294414Y.0000000413.

[19] P.D. Enrique, C. Li, C. DiGiovanni, S. Peterkin, N.Y. Zhou, Electrospark deposition

interlayers for dissimilar resistance welding of steel to aluminum, Manuf. Lett. 24 (2020) 123–126. https://doi.org/10.1016/j.mfglet.2020.04.009.

[20] J. Gould, Application of Electro-Spark Deposition as a Joining Technology, Weld. J. 90 (2011) 191–197.

[21] R.N. Johnson, G.L. Sheldon, Advances in the electrospark deposition coating process, J. Vac. Sci. Technol. A Vacuum, Surfaces, Film. 4 (1986) 2740–2746. https://doi.org/10.1116/1.573672.

[22] S.K. Tang, T.C. Nguyen, Y. Zhou, Materials transfer in electro-spark deposition of TiCp/Ni metal-matrix composite coating on Cu substrate, Weld. J. 89 (2010) 172-s to 180-s.

[23] K.P. Kees, Hard-facing with electro-spark deposition. Final report, Richland, WA (United States), 1983. https://doi.org/10.2172/5537601.

[24] S. Peterkin, Electro-Spark Deposition Machine Design, Physical Controls and Parameter Effects, University of Waterloo, 2016.

[25] A. Lešnjak, J. Tušek, Processes and properties of deposits in electrospark deposition, Sci. Technol. Weld. Join. 7 (2002) 391–396. https://doi.org/10.1179/136217102225006886.

[26] S. Frangini, A. Masci, A study on the effect of a dynamic contact force control for improving electrospark coating properties, Surf. Coatings Technol. 204 (2010) 2613–2623. https://doi.org/10.1016/j.surfcoat.2010.02.006.

[27] P.Z. Wang, G.S. Pan, Y. Zhou, J.X. Qu, H.S. Shao, Accelerated electrospark deposition and the wear behavior of coatings, J. Mater. Eng. Perform. 6 (1997) 780–784. https://doi.org/10.1007/s11665-997-0081-5.

[28] V.D. Belik, R. V. Litvin, M.S. Kovalchenko, A.A. Rogozinskaya, Effect of pulse duration and size of interelectrode interval on electrospark spraying. II. Effect of pulse duration and size of interelectrode interval on composition and mechanical properties of coatings, Powder Metall. Met. Ceram. 46 (2007) 95–99. https://doi.org/10.1007/s11106-007-0015-7.

[29] P.D. Enrique, S. Peterkin, N.Y. Zhou, Parametric study of Automated Electrospark Deposition for Ni-superalloys, Weld. J. (2021).

[30] W.E. Wood, B. Adam, J. Kadali, R. Talla, T. Langston, Heat-Affected Zone Formation in Electrospark-Deposition Additive Manufacturing on Ultrahigh-Strength Steel, Mater. Perform. Charact. 6 (2017) MPC20160038. https://doi.org/10.1520/MPC20160038.

[31] D.F. Paulonis, J.J. Schirra, Alloy 718 at Pratt & Whitney: Historical Perspective and Future Challenges, in: Superalloys 718, 625, 706 Var. Deriv., TMS, 2001: pp. 13–23. https://doi.org/10.7449/2001/Superalloys_2001_13_23.

[32] R.E. Schafrik, D.D. Ward, J.R. Groh, Application of Alloy 718 in GE Aircraft Engines: Past, Present and Next Five Years, in: Superalloys 718, 625, 706 Var. Deriv., TMS, 2001: pp. 1–11. https://doi.org/10.7449/2001/Superalloys_2001_1_11.

[33] R.P. Jewett, J.A. Halchak, The Use of Alloy 718 in the Space Shuttle Main Engine, in: Superalloys 718, 625 Var. Deriv., TMS, 1991: pp. 749–760. https://doi.org/10.7449/1991/Superalloys_1991_749_760.

[34] Special Metals, INCONEL Alloy 718, 2007. http://www.specialmetals.com/assets/smc/documents/inconel_alloy_718.pdf.

[35] Haynes International, HASTELLOY X alloy, 2019. http://www.haynes.ch/doc/HASTELLOY_X.pdf.

[36] A.M. Russell, K.L. Lee, Structure-Property Relations in Nonferrous Metals, John Wiley & Sons, 2005.

[37] M. Jouiad, E. Marin, R.S. Devarapalli, J. Cormier, F. Ravaux, C. Le Gall, J.M. Franchet, Microstructure and mechanical properties evolutions of alloy 718 during isothermal and thermal cycling over-aging, Mater. Des. 102 (2016) 284–296. https://doi.org/10.1016/j.matdes.2016.04.048.

[38] M.J. Donachie, S.J. Donachie, Superalloys: A Technical Guide, ASM International, 2002. https://doi.org/10.1361/stgs2002p001.

[39] M. Sundararaman, P. Mukhopadhyay, S. Banerjee, Carbide Precipitation in Nickel Base

Superalloys 718 and 625 and Their Effect on Mechanical Properties, in: Superalloys 718, 625, 706 Var. Deriv., TMS, 1997: pp. 367–378. https://doi.org/10.7449/1997/Superalloys_1997_367_378.

[40] S. Azadian, L.Y. Wei, R. Warren, Delta phase precipitation in inconel 718, Mater. Charact. 53 (2004) 7–16. https://doi.org/10.1016/j.matchar.2004.07.004.

[41] Y. Desvallees, M. Bouzidi, F. Bois, N. Beaude, Delta Phase in INCONEL 718: Mechanical Properties and Forging Process Requirements, in: Superalloys 718, 625, 706 Var. Deriv., TMS, 1994: pp. 281–291. https://doi.org/10.7449/1994/Superalloys_1994_281_291.

[42] Q. Lu, O. Lu, Microstructural evolution in alloy 718 after multiple repair and PWHT cycles, Ohio State University, 1999. https://etd.ohiolink.edu/!etd.send_file?accession=osu148818704954173&disposition=inline.

[43] A. Mitchell, A.J. Schmalz, C. Schvezov, S.L. Cockcroft, The Precipitation of Primary Carbides in Alloy 718, Superalloys 718, 625, 706 Var. Deriv. (1994) 65–78. https://doi.org/10.7449/1994/Superalloys_1994_65_78.

[44] R.G. Thompson, J.R. Dobbs, D.E. Mayo, The Effect of Heat Treatment on Microfissuring in Alloy 718, Weld. J. (1986) 299.

[45] S. Sui, J. Chen, E. Fan, H. Yang, X. Lin, W. Huang, The influence of Laves phases on the high-cycle fatigue behavior of laser additive manufactured Inconel 718, Mater. Sci. Eng. A. 695 (2017) 6–13. https://doi.org/10.1016/j.msea.2017.03.098.

[46] S. Sui, H. Tan, J. Chen, C. Zhong, Z. Li, W. Fan, A. Gasser, W. Huang, The influence of Laves phases on the room temperature tensile properties of Inconel 718 fabricated by powder feeding laser additive manufacturing, Acta Mater. 164 (2019) 413–427. https://doi.org/10.1016/j.actamat.2018.10.032.

[47] J.C. Lippold, Welding Metallurgy and Weldability, John Wiley & Sons, Inc., Hoboken, New Jersey, 2015.

[48] S. Kou, Welding Metallurgy, 2nd ed., John Wiley & Sons, Inc., New Jersey, USA, 2003.

http://books.google.com/books?hl=en&lr=&id=N8gICBzzgRwC&oi=fnd&pg=PR7&dq=WELDING+METALLURGY&ots=KbMCYOBY2l&sig=bUKTMZRhqD6LE6kzQIivLlTfJK4.

[49] E. Anisimov, A.K. Khan, O.A. Ojo, Analysis of microstructure in electro-spark deposited IN718 superalloy, Mater. Charact. 119 (2016) 233–240. https://doi.org/10.1016/j.matchar.2016.07.025.

[50] Y. Xie, M. Wang, Microstructural morphology of electrospark deposition layer of a high gamma prime superalloy, Surf. Coatings Technol. 201 (2006) 691–698. https://doi.org/10.1016/j.surfcoat.2005.12.034.

[51] M. Ebrahimnia, F.M. Ghaini, H.R. Shahverdi, Hot cracking in pulsed laser processing of a nickel based superalloy built up by electrospark deposition, Sci. Technol. Weld. Join. 19 (2014) 25–29. https://doi.org/10.1179/1362171813Y.0000000157.

[52] S.-H. Kang, Y. Deguchi, K. Yamamoto, K. Ogi, M. Shirai, Solidification Process and Behavior of Alloying Elements in Ni-Based Superalloy Inconel718, Mater. Trans. 45 (2004) 2728–2733. https://doi.org/10.2320/matertrans.45.2728.

[53] D.W. Heard, J. Boselli, R. Rioja, E.A. Marquis, R. Gauvin, M. Brochu, Interfacial morphology development and solute trapping behavior during rapid solidification of an Al-Li-Cu alloy, Acta Mater. 61 (2013) 1571–1580. https://doi.org/10.1016/j.actamat.2012.11.034.

[54] K.R. Vishwakarma, O.A. Ojo, N.L. Richards, Nano-size solidification microconstituents in electro-spark deposited Ni-base superalloy, Philos. Mag. Lett. 95 (2015) 30–36. https://doi.org/10.1080/09500839.2014.995740.

[55] G. Rotella, S. Imbrogno, S. Candamano, D. Umbrello, Surface integrity of machined additively manufactured Ti alloys, J. Mater. Process. Technol. 259 (2018) 180–185. https://doi.org/10.1016/j.jmatprotec.2018.04.030.

[56] L. Lizzul, M. Sorgato, R. Bertolini, A. Ghiotti, S. Bruschi, Influence of additive manufacturing-induced anisotropy on tool wear in end milling of Ti6Al4V, Tribol. Int. 146 (2020) 106200. https://doi.org/10.1016/j.triboint.2020.106200.

[57] J.C. Heigel, T.Q. Phan, J.C. Fox, T.H. Gnaupel-Herold, Experimental Investigation of Residual Stress and its Impact on Machining in Hybrid Additive/Subtractive Manufacturing, Procedia Manuf. 26 (2018) 929–940. https://doi.org/10.1016/j.promfg.2018.07.120.

[58] H. Yamaguchi, O. Fergani, P.Y. Wu, Modification using magnetic field-assisted finishing of the surface roughness and residual stress of additively manufactured components, CIRP Ann. - Manuf. Technol. 66 (2017) 305–308. https://doi.org/10.1016/j.cirp.2017.04.084.

[59] A. Boschetto, L. Bottini, F. Veniali, Surface roughness and radiusing of Ti6Al4V selective laser melting-manufactured parts conditioned by barrel finishing, Int. J. Adv. Manuf. Technol. 94 (2018) 2773–2790. https://doi.org/10.1007/s00170-017-1059-6.

[60] M.S. Duval-Chaneac, S. Han, C. Claudin, F. Salvatore, J. Bajolet, J. Rech, Experimental study on finishing of internal laser melting (SLM) surface with abrasive flow machining (AFM), Precis. Eng. 54 (2018) 1–6. https://doi.org/10.1016/j.precisioneng.2018.03.006.

[61] S. Han, F. Salvatore, J. Rech, J. Bajolet, Abrasive flow machining (AFM) finishing of conformal cooling channels created by selective laser melting (SLM), Precis. Eng. 64 (2020) 20–33. https://doi.org/10.1016/j.precisioneng.2020.03.006.

[62] A.P. Nagalingam, S.H. Yeo, Controlled hydrodynamic cavitation erosion with abrasive particles for internal surface modification of additive manufactured components, Wear. 414–415 (2018) 89–100. https://doi.org/10.1016/j.wear.2018.08.006.

[63] H. Zhang, R. Chiang, H. Qin, Z. Ren, X. Hou, D. Lin, G.L. Doll, V.K. Vasudevan, Y. Dong, C. Ye, The effects of ultrasonic nanocrystal surface modification on the fatigue performance of 3D-printed Ti64, Int. J. Fatigue. 103 (2017) 136–146. https://doi.org/10.1016/j.ijfatigue.2017.05.019.

[64] P. Walker, S. Malz, E. Trudel, S. Nosir, M.S.A. ElSayed, L. Kok, Effects of Ultrasonic Impact Treatment on the Stress-Controlled Fatigue Performance of Additively Manufactured DMLS Ti-6Al-4V Alloy, Appl. Sci. 9 (2019). https://doi.org/10.3390/app9224787.

[65] F. Using, S. Laser, Ultrasonic Peening Treatment Used to Improve Stress Corrosion

Resistance of AlSi10Mg Components, (2019). https://doi.org/10.3390/met9010103.

[66] N.E. Uzan, S. Ramati, R. Shneck, N. Frage, O. Yeheskel, On the effect of shot-peening on fatigue resistance of AlSi10Mg specimens fabricated by additive manufacturing using selective laser melting (AM-SLM), Addit. Manuf. 21 (2018) 458–464. https://doi.org/10.1016/j.addma.2018.03.030.

[67] A. Maamoun, M. Elbestawi, S. Veldhuis, Influence of Shot Peening on AlSi10Mg Parts Fabricated by Additive Manufacturing, J. Manuf. Mater. Process. 2 (2018) 40. https://doi.org/10.3390/jmmp2030040.

[68] P.D. Enrique, E. Marzbanrad, Y. Mahmoodkhani, Z. Jiao, E. Toyserkani, N.Y. Zhou, Surface modification of binder-jet additive manufactured Inconel 625 via electrospark deposition, Surf. Coatings Technol. 362 (2019) 141–149. https://doi.org/10.1016/j.surfcoat.2019.01.108.

[69] A. Krishnan, F. Fang, Review on mechanism and process of surface polishing using lasers, Front. Mech. Eng. 14 (2019) 299–319. https://doi.org/10.1007/s11465-019-0535-0.

[70] M.A. Obeidi, E. McCarthy, B. O'Connell, I.U. Ahad, D. Brabazon, Laser polishing of additive manufactured 316L stainless steel synthesized by selective laser melting, Materials (Basel). 12 (2019). https://doi.org/10.3390/ma12060991.

[71] L. Chen, B. Richter, X. Zhang, X. Ren, F.E. Pfefferkorn, Modification of surface characteristics and electrochemical corrosion behavior of laser powder bed fused stainless-steel 316L after laser polishing, Addit. Manuf. 32 (2020) 101013. https://doi.org/10.1016/j.addma.2019.101013.

[72] B. Richter, N. Blanke, C. Werner, N.D. Parab, T. Sun, F. Vollertsen, F.E. Pfefferkorn, High-speed X-ray investigation of melt dynamics during continuous-wave laser remelting of selective laser melted Co-Cr alloy, CIRP Ann. 68 (2019) 229–232. https://doi.org/10.1016/j.cirp.2019.04.110.

[73] J. Dos Santos Solheid, H.J. Seifert, W. Pfleging, Laser surface modification and polishing of additive manufactured metallic parts, Procedia CIRP. 74 (2018) 280–284. https://doi.org/10.1016/j.procir.2018.08.111.

[74] E. Yasa, J. Deckers, J. Kruth, The investigation of the influence of laser re-melting on density, surface quality and microstructure of selective laser melting parts, Rapid Prototyp. J. 17 (2011) 312–327. https://doi.org/10.1108/13552541111156450.

[75] J.G. Lunney, R. Jordan, Pulsed laser ablation of metals, Appl. Surf. Sci. 127–129 (1998) 941–946. https://doi.org/10.1016/S0169-4332(97)00770-8.

[76] O. Černašėjus, J. Škamat, V. Markovič, N. Višniakov, S. Indrišiūnas, Effect of Laser Processing on Surface Properties of Additively Manufactured 18-Percent Nickel Maraging Steel Parts, Coatings. 10 (2020) 600. https://doi.org/10.3390/coatings10060600.

[77] D. Loaldi, M. Kain, G. Tosello, Comparison of Selective Laser Melting Post-Processes based on Amplitude and Functional Surface Roughness parameters, in: Jt. Spec. Interes. Gr. Meet. between Euspen ASPE Adv. Precis. Addit. Manuf., 2019.

[78] M. Anilli, A.G. Demir, B. Previtali, Additive manufacturing of laser cutting nozzles by SLM: processing, finishing and functional characterization, Rapid Prototyp. J. 24 (2018) 562–583. https://doi.org/10.1108/RPJ-05-2017-0106.

[79] P.D. Enrique, A. Keshavarzkermani, R. Esmaeilizadeh, S. Peterkin, H. Jahed, E. Toyserkani, N.Y. Zhou, Enhancing fatigue life of additive manufactured parts with electrospark deposition post-processing, Addit. Manuf. 36 (2020) 101526. https://doi.org/10.1016/j.addma.2020.101526.

[80] N.J. Petch, The cleavage strength of polycrystals, J. Iron Steel Inst. 174 (1953) 25–28.

[81] E.O. Hall, The Deformation and Ageing of Mild Steel: III Discussion of Results, Proc. Phys. Soc. London Sect. B. 64 (1951) 747–753. https://doi.org/10.1088/0370-1301/64/9/303.

[82] P.D. Enrique, Z. Jiao, N.Y. Zhou, E. Toyserkani, Dendritic coarsening model for rapid solidification of Ni-superalloy via electrospark deposition, J. Mater. Process. Technol. 258 (2018) 138–143. https://doi.org/10.1016/j.jmatprotec.2018.03.023.

[83] B.D. Sartwell, K.O. Legg, N. Price, D. Aylor, V. Champagne, M. Pepi, T. Pollard, Electrospark Deposition for Depot- and Field-Level Component Repair and Replacement of Hard Chromium Plating, Environ. Secur. Technol. Certif. Progr. (2006) 299.

http://www.dtic.mil/docs/citations/ADA603502.

[84] M. Brochu, G. Portillo, Grain Refinement during Rapid Solidification of Aluminum-Zirconium Alloys Using Electrospark Deposition, Mater. Trans. 54 (2013) 934–939. https://doi.org/10.2320/matertrans.MD201228.

[85] X. Wei, Z. Chen, J. Zhong, L. Wang, Z. Hou, Y. Zhang, F. Tan, Facile preparation of nanocrystalline Fe 2 B coating by direct electro-spark deposition of coarse-grained Fe 2 B electrode material, J. Alloys Compd. 717 (2017) 31–40. https://doi.org/10.1016/j.jallcom.2017.05.081.

[86] R. Farhat, M. Brochu, Utilisation of electrospark deposition to restore local oxidation resistance properties in damaged NiCoCrAlY and CoNiCrAlY coatings, Can. Metall. Q. 51 (2012) 313–319. https://doi.org/10.1179/1879139512Y.0000000019.

[87] J. Wang, H. Meng, H. Yu, Z. Fan, D. Sun, Wear characteristics of spheroidal graphite roll WC-8Co coating produced by electro-spark deposition, Rare Met. 29 (2010) 174–179. https://doi.org/10.1007/s12598-010-0030-6.

[88] Y. Ruan, A. Mohajerani, M. Dao, Microstructural and Mechanical-Property Manipulation through Rapid Dendrite Growth and Undercooling in an Fe-based Multinary Alloy, Sci. Rep. 6 (2016) 1–11. https://doi.org/10.1038/srep31684.

[89] M. Ebrahimnia, F. Malek Ghaini, Y.J. Xie, H. Shahverdi, Microstructural characteristics of the built up layer of a precipitation hardened nickel based superalloy by electrospark deposition, Surf. Coatings Technol. 258 (2014) 515–523. https://doi.org/10.1016/j.surfcoat.2014.08.045.

[90] J. Saarimäki, M. Lundberg, J.J. Moverare, H. Brodin, Characterization of Hastelloy X Produced by Laser Powder Bed Additive Manufacturing, World PM2016. (2016) 1–6.

[91] ASM International, Metallographic Technique for Nonferrous Metals and Special-Purpose Alloys, ASM International, 1998.

[92] W.F. Savage, E.F. Nippes, T.W. Miller, Microsegregation in 70Cu-30Ni Weld Metal, Weld. J. (1976) 165s-173s.

[93] A. Rollett, F. Humphreys, G. Rohrer, M. Hatherly, Recrystallisation and Related Annealing Phenomena, 2nd ed., Elsevier, 2004.

[94] R.J. Brook, Controlled Grain Growth, in: Ceram. Fabr. Process. Treatise Mater. Sci. Technol., 1976: pp. 331–364. https://doi.org/10.1016/B978-0-12-341809-8.50024-3.

[95] J.W.. A.S.M.. E.T.W. Elmer, The Influence Of Cooling Rate On The Microstructure Of Stainless Steel Alloys, University of California, 1988.

[96] J. Kaneko, Dendrite coarsening during solidification of hypo- and hyper-eutectic Al-Cu alloys, J. Mater. Sci. 12 (1977) 1392–1400. https://doi.org/10.1007/BF00540853.

[97] Y. Sun, W.B. Andrews, K. Thornton, P.W. Voorhees, Self-Similarity and the Dynamics of Coarsening in Materials, Sci. Rep. 8 (2018) 1–8. https://doi.org/10.1038/s41598-018-36354-8.

[98] J.W. Martin, R.D. Doherty, B. Cantor, Stability of Microstructure in Metallic Systems, Cambridge University Press, 1997.

[99] MatWeb, Special Metals INCONEL Alloy 718, (2017). http://www.matweb.com (accessed June 13, 2017).

[100] T. Hanamura, H. Qiu, Analysis of Fracture Toughness Mechanism in Ultra-fine-grained Steels, Springer Japan, Tokyo, 2014. https://doi.org/10.1007/978-4-431-54499-9.

[101] A. Rollett, F. Humphreys, G.S. Rohrer, M. Hatherly, Recrystallization and Related Annealing Phenomena: Second Edition, 2004. https://doi.org/10.1016/B978-0-08-044164-1.X5000-2.

[102] P.D. Enrique, Z. Jiao, N.Y. Zhou, E. Toyserkani, Effect of microstructure on tensile properties of electrospark deposition repaired Ni-superalloy, Mater. Sci. Eng. A. 729 (2018) 268–275. https://doi.org/10.1016/j.msea.2018.05.049.

[103] P. Leo, G. Renna, G. Casalino, Study of the Direct Metal Deposition of AA2024 by ElectroSpark for Coating and Reparation Scopes, Appl. Sci. 7 (2017) 945. https://doi.org/10.3390/app7090945.

[104] C.J. Chen, M.C. Wang, D.S. Wang, H.S. Liang, P. Feng, Characterisations of electrospark

deposition Stellite 6 alloy coating on 316L sealed valve used in nuclear power plant, Mater. Sci. Technol. 26 (2010) 276–280. https://doi.org/10.1179/174328409X430447.

[105] A. Carofalo, V. Dattoma, R. Nobile, F.W. Panella, G. Alfeo, A. Scialpi, G.P. Zanon, Mechanical Characterization of a Nickel-based Superalloy Repaired using MicroPlasma and ESD Technology, Procedia Eng. 109 (2015) 312–319. https://doi.org/10.1016/j.proeng.2015.06.238.

[106] J. Filliben, A. Heckert, NIST Dataplot, (2016). https://www.itl.nist.gov/div898/software/dataplot/refman2/auxillar/hedgeg.htm.

[107] G.M. Sullivan, R. Feinn, Using Effect Size—or Why the P Value Is Not Enough , J. Grad. Med. Educ. 4 (2012) 279–282. https://doi.org/10.4300/jgme-d-12-00156.1.

[108] J.A. Durlak, How to Select, Calculate, and Interpret Effect Sizes, J. Pediatr. Psychol. 34 (2009) 917–928. https://doi.org/10.1093/jpepsy/jsp004.

[109] M. Fakoori Hasanabadi, F. Malek Ghaini, M. Ebrahimnia, H.R. Shahverdi, Production of amorphous and nanocrystalline iron based coatings by electro-spark deposition process, Surf. Coatings Technol. 270 (2015) 95–101. https://doi.org/10.1016/j.surfcoat.2015.03.016.

[110] P. Guo, X. Lin, J. Li, Y. Zhang, M. Song, W. Huang, Electrochemical behavior of Inconel 718 fabricated by laser solid forming on different sections, Corros. Sci. 132 (2018) 79–89. https://doi.org/10.1016/j.corsci.2017.12.021.

[111] S.H. Baghjari, F. Malek Ghaini, H.R. Shahverdi, C. Mapelli, S. Barella, D. Ripamonti, Laser welding of niobium to 410 steel with a nickel interlayer produced by electro spark deposition, Mater. Des. 107 (2016) 108–116. https://doi.org/10.1016/j.matdes.2016.06.022.

[112] R.K. GUPTA, C. Mathew, P. Ramkumar, Strain Hardening in Aerospace Alloys, Front. Aerosp. Eng. 4 (2015) 1–13. https://doi.org/10.12783/fae.2015.0401.01.

[113] R. Cortés, E.R.R. Barragán, V.H.H. López, R.R.R. Ambriz, D. Jaramillo, Mechanical properties of Inconel 718 welds performed by gas tungsten arc welding, Int. J. Adv. Manuf. Technol. 94 (2017) 3949–3961. https://doi.org/10.1007/s00170-017-1128-x.

[114] H. Peter, U. Zerbst, Recent Trends in Fracture and Damage Mechanics, in: Recent Trends Fract. Damage Mech., 2016: pp. 61–86. https://doi.org/10.1007/978-3-319-21467-2.

[115] J. Yang, H. Li, D. Hu, M. Dixon, Microstructural characterisation of fatigue crack growth fracture surfaces of lamellar Ti45Al2Mn2Nb1B, Intermetallics. 45 (2014) 89–95. https://doi.org/10.1016/j.intermet.2013.10.011.

[116] H. Tada, P. Paris, G. Irwin, Stress Analysis Results for Common Test Specimen Configurations, in: Stress Anal. Cracks Handbook, Third Ed., ASME, Three Park Avenue New York, NY 10016-5990, NY 10016-5990, 2017: pp. 39–80. https://doi.org/10.1115/1.801535.ch2.

[117] J.W. Hutchinson, STRESSES AND FAILURE MODES IN THIN FILMS AND MULTILAYERS, 1996.

[118] H. Ming-Yuan, J.W. Hutchinson, Crack deflection at an interface between dissimilar elastic materials, Int. J. Solids Struct. 25 (1989) 1053–1067. https://doi.org/10.1016/0020-7683(89)90021-8.

[119] W. Callister, D. Rethwisch, Materials science and engineering: an introduction, 2007. https://doi.org/10.1016/0025-5416(87)90343-0.

[120] D. Hull, D.J. Bacon, Introduction to Dislocations, Fifth, Elsevier, Oxford, 2011. https://doi.org/10.1016/C2009-0-64358-0.

[121] M. Ma, Z. Wang, X. Zeng, Effect of energy input on microstructural evolution of direct laser fabricated IN718 alloy, Mater. Charact. 106 (2015) 420–427. https://doi.org/10.1016/j.matchar.2015.06.027.

[122] J.J. Schirra, R.H. Caless, R.W. Hatala, The Effect of Laves Phase on the Mechanical Properties of Wrought and Cast + HIP Inconel 718, in: Superalloys 718, 625 Var. Deriv., TMS, 1991: pp. 375–388. https://doi.org/10.7449/1991/Superalloys_1991_375_388.

[123] E.L. Stevens, J. Toman, A.C. To, M. Chmielus, Variation of hardness, microstructure, and Laves phase distribution in direct laser deposited alloy 718 cuboids, Mater. Des. 119 (2017) 188–198. https://doi.org/10.1016/j.matdes.2017.01.031.

[124] P.D. Enrique, A. Keshavarzkermani, N.Y. Zhou, Effect of Micro-segregation on High Temperature Microstructure Evolution in Rapid Solidification Processed Nb-rich Ni-superalloys, Adv. Eng. Mater. (2021). https://doi.org/10.1002/adem.202001396.

[125] E.J. Lavernia, T.S. Srivatsan, The rapid solidification processing of materials: Science, principles, technology, advances, and applications, J. Mater. Sci. 45 (2010) 287–325. https://doi.org/10.1007/s10853-009-3995-5.

[126] L.Y. Wang, Z.J. Zhou, C.P. Li, G.F. Chen, G.P. Zhang, Comparative investigation of small punch creep resistance of Inconel 718 fabricated by selective laser melting, Mater. Sci. Eng. A. 745 (2019) 31–38. https://doi.org/10.1016/j.msea.2018.12.083.

[127] H.Y. Wan, Z.J. Zhou, C.P. Li, G.F. Chen, G.P. Zhang, Enhancing Fatigue Strength of Selective Laser Melting-Fabricated Inconel 718 by Tailoring Heat Treatment Route, Adv. Eng. Mater. 20 (2018) 1–6. https://doi.org/10.1002/adem.201800307.

[128] E.A. Lass, M.R. Stoudt, M.E. Williams, M.B. Katz, L.E. Levine, T.Q. Phan, T.H. Gnaeupel-Herold, D.S. Ng, Formation of the Ni3Nb δ-Phase in Stress-Relieved Inconel 625 Produced via Laser Powder-Bed Fusion Additive Manufacturing, Metall. Mater. Trans. A Phys. Metall. Mater. Sci. 48 (2017) 5547–5558. https://doi.org/10.1007/s11661-017-4304-6.

[129] H. Qi, M. Azer, A. Ritter, Studies of standard heat treatment effects on microstructure and mechanical properties of laser net shape manufactured INCONEL 718, Metall. Mater. Trans. A Phys. Metall. Mater. Sci. 40 (2009) 2410–2422. https://doi.org/10.1007/s11661-009-9949-3.

[130] D. Zhang, W. Niu, X. Cao, Z. Liu, Effect of standard heat treatment on the microstructure and mechanical properties of selective laser melting manufactured Inconel 718 superalloy, Mater. Sci. Eng. A. 644 (2015) 32–40. https://doi.org/10.1016/j.msea.2015.06.021.

[131] F. Lyu, F. Liu, X. Hu, X. Yang, C. Huang, D. Shi, The δ phase precipitation of an Inconel 718 superalloy fabricated by electromagnetic stirring assisted laser solid forming, Materials (Basel). 12 (2019). https://doi.org/10.3390/ma12162604.

[132] F. Liu, F. Lyu, F. Liu, X. Lin, C. Huang, Laves phase control of inconel 718 superalloy

fabricated by laser direct energy deposition via δ aging and solution treatment, J. Mater. Res. Technol. 9 (2020) 9753–9765. https://doi.org/10.1016/j.jmrt.2020.06.061.

[133] W. Huang, Z. Wang, Isothermal Solid-State Transformations of Inconel 718 Alloy Fabricated by Selective Laser Melting, Adv. Eng. Mater. 2000982 (2020) 2000982. https://doi.org/10.1002/adem.202000982.

[134] J. Lu, Z. Yang, Y. Zhou, J. Huang, J. Yan, Y. Dang, Y. Yuan, Y. Gu, Failure analysis for a dry-pulverized coal gasifier burner made up of Inconel 718 superalloy, Eng. Fail. Anal. 97 (2019) 227–233. https://doi.org/10.1016/j.engfailanal.2019.01.049.

[135] R.E. Dundas, Investigation of Failure in Gas Turbines: Part 2 — Engineering and Metallographic Aspects of Failure Investigation, in: Vol. 2 Combust. Fuels; Oil Gas Appl. Cycle Innov. Heat Transf. Electr. Power; Ind. Cogener. Ceram. Struct. Dyn. Control. Diagnostics Instrumentation; IGTI Sch. Award, American Society of Mechanical Engineers, 1993: p. V002T10A003. https://doi.org/10.1115/93-GT-084.

[136] C. Kumara, A. Segerstark, F. Hanning, N. Dixit, S. Joshi, J. Moverare, P. Nylén, Microstructure modelling of laser metal powder directed energy deposition of alloy 718, Addit. Manuf. 25 (2019) 357–364. https://doi.org/10.1016/j.addma.2018.11.024.

[137] P.D. Enrique, Z. Jiao, N.Y. Zhou, Effect of Direct Aging on Heat-Affected Zone and Tensile Properties of Electrospark-Deposited Alloy 718, Metall. Mater. Trans. A. 50 (2019) 285–294. https://doi.org/10.1007/s11661-018-4997-1.

[138] J. Dong, X. Xie, Z. Xu, S. Zhang, M. Chen, Tem Study on Microstructure Behavior of Alloy 718 After Long Time Exposure at High Temperatures, in: Superalloys 718, 625, 706 Var. Deriv., TMS, 1994: pp. 649–658. https://doi.org/10.7449/1994/Superalloys_1994_649_658.

[139] C. Slama, C. Servant, G. Cizeron, Aging of the Inconel 718 alloy between 500 and 750 °C, J. Mater. Res. 12 (1997) 2298–2316. https://doi.org/10.1557/JMR.1997.0306.

[140] L.M. Suave, D. Bertheau, J. Cormier, P. Villechaise, A. Soula, Z. Hervier, J. Laigo, Impact of microstructural evolutions during thermal aging of Alloy 625 on its monotonic mechanical properties, MATEC Web Conf. 14 (2014) 21001.

https://doi.org/10.1051/matecconf/20141421001.

[141] L. Ratke, P.W. Voorhees, Nucleation, Growth and Coarsening, in: Growth and Coarsening, 2002: pp. 205–224. https://doi.org/10.1007/978-3-662-04884-9_10.

[142] X.J. Pang, D.J. Dwyer, M. Gao, P. Valerio, R.P. Wei, Surface enrichment and grain boundary segregation of niobium in inconel 718 single- and poly-crystals, Scr. Metall. Mater. 31 (1994) 345–350. https://doi.org/10.1016/0956-716X(94)90294-1.

[143] D.H. Ping, Y.F. Gu, C.Y. Cui, H. Harada, Grain boundary segregation in a Ni-Fe-based (Alloy 718) superalloy, Mater. Sci. Eng. A. 456 (2007) 99–102. https://doi.org/10.1016/j.msea.2007.01.090.

[144] H. Rajek, Computer simulation of precipitation kinetics in solid metals and application to the complex power plant steel CB8, Graz University of Technology, 2005. http://scholar.google.com/scholar?hl=en&btnG=Search&q=intitle:Computer+simulation+of+precipitation+kinetics+in+solid+metals+and+application+to+the+complex+power+plant+steel+CB8#0.

[145] J. Lacaze, M. Dehmas, A. Niang, B. Viguier, TEM study of high-temperature precipitation of delta phase in inconel 718 alloy, Adv. Mater. Sci. Eng. 2011 (2011). https://doi.org/10.1155/2011/940634.

[146] C. Zhang, L. Yu, H. Wang, Kinetic Analysis for High-Temperature Coarsening of γ″ Phase in Ni-Based Superalloy GH4169, Materials (Basel). 12 (2019) 2096. https://doi.org/10.3390/ma12132096.

[147] A. Devaux, L. Nazé, R. Molins, A. Pineau, A. Organista, J.Y. Guédou, J.F. Uginet, P. Héritier, Gamma double prime precipitation kinetic in Alloy 718, Mater. Sci. Eng. A. 486 (2008) 117–122. https://doi.org/10.1016/j.msea.2007.08.046.

[148] J.D.J. Boyd, R.. B. Nicholson, The coarsening behaviour of θ″ and θ′ precipitates in two Al-Cu alloys, Acta Metall. 19 (1971) 1379–1391. https://doi.org/10.1016/0001-6160(71)90076-9.

[149] M.J. Sohrabi, H. Mirzadeh, Revisiting the Diffusion of Niobium in an As-Cast Nickel-Based Superalloy During Annealing at Elevated Temperatures, Met. Mater. Int. (2019).

https://doi.org/10.1007/s12540-019-00342-y.

[150] M. Rafiei, H. Mirzadeh, M. Malekan, M.J. Sohrabi, Homogenization kinetics of a typical nickel-based superalloy, J. Alloys Compd. 793 (2019) 277–282. https://doi.org/10.1016/j.jallcom.2019.04.147.

[151] S. Kumar, W.A. Curtin, Crack interaction with microstructure, Mater. Today. 10 (2007) 34–44. https://doi.org/10.1016/S1369-7021(07)70207-9.

[152] S. Li, J. Yang, J. Zhuang, Q. Deng, J. Du, X. Xie, B. Li, Z. Xu, Z. Cao, Z. Su, C. Jiang, The Effect of Delta-Phase on Crack Propagation Under Creep and Fatigue Conditions in Alloy 718, in: Superalloys 718, 625, 706 Var. Deriv., TMS, 1994: pp. 545–555. https://doi.org/10.7449/1994/Superalloys_1994_545_555.

[153] S. Afkhami, M. Dabiri, S.H. Alavi, T. Björk, A. Salminen, Fatigue characteristics of steels manufactured by selective laser melting, Int. J. Fatigue. 122 (2019) 72–83. https://doi.org/10.1016/j.ijfatigue.2018.12.029.

[154] K. Bammert, H. Sandstede, Measurements of the Boundary Layer Development Along a Turbine Blade With Rough Surfaces., Am. Soc. Mech. Eng. 102 (1980) 978–983.

[155] Y. Il Yun, I.Y. Park, S.J. Song, Performance degradation due to blade surface roughness in a single-stage axial turbine, J. Turbomach. 127 (2005) 137–143. https://doi.org/10.1115/1.1811097.

[156] Q. Zhang, P.M. Ligrani, Aerodynamic losses of a cambered turbine vane: Influences of surface roughness and freestream turbulence intensity, J. Turbomach. 128 (2006) 536–546. https://doi.org/10.1115/1.2185125.

[157] Z. Chen, X. Wu, D. Tomus, C.H.J. Davies, Surface roughness of Selective Laser Melted Ti-6Al-4V alloy components, Addit. Manuf. 21 (2018) 91–103. https://doi.org/10.1016/j.addma.2018.02.009.

[158] U. Ali, R. Esmaeilizadeh, F. Ahmed, D. Sarker, W. Muhammad, A. Keshavarzkermani, Y. Mahmoodkhani, E. Marzbanrad, E. Toyserkani, Identification and characterization of spatter particles and their effect on surface roughness, density and mechanical response of 17-4 PH stainless steel laser powder-bed fusion parts, Mater. Sci. Eng. A. 756 (2019) 98–

107. https://doi.org/10.1016/j.msea.2019.04.026.

[159] R. Esmaeilizadeh, U. Ali, A. Keshavarzkermani, Y. Mahmoodkhani, E. Marzbanrad, E. Toyserkani, On the effect of spatter particles distribution on the quality of Hastelloy X parts made by laser powder-bed fusion additive manufacturing, J. Manuf. Process. 37 (2019) 11–20. https://doi.org/10.1016/j.jmapro.2018.11.012.

[160] Z. Dong, Y. Liu, W. Li, J. Liang, Orientation dependency for microstructure, geometric accuracy and mechanical properties of selective laser melting AlSi10Mg lattices, J. Alloys Compd. 791 (2019) 490–500. https://doi.org/10.1016/j.jallcom.2019.03.344.

[161] F. Calignano, Investigation of the accuracy and roughness in the laser powder bed fusion process, Virtual Phys. Prototyp. 13 (2018) 97–104. https://doi.org/10.1080/17452759.2018.1426368.

[162] T. Yang, T. Liu, W. Liao, E. MacDonald, H. Wei, X. Chen, L. Jiang, The influence of process parameters on vertical surface roughness of the AlSi10Mg parts fabricated by selective laser melting, J. Mater. Process. Technol. 266 (2019) 26–36. https://doi.org/10.1016/j.jmatprotec.2018.10.015.

[163] R. Mertens, S. Clijsters, K. Kempen, J.-P. Kruth, Optimization of Scan Strategies in Selective Laser Melting of Aluminum Parts With Downfacing Areas, J. Manuf. Sci. Eng. 136 (2014) 061012. https://doi.org/10.1115/1.4028620.

[164] S. Patel, A. Rogalsky, M. Vlasea, Towards understanding side-skin surface characteristics in laser powder bed fusion, J. Mater. Res. (2020). https://doi.org/10.1557/jmr.2020.125.

[165] O. Oyelola, P. Crawforth, R. M'Saoubi, A.T. Clare, Machining of Additively Manufactured Parts: Implications for Surface Integrity, Procedia CIRP. 45 (2016) 119–122. https://doi.org/10.1016/j.procir.2016.02.066.

[166] I.A. Choudhury, M.A. El-Baradie, Machinability of nickel-base super alloys: A general review, J. Mater. Process. Technol. 300 (1998) 278–284. https://doi.org/10.1016/s0924-0136(97)00429-9.

[167] A. Lamikiz, J.A. Sánchez, L.N. López de Lacalle, J.L. Arana, Laser polishing of parts built up by selective laser sintering, Int. J. Mach. Tools Manuf. 47 (2007) 2040–2050.

https://doi.org/10.1016/j.ijmachtools.2007.01.013.

[168] K.C. Yung, T.Y. Xiao, H.S. Choy, W.J. Wang, Z.X. Cai, Laser polishing of additive manufactured CoCr alloy components with complex surface geometry, J. Mater. Process. Technol. 262 (2018) 53–64. https://doi.org/10.1016/j.jmatprotec.2018.06.019.

[169] X. Wang, S. Li, Y. Fu, H. Gao, Finishing of additively manufactured metal parts by abrasive flow machining, in: Proc. 27th Annu. Int. Solid Free. Fabr. Symp., Austin, TX, 2016: pp. 2470–2472.

[170] E. Uhlmann, C. Schmiedel, J. Wendler, CFD simulation of the Abrasive Flow Machining process, Procedia CIRP. 31 (2015) 209–214. https://doi.org/10.1016/j.procir.2015.03.091.

[171] S. Sarkar, C.S. Kumar, A.K. Nath, Effects of different surface modifications on the fatigue life of selective laser melted 15–5 PH stainless steel, Mater. Sci. Eng. A. 762 (2019) 138109. https://doi.org/10.1016/j.msea.2019.138109.

[172] V. Urlea, V. Brailovski, Electropolishing and electropolishing-related allowances for powder bed selectively laser-melted Ti-6Al-4V alloy components, J. Mater. Process. Technol. 242 (2017) 1–11. https://doi.org/10.1016/j.jmatprotec.2016.11.014.

[173] D. Zhu, L. Yu, R. Zhang, Dissolution effects with different microstructures of inconel 718 on surface integrity in electrochemical machining, J. Electrochem. Soc. 165 (2018) E872–E878. https://doi.org/10.1149/2.0761816jes.

[174] E.J. Taylor, M. Inman, Electrochemical surface finishing, Electrochem. Soc. Interface. 23 (2014) 57–61. https://doi.org/10.1149/2.F05143if.

[175] V. Finazzi, A.G. Demir, C.A. Biffi, F. Migliavacca, L. Petrini, B. Previtali, Design and functional testing of a novel balloon-expandable cardiovascular stent in CoCr alloy produced by selective laser melting, J. Manuf. Process. 55 (2020) 161–173. https://doi.org/10.1016/j.jmapro.2020.03.060.

[176] L. Denti, A. Sola, On the Effectiveness of Different Surface Finishing Techniques on A357.0 Parts Produced by Laser-Based Powder Bed Fusion: Surface Roughness and Fatigue Strength, Metals (Basel). 9 (2019) 1284. https://doi.org/10.3390/met9121284.

[177] J.R. Davis, ASM Specialty Handbook: Heat-Resistant Materials, ASM International, 1997.

[178] S. Sui, C. Zhong, J. Chen, A. Gasser, W. Huang, J.H. Schleifenbaum, Influence of solution heat treatment on microstructure and tensile properties of Inconel 718 formed by high-deposition-rate laser metal deposition, J. Alloys Compd. 740 (2018) 389–399. https://doi.org/10.1016/j.jallcom.2017.11.004.

[179] J. Vit, Surface metrology open profile Gaussian filter, (2015). https://www.mathworks.com/matlabcentral/fileexchange/52892-surface-metrology-open-profile-gaussian-filter.

[180] A. V. Ribalko, K. Korkmaz, O. Sahin, Intensification of the anodic erosion in electrospark alloying by the employment of pulse group, Surf. Coatings Technol. 202 (2008) 3591–3599. https://doi.org/10.1016/j.surfcoat.2007.12.037.

[181] K.F. Weaver, V.C. Morales, S.L. Dunn, K. Godde, P.F. Weaver, An Introduction to Statistical Analysis in Research: With Applications in the Biological and Life Sciences, 2017. https://doi.org/10.1002/9781119454205.

[182] E. Hosseini, V.A. Popovich, A review of mechanical properties of additively manufactured Inconel 718, Addit. Manuf. 30 (2019) 100877. https://doi.org/10.1016/j.addma.2019.100877.

[183] T.B. Reed, Free Energy of Formation of Binary Compounds: An Atlas of Charts for High-temperature Chemical Calculations, MIT Press, 1971.

[184] A.N.D. Gasper, B. Szost, X. Wang, D. Johns, S. Sharma, A.T. Clare, I.A. Ashcroft, Spatter and oxide formation in laser powder bed fusion of Inconel 718, Addit. Manuf. 24 (2018) 446–456. https://doi.org/10.1016/j.addma.2018.09.032.

[185] Y.N. Zhang, X. Cao, P. Wanjara, M. Medraj, Oxide films in laser additive manufactured Inconel 718, Acta Mater. 61 (2013) 6562–6576. https://doi.org/10.1016/j.actamat.2013.07.039.

[186] L.M. Felix, C.C.F. Kwan, N.Y. Zhou, The Effect of Pulse Energy on the Defects and Microstructure of Electro-Spark-Deposited Inconel 718, Metall. Mater. Trans. A. 50

(2019) 4223–4231. https://doi.org/10.1007/s11661-019-05332-8.

[187] S. Singh, Y. Guo, B. Winiarski, T.L. Burnett, P.J. Withers, M. De Graef, High resolution low kV EBSD of heavily deformed and nanocrystalline Aluminium by dictionary-based indexing, Sci. Rep. 8 (2018) 1–8. https://doi.org/10.1038/s41598-018-29315-8.

[188] S. Kuroda, T.W. Clyne, The quenching stress in thermally sprayed coatings, Thin Solid Films. 200 (1991) 49–66. https://doi.org/10.1016/0040-6090(91)90029-W.

[189] A.J. Wilkinson, D.J. Dingley, Quantitative deformation studies using electron back scatter patterns, Acta Metall. Mater. 39 (1991) 3047–3055. https://doi.org/10.1016/0956-7151(91)90037-2.

[190] A. Oradei-Basile, J.F. Radavich, A Current T-T-T Diagram for Wrought Alloy 718, in: Superalloys 718, 625 Var. Deriv., TMS, 1991: pp. 325–335. https://doi.org/10.7449/1991/Superalloys_1991_325_335.

[191] J.-C. Zhao, M. Larsen, V. Ravikumar, Phase precipitation and time–temperature-transformation diagram of Hastelloy X, Mater. Sci. Eng. A. 293 (2000) 112–119. https://doi.org/10.1016/S0921-5093(00)01049-2.

[192] H.M. Tawancy, Long-term ageing characteristics of Hastelloy alloy X, J. Mater. Sci. 18 (1983) 2976–2986. https://doi.org/10.1007/BF00700780.

[193] Q. Han, R. Mertens, M.L. Montero-Sistiaga, S. Yang, R. Setchi, K. Vanmeensel, B. Van Hooreweder, S.L. Evans, H. Fan, Laser powder bed fusion of Hastelloy X: Effects of hot isostatic pressing and the hot cracking mechanism, Mater. Sci. Eng. A. 732 (2018) 228–239. https://doi.org/10.1016/j.msea.2018.07.008.

[194] M. Suraratchai, J. Limido, C. Mabru, R. Chieragatti, Modelling the influence of machined surface roughness on the fatigue life of aluminium alloy, Int. J. Fatigue. 30 (2008) 2119–2126. https://doi.org/10.1016/j.ijfatigue.2008.06.003.

[195] D. Arola, C.L. Williams, Estimating the fatigue stress concentration factor of machined surfaces, Int. J. Fatigue. 24 (2002) 923–930. https://doi.org/10.1016/S0142-1123(02)00012-9.

[196] J.W. Pegues, N. Shamsaei, M.D. Roach, R.S. Williamson, Fatigue life estimation of additive manufactured parts in the as-built surface condition, Mater. Des. Process. Commun. 1 (2019) e36. https://doi.org/10.1002/mdp2.36.

[197] R. Esmaeilizadeh, A. Keshavarzkermani, U. Ali, B. Behravesh, A. Bonakdar, H. Jahed, E. Toyserkani, On the effect of laser powder-bed fusion process parameters on quasi-static and fatigue behaviour of Hastelloy X : A microstructure / defect interaction study, Addit. Manuf. 38 (2021) 101805. https://doi.org/10.1016/j.addma.2020.101805.

[198] M.A.S. Torres, H.J.C. Voorwald, An evaluation of shot peening, residual stress and stress relaxation on the fatigue life of AISI 4340 steel, Int. J. Fatigue. 24 (2002) 877–886. https://doi.org/10.1016/S0142-1123(01)00205-5.

[199] D. Gopikrishna, S.N. Jha, L.N. Dash, Influence of Microstructure on Fatigue Properties of Alloy 718, in: Superalloys 718, 625, 706 Var. Deriv., TMS, Pittsburgh, Pennsylvania, 1997: pp. 567–573. https://doi.org/10.7449/1997/Superalloys_1997_567_573.

[200] A.D. Boyd-Lee, Fatigue crack growth resistant microstructures in polycrystalline Ni-base superalloys for aeroengines, Int. J. Fatigue. 21 (1999) 393–405. https://doi.org/10.1016/S0142-1123(98)00087-5.